QUANTIFYING COMPOSITIONAL IMPACTS OF AMBIENT AEROSOL ON CLOUD DROPLET FORMATION

A Dissertation
Presented to
The Academic Faculty

by

Sara Lance

In Partial Fulfillment
of the Requirements for the Degree
Doctor of Philosophy in the
School of Earth and Atmospheric Sciences

Georgia Institute of Technology
December, 2007

QUANTIFYING COMPOSITIONAL IMPACTS OF AMBIENT AEROSOL ON CLOUD DROPLET FORMATION

Approved by:

Dr. Athanasios Nenes, Advisor
School of Earth and Atmospheric Sciences
Georgia Institute of Technology

Dr. James N. Smith
Atmospheric Chemistry Division
National Center for Atmospheric Research

Dr. Rodney Weber
School of Earth and Atmospheric Sciences
Georgia Institute of Technology

Dr. Michael Bergin
School of Earth and Atmospheric Sciences
Georgia Institute of Technology

Dr. Armistead Russell
School of Civil and Environmental Engineering
Georgia Institute of Technology

Date Approved: November 2, 2007

ACKNOWLEDGEMENTS

Thanks to Jeessy for teaching me that life is more than grad school, Akua for teaching me how to get pumped up for a talk, Christos for teaching me to "be myself," Nicholas for teaching me to be skeptical of measurements, Luz for teaching me to have a sense of humor, Donifan for teaching me to defend my work, Rich for teaching me to question everything, Rafaella and Thimios for teaching me how to balance work and family life, Wei-Chun for teaching me to listen and Thanos for teaching me that hard work and dedication pays off! Deep thanks to Matt for being my best friend, Tim for looking out for me, Jeff for keeping it real, Kelley for teaching me what a strong woman scientist is, Andy for teaching me how to carefully state a case, and of course Jim for teaching me about the wonderful chaotic life of an experimentalist. Each of you has helped me more than you know. I am extremely grateful to all of you. Good luck to everyone, and I look forward to seeing you again!

Special thanks to ASP for the wonderful program that allowed me to be at NCAR for two and a half years.

TABLE OF CONTENTS

	Page
ACKNOWLEDGEMENTS	iii
LIST OF TABLES	vii
LIST OF FIGURES	viii
SUMMARY	xi
CHAPTER	
1 CHEMICAL AND DYNAMICAL EFFECTS ON CLOUD DROPLET NUMBER: IMPLICATIONS FOR ESTIMATES OF THE AEROSOL INDIRECT EFFECT	1
Introduction	1
Methods	8
The Aerosol	11
Aerosol used in this study	13
Aerosol-Drop Number Correlations	14
The Cloud Parcel Model	16
Empirical Correlations and Model Setup	17
Results	21
Base-case Updraft Velocity	21
Sensitivity of Droplet Number to Updraft Velocity	25
Sensitivity of Droplet Number to Chemical Effects	28
Chemical and Dynamical Effects for Variable Aerosol Number	31
Implications for the Aerosol Indirect Effect	32
Conclusions	34

2 MAPPING THE OPOERATION OF THE DMT CONTINUOUS FLOW CCN COUNTER 37

Introduction 38

Instrument Description 39

Instrument and Droplet Growth Models 42

Characterization of Wall Thermal Resistance 43

Definition of Thermal Efficiency 43

Experimental Determination of Thermal Efficiency 45

Theoretical Determination of Thermal Efficiency 48

Mapping Thermal Efficiency 53

Mapping Supersaturation 58

Recommended Procedure for Calibrating Thermal Resistance 59

Particle Growth and CCN Counting 60

The Optimal OPC Detection Threshold 60

Resolution Ratio 67

CCN with Slow Growth Kinetics 69

Distinguishing Slow Growing and Low S_c particles from Droplets 71

Summary 72

3 INFERRING THE AEROSOL MIXING-STATE FROM MEASURED AMBIENT CLOUD ACTIVATION SPECTRA DURING THE MIRAGE CAMPAIGN 75

Introduction 75

Experimental Method 76

Analysis Method 81

Sigmoidal Fit of CCN Activation Spectra 82

Comprehensive Analysis 89

Particle Size Distribution Approximation 101

Results 105

Comparing the Inferred and Direct Chemical Measurements 107

Diurnal Behavior of CCN Activation 113

Potential Mechanisms for Chemical Broadening 115

Quantifying Uncertainties 120

Size-Resolved Droplet Growth Kinetics 122

Conclusions 128

4 CCN CLOSURE IN THE POLLUTED BOUNDARY LAYER OVER HOUSTON, TX DURING THE GULF OF MEXICO ATMOSPHERIC COMPOSITION AND CLIMATE STUDY (GOMACCS) 130

Introduction 130

Measurements 131

CCN Closure 133

Conclusions 143

REFERENCES 144

VITA 153

LIST OF TABLES

	Page
Table 1.1: Average Modal Size Distribution Parameters	10
Table 1.2: Modal Base Case Chemical Compositions	10
Table 1.3: Base Case Modal Aerosol Number Concentrations	14
Table 1.4: Base Case, Lower and Upper Limits for Sensitivity Parameters	29
Table 2.1: Input Variables to the Instrument Model	54
Table 2.2: Regression Coefficients for Thermal Efficiency Parameterization	56

LIST OF FIGURES

Page

Figure 1.1: "Inverse Modeling" Sensitivity Analysis Method 11

Figure 1.2: Marine Cloud Droplet Number Sensitivity to Dynamics and Chemistry 26

Figure 1.3: Continental Droplet Number Sensitivity to Dynamics and Chemistry 27

Figure 1.4: Polluted Cloud Droplet Number Sensitivity to Dynamics and Chemistry 28

Figure 1.5: Percent Change in Cloud Reflectivity 33

Figure 2.1: Schematic of the CFSTGC calibration setup 40

Figure 2.2: Cross-sectional representation of the CCN column turned on its side 44

Figure 2.3: Activation Curve for $(NH_4)_2SO_4$ and NaCl 46

Figure 2.4: Thermal Efficiency 55

Figure 2.5: Overestimate of Supersaturation when Neglecting Thermal Resistance 57

Figure 2.6: Example Simulated Droplet Growth Curve and Fit 61

Figure 2.7: Instrument Supersaturation and Optimal OPC Detection Threshold 62

Figure 2.8: Minimum Time Available for Droplet Growth 66

Figure 2.9: Resolution Ratio vs. ΔT_{inner} 69

Figure 2.10: Optimal OPC Detection Threshold for Slow Growing Droplets 70

Figure 2.11: Modeled Droplet Curves at Two Residence Times 72

Figure 3.1: Schematic of the Hygroscopicity Tandem Differential Mobility Analyzer 79

Figure 3.2: Schematic of HTDMA and CCNc Parallel Sampling 80

Figure 3.3: HTDMA and CCNc Operation Schedule 81

Figure 3.4: Example Activation Spectrum with Explanation of Fit Parameters 83

Figure 3.5: Probability Distributions of Scaled Volume Fraction 87

Figure 3.6: Chemical Dispersion versus Sigmoidal Fit Parameters 88

Figure 3.7: Uncertainty in Inferred Chemistry 89

Figure 3.8: Comparing Calibration and Ambient Activation Spectra 92

Figure 3.9: Sigmoidal Fits for Size-Resolved Ambient Activation Spectra 95

Figure 3.10: Comprehensive Analysis of Size-Resolved Activation Spectra 97

Figure 3.11: Inferred “Chemical Distributions” from Two Analytical Methods 98

Figure 3.12: Activation Spectra Showing Affect of Size-Resolved Chemistry 100

Figure 3.13: Effect of the Sheath to Aerosol Ratio on Typical Activation Spectra 102

Figure 3.14: Maximum Effect of the Sheath to Aerosol Ratio on Activation Spectra 103

Figure 3.15: Inferred “Chemical Distributions” from Three Analytical Methods 105

Figure 3.16: Timeseries of Inferred Chemistry and other Ambient Observations 106

Figure 3.17: Comparison of SVF from Two Direct Chemical Measurements 112

Figure 3.18: Diurnal CCN Behavior 114

Figure 3.19: Illustration of Condensational Affect on the Chemical Distribution 115

Figure 3.20: Illustration of Two Chemical Distributions after Coagulation 117

Figure 3.21: Comparison of Nonactivated Fraction with Single Particle Chemistry 119

Figure 3.22: Diurnal CCN Behavior with Pollution Outflow Days Highlighted 120

Figure 3.23: Chemical Variability versus Chemical Uncertainty 122

Figure 3.24: Timeseries of Average Droplet Diameter for 100 nm dry particles 124

Figure 3.25: Average Droplet Diameter vs. Characteristic Critical Supersaturation 125

Figure 3.26: Average Droplet Diameter versus Instrument Supersaturation 127

Figure 4.1: Regional Map of the Research Flight Tracks during GoMACCS 131

Figure 4.2: CCN Closure for the Entire Dataset Assuming Ammonium Sulfate 134

Figure 4.3: Flight Track for RF22 colored by Total Particle Concentration 135

Figure 4.4: Flight Track for RF22 colored by Organic Fraction 136

Figure 4.5: Timeseries of Predicted and Measured CCN, Droplet Size Distribution 137

Figure 4.6: CCN Closure for RF22 with Three Assumptions of Particle Chemistry 138

Figure 4.7: Average Droplet Diameter versus Instrument Supersaturation 142

SUMMARY

The largest uncertainty in prediction of anthropogenic influences on climate change involves the details of the hydrological cycle [Intergovernmental Panel on Climate Change (IPCC), 2007]. Water in the atmosphere has three major, competing effects on climate. Water vapor is the primary greenhouse gas in the Earth's atmosphere. Conversely, liquid water in the form of suspended cloud droplets accounts for about 30% of the Earth's albedo [Charlson et al., 1987]. Water ice in the upper troposphere absorbs infrared radiation emitted by the Earth. The mechanisms for distribution of each phase are therefore important for determining the overall effect of atmospheric water on climate. Aerosols affect the formation, radiative properties and lifetime of clouds, collectively known as the aerosol "indirect effect" on climate. The focus of this thesis is the formation of liquid water clouds.

It has been historically assumed that most of the uncertainty associated with the indirect effect can be attributed to the unpredictability of updrafts. In Chapter 1, we analyze the sensitivity of cloud droplet number density, N_D, to realistic variations in aerosol chemical properties and to variable updraft velocities using a 1-dimensional cloud parcel model in three important environmental cases (continental, polluted and remote marine). The modeled aerosol size distribution, aerosol chemical composition, cloud updraft velocity, water vapor supersaturation and N_D for all cases were consistent with published measurements. The results suggest that aerosol chemical variability may be as important to the aerosol indirect effect as the effect of unresolved cloud dynamics, especially in polluted environments.

Our next task was to see if chemical variability of ambient particles in polluted environments can account for the uncertainty in our predictions of cloud formation. Cloud Condensation Nuclei (CCN) concentrations, which are fundamentally important for studies of aerosol-cloud-climate interactions, provide the direct quantitative link between aerosol and clouds. We used a continuous flow streamwise thermal gradient CCN counter (CCNc) to study the water-uptake properties of the ambient aerosol, by exposing an aerosol sample to a controlled water vapor supersaturation and counting the resulting number of droplets. In Chapter 2, we modeled and experimentally characterized the heat transfer properties and droplet growth within the CCNc.

Chapter 3 describes results from the MIRAGE field campaign, in which the CCNc and a Hygroscopicity Tandem Differential Mobility Analyzer (HTDMA) were deployed at a ground-based site during March, 2006. Size-resolved CCN activation spectra and growth factor distributions of the ambient aerosol in Mexico City were obtained, and an analytical technique was developed to quantify a probability distribution of solute volume fractions for the CCN in addition to the aerosol mixing-state. The CCN were shown to be much less CCN active than ammonium sulfate, with water uptake properties more consistent with low molecular weight organic compounds. The pollution outflow from Mexico City was shown to have CCN with an even lower fraction of soluble material. "Chemical Closure" was attained for the CCN, by comparing the inferred solute volume fraction with that from direct chemical measurements. A clear diurnal pattern was observed for the CCN solute volume fraction, showing that measurable aging of the aerosol population occurs during the day, on the timescale of a

few hours. The mixing state of the aerosol, also showing a consistent diurnal pattern, clearly correlates with a chemical tracer for local combustion sources.

Chapter 4 describes results from the GoMACCS field study, in which the CCNc was subsequently deployed on an airborne field campaign in Houston, Texas during August-September, 2006. GoMACCS tested our ability to predict CCN for highly polluted conditions with limited chemical information. Assuming the particles were composed purely of ammonium sulfate, CCN closure was obtained with a 10% overprediction bias on average for CCN concentrations ranging from less than 100 cm^{-3} to over 10,000 cm^{-3}, but with on average 50% variability. Assuming measured concentrations of organics to be internally mixed and insoluble tended to reduce the overprediction bias for less polluted conditions, but led to underprediction bias in the most polluted conditions. A likely explanation is that the high organic concentrations in the polluted environments depress the surface tension of the droplets, thereby enabling activation at lower soluble fractions.

Comparing the two campaigns, it is clear that the chemistry of the particles plays an important role in our ability to predict CCN concentrations. However, our observations of droplet growth kinetics for both the MIRAGE and GoMACCS field campaign suggest that the organic constituents in the ambient aerosol do not often delay droplet growth substantially.

CHAPTER 1

CHEMICAL AND DYNAMICAL EFFECTS ON CLOUD DROPLET NUMBER: IMPLICATIONS FOR ESTIMATES OF THE AEROSOL INDIRECT EFFECT

Introduction

Cloud droplets in the atmosphere are formed from condensation of water vapor upon cloud condensation nuclei (CCN). Both the physical and chemical characteristics of a CCN population influence the number and size of cloud droplets that form. However, the physical and chemical properties of CCN vary significantly with space and time, since the sources and sinks of CCN are localized and since CCN have short atmospheric lifetimes (as compared to the mixing timescale of the atmosphere). In addition, the cloud updraft velocity, which is highly variable within a cloud and difficult to measure [*Mason*, 1971], has a strong influence on the number and size of cloud droplets formed; a higher updraft provides a higher water-vapor supersaturation, which is the driving force for condensational growth. The strong variability in these parameters, to which cloud droplet formation is highly sensitive, causes much of the uncertainty in cloud modeling.

Most of the radiative properties of liquid water clouds can be inferred from knowledge of the cloud liquid water content and cloud droplet number concentration. *Twomey* [1974] suggested that increasing the number of aerosol particles increases the number of CCN, which increases the number of cloud droplets and leads to a higher

Lance S., A. Nenes, T.A. Rissman, Chemical and dynamical effects on cloud droplet number, *J. Geophys. Res.*, 109 (D22), 2004. Published American Geophysical Union.

cloud albedo. The increased cloud reflectivity, and the associated radiative cooling, is referred to as the "first indirect climate effect" of aerosols. Global Climate Models (GCMs) are currently incapable of providing the resolution necessary for explicitly addressing the scales involved in aerosol-cloud interactions; instead, empirical correlations between cloud droplet number and one aerosol characteristic (e.g. number concentration [*Gultepe and Isaac*, 1999] or sulfate mass [*Boucher and Lohmann*, 1995]) are often used to quantify aerosol-cloud interactions. The variability inherent in such relationships translates to a large predictive uncertainty of the indirect effect, potentially as large as the greenhouse gas radiative forcing [*IPCC,* 2001]. For example, in the *Boucher and Lohmann* [1995] observations, the cloud droplet number concentration ranges from 60 to 600 cm^{-3} for an aerosol non-sea-salt (nss) sulfate mass of 1 $\mu g\ m^{-3}$. For the same liquid water path, this variability in cloud droplet concentration could lead to a change in cloud reflectivity of up to ~60% [*Seinfeld and Pandis*, 1998]. This large variability shows that cloud droplet number is strongly influenced by factors other than sulfate mass, but does not indicate what the variability can be attributed to.

The variability in the *Boucher and Lohmann* [1995] and *Gultepe and Isaac* [1999] observations is historically attributed to variations in cloud updraft velocity [*IPCC*, 2001]. Although updraft variations may produce an order-of-magnitude range in droplet number, recent work has suggested that a variety of organic chemical effects, including reduction in surface tension and modified growth kinetics, can potentially contribute as much to the variability in cloud droplet number as updraft velocity.

Facchini et al. [2000] observed a significant decrease in the surface tension of polluted fog water samples, by as much as 25%, compared to the surface tension of pure

water. The normalized surface tension depression was related to the bulk concentration of water-soluble organic compounds (WSOC), fit to the Szyszkowski-Langmuir equation [*Facchini et al*, 1999]. The WSOC were separated into three main classes, and it was determined that polyacidic compounds in the ambient aerosol were mainly responsible for the observed surface tension depression [*Facchini et al*, 2000]. *Facchini et al* [1999] estimated, using Köhler theory and assuming a power-law relationship between droplet number and supersaturation, that the maximum decrease in surface tension could lead to an ~20% increase in the number of cloud droplets.

Li et al [1998] found that laboratory-generated aerosol consisting of mixtures of sodium dodecyl sulfate (SDS) and NaCl can lower the surface tension by up to 20% compared to the same size dry particle composed of pure NaCl. The surface tension was related to the bulk surfactant (SDS) concentration, using the Szyskowski equation of state. In addition, surfactant partitioning between the bulk and surface of the droplet was considered and the Critical Micelle Concentration (CMC) was calculated, at which point the surface tension becomes nearly constant with additional solute. SDS was used because its properties are well defined and it has a similar effect on surface tension as surfactants found in ambient aerosol. However, SDS is not likely found in significant quantities in the atmosphere [*Li et al*, 1998], and the solubility of SDS has not been shown to be representative of organic surfactants in atmospheric aerosol. Furthermore, it is rare for submicron atmospheric aerosol to be composed purely of NaCl; ammonium sulfate/nitrate aerosol mixed with partially soluble and insoluble compounds (as used in the *Facchini et al* [1999] study) is far more common for CCN [*Heintzenberg*, 1989], and may thus be a better basis for comparison.

Interestingly, *Li et al* [1998] found that the solubility of SDS is low enough to counteract the effect of surface tension depression, and leads to a higher critical supersaturation than for a pure NaCl aerosol particle of the same dry size. This might at first appear to contradict the conclusions of *Facchini et al* [1999]. However, the basis for comparison between the two studies is not the same; *Facchini et al* [1999] compared aerosol of the same composition with and without surface tension depression, whereas *Li et al* [1998] compared the SDS/NaCl mixture to a pure NaCl aerosol. Thus, the main difference is that for the *Facchini et al* [1999] study there was no change in the Raoult term of the Köhler equation, whereas the *Li et al* [1998] study covaried droplet surface tension and number of dissolved moles by replacing SDS with NaCl. It was found by *Facchini et al* [2001] that including the surfactant partitioning from *Li et al* [1998] to characterize the surfactant properties of their sampled fog droplets yields a slight increase in critical supersaturation as compared to using a single-phase bulk surfactant concentration. However, this increase is minor compared to the large increase in supersaturation that results from assuming a constant surface tension. In other words, however surface tension is characterized, surface tension depression resulting from organic surfactants has been shown to be important, and must be included in cloud models.

Shulman et al [1996] measured the solubility and surface tension of laboratory generated aerosols, which consisted of two-component mixtures of ammonium sulfate and various difunctional organic oxygenates that have significant concentrations in the atmosphere (e.g. cis-pinonic acid and glutaric acid). The observed surface tension decreased by as much as 20% compared to pure water. It was also found that higher

concentrations of ammonium sulfate actually enhanced the surface tension depression for cis-pinonic acid. This relatively high molecular weight organic compound is the least soluble of the model compounds studied; however, the addition of 0.5 M ammonium sulfate (which is ubiquitous in the atmosphere) allowed for the same ~20% reduction in surface tension depression at half the cis-pinonic acid concentration (0.02 M rather than 0.04 M).

Numerous modeling studies have been performed to estimate the effect of the observed surface tension depression and gradual dissolution of organic compounds. *Nenes et al*. [2002] used a numerical cloud parcel model to show that the reduction in surface tension due to organic surfactants can have a greater effect on droplet number than doubling aerosol number, for polluted aerosol at low updraft. For marine aerosol at high updraft, the enhancement in droplet number from surfactants can be about half of that seen by doubling the aerosol number concentration. *Rissman et al*. [2004] modified an existing parameterization by *Abdul-Razzak et al.* [1998, 2000] to explicitly account for the effect of surface active organics on droplet number. The modified parameterization was used to identify regimes for which varying aerosol mass fraction of surface active organic species can have as large an effect on the number of cloud droplets as varying updraft velocity. *Rissman et al*. [2004] conclude that the normalized cloud droplet number sensitivity to aerosol organic mass fraction (relative to updraft velocity) is usually positive, between 10 and 50%, with the strongest relative chemical effect at higher updraft velocity. For the marine aerosol, as updraft velocity increases above ~0.4 m s^{-1}, the relative sensitivity becomes nearly constant. For continental aerosol, the relative sensitivity can be negative at low updraft velocities, implying that an increase in

aerosol organic mass fraction increases CCN concentration, but decreases the number of cloud droplets (by decreasing the maximum supersaturation). *Mircea et al* [2002] estimated that water soluble organic compounds, modeled after the *Facchini et al* [1999] observations, may increase the CCN number concentration by up to 13% for a marine aerosol, by up to 97% for a rural aerosol and by up to 110% for an urban aerosol, under typical atmospheric supersaturations. These studies illustrate that the response in CCN concentrations from the presence of organic surfactants is often important, and strongly depends on the size distribution of chemical composition and aerosol number, and the local dynamical conditions of cloud formation.

The presence of organic film-forming compounds (FFCs), which form a thin film over a partially deliquesced aerosol particle (with the hydrophobic side of the molecules facing outward and the hydrophilic side facing inward), have the potential to inhibit the rate of droplet growth. The condensation coefficient, which is the probability of a water vapor molecule "sticking" upon collision with an aerosol particle, may be considerably reduced when FFCs are present on the particle surface. A condensation coefficient of 0.045 is widely recognized by the cloud physics community as the typical value for atmospheric droplets (e.g. *Feingold and Chuang* [2002] used a value of 0.042 to represent typical FFC-free cloud droplets), although the value varies significantly between studies [*Mozurkewich*, 1986; *Pruppacher and Klett*, 2000]. *Pruppacher and Klett* [2000] summarize that an aged atmospheric drop will have a condensation coefficient of ~0.01 while a clean drop will have a value closer to unity. Two recent studies indicate that the condensation coefficient of pure water is even smaller than

previously estimated; *Shaw and Lamb* [1999] estimate a value of 0.04-0.1 and *Li et al* [2001] estimate a value of 0.17 ± 0.03 at 280K and 0.32 ± 0.04 at 258K.

There is evidence for the existence of FFC compounds in ambient aerosol that lower the condensation coefficient to as low as 10^{-5} [*Chuang*, 2003]. This lower condensation coefficient indicates that at least 99.98% fewer collisions result in "capture" of a water molecule from the gas as compared to an uncoated cloud drop. However, the chemical composition of FFC-coated particles and the corresponding condensation coefficients are issues that need to be addressed in future studies. In addition, the distribution of FFCs within the aerosol population must be looked at carefully. The modeling study of *Feingold and Chuang* [2002] shows that when a minor fraction (5-10% mass) of polluted aerosol is composed of FFCs, and the FFC is distributed according to surface area, modified growth kinetics can suppress the number of cloud droplets by as much as 90%. When *Nenes et al*. [2002] distributed the same organic FFC by aerosol mass, a decrease in the initial rate of condensation led to a large enough increase in cloud parcel supersaturation that the end result was an increase (by 50-100%) in cloud droplet number. For marine aerosols, both studies found that cloud droplet number was modestly affected by the presence of FFCs. *Feingold and Chuang* [2002] also did simulations in which the FFC was distributed by mass, which resulted in nearly the same droplet number as when FFCs were not present. However, *Feingold and Chuang* [2002] used a unimodal lognormal size distribution whereas *Nenes et al* [2002] used a trimodal lognormal distribution. Distributing the FFC by mass reduces the growth of larger aerosol particles, which can increase the cloud supersaturation and allow more of the smaller particles to activate. The greater number of larger aerosol in the *Nenes et al*

[2002] study was a significant factor enabling greater droplet activation when the condensation coefficient was decreased to 10^{-5}.

These and many other studies have shown that considerable variability in cloud droplet number may be induced by different chemical effects, but they do not assess the potential significance of the chemical effects on scales larger than individual updrafts. The current study attempts to address the cloud-system scale by using an inverse modeling approach. This unique approach uses empirical correlations of aerosol number and sulfate mass versus droplet number, observed ranges of chemical composition, cloud dynamics and aerosol size distribution to constrain the chemical effects on cloud droplet number for cloud-system scales. The observational dataset includes cumuliform and stratiform clouds and CCN originating from both clean and polluted conditions. We use a numerical adiabatic cloud parcel model with explicit microphysics [*Nenes et al*., 2001] to determine the minimum updraft velocity required to produce the number of droplets described by the *Boucher and Lohmann* [1995] and *Gultepe and Isaac* [1999] correlations. This base-case updraft velocity is then used with the parcel model to estimate the sensitivity of cloud droplet number to organic chemical effects. For comparison, cloud droplet number sensitivity to updraft velocity is also estimated.

Methods

Not all the factors affecting the number of cloud droplets are available from the published data. To overcome this lack of information, we adopt an inverse modeling analysis to constrain key unresolved parameters. The procedure is illustrated in Figure

1.1. For a given aerosol number, the *Gultepe and Isaac* [1999] correlations provide the cloud droplet number, and the *Boucher and Lohmann* [1995] correlations provide the aerosol sulfate mass. With information about the aerosol size distribution, an updraft velocity can be determined that is consistent with the observations; these conditions are used as a "base-case". Organic mass fraction, condensation coefficient, updraft velocity, and aerosol number concentration are then varied to assess their effects on cloud droplet number. The aerosol physical characteristics (Table 1.1) and chemical composition (Table 1.2) used in the analysis are obtained from published literature.

The exact procedure (Figure 1.1) is as follows: 1) specify the average aerosol physical and chemical characteristic for three "base-case" environments (polluted, continental and marine) based on published observations, 2) determine a droplet number concentration that may result for these situations based on the average empirical relations of *Gultepe and Isaac* [1999], 3) using the *Boucher and Lohmann* [1995] correlation, determine a representative sulfate mass concentration that corresponds to the cloud droplet concentration determined from the *Gultepe and Isaac* [1999] correlations, 4) determine the coarse mode sulfate mass fraction and/or coarse mode number concentration needed to provide this total sulfate mass, and 5) determine an updraft velocity that can produce the droplet concentration from step 2 using the numerical cloud parcel model of *Nenes et al*., [2001]. These updraft velocities and aerosol characteristics are referred to as the "base-case" values. The sensitivity of cloud droplet number to chemical effects is assessed by introducing a reasonable variability in organic mass fraction and condensation coefficient. The sensitivity of cloud droplet number to updraft velocity is also computed for comparison. When varying the cloud updraft velocity, the

organic mass fraction is maintained at the base-case value, with a condensation coefficient of 0.045. When varying the organic mass fraction, the base-case updraft velocity is maintained, with a condensation coefficient of 0.045. While varying the condensation coefficient, the base-case updraft velocity and organic mass fraction are assumed.

Table 1.1. Average modal size distribution parameters ($\overline{D}_{gi}$ in μm, N_i in cm^{-3}) from *Whitby* [1978]. *Average fine marine parameters over the latitude range from *Heintzenberg* [2000] and coarse mode parameters from *Jaenicke* [1993].

Aerosol Type	**Nuclei Mode**			**Accumulation Mode**			**Coarse Mode**		
	$\overline{D}_{g1}$	σ_{g1}	N_1	$\overline{D}_{g2}$	σ_{g2}	N_2	$\overline{D}_{g3}$	σ_{g3}	N_3
Remote Marine	0.01	1.6	340	0.071	2.0	60	0.62	2.7	3.1
*Latitudes 60 – 75°S	0.018	1.4	310	0.075	1.6	70	0.58	2.49	3.1
*Latitudes 15– 60°N	0.020	1.47	230	0.092	1.47	176.7	0.58	2.49	3.1
Clean Continental	0.016	1.6	1000	0.067	2.1	800	0.93	2.2	0.72
Polluted	0.014	1.8	106000	0.054	2.16	32000	0.86	2.21	5.4

Table 1.2. Modal base-case chemical composition for each aerosol type used in this study. The fine particle ($\overline{D}_{gi}$ < 0.1 μm) mass fractions are obtained from *Heintzenberg* [1989]. Coarse mode sulfate mass fractions are calculated using the procedure outlined in the text. The other coarse mode mass fractions are estimated from [*Fitzgerald*, 1991; *Ramanathan et al*., 2001; *Neusüβ et al.*, 2002; *Finlayson-Pitts and Pitts*, 1986].

	Fine			**Coarse**			
Aerosol type	ε_{SO4}	ε_o	ε_{ins}	ε_{SO4}	ε_{NaCl}	ε_o	ε_{ins}
Marine	0.22	0.11	0.67	0.05	0.93	-	0.05
Clean Continental	0.37	0.24	0.39	0.07	-	-	0.9
Diluted Polluted	0.28	0.31	0.41	0.11	-	0.2	0.644

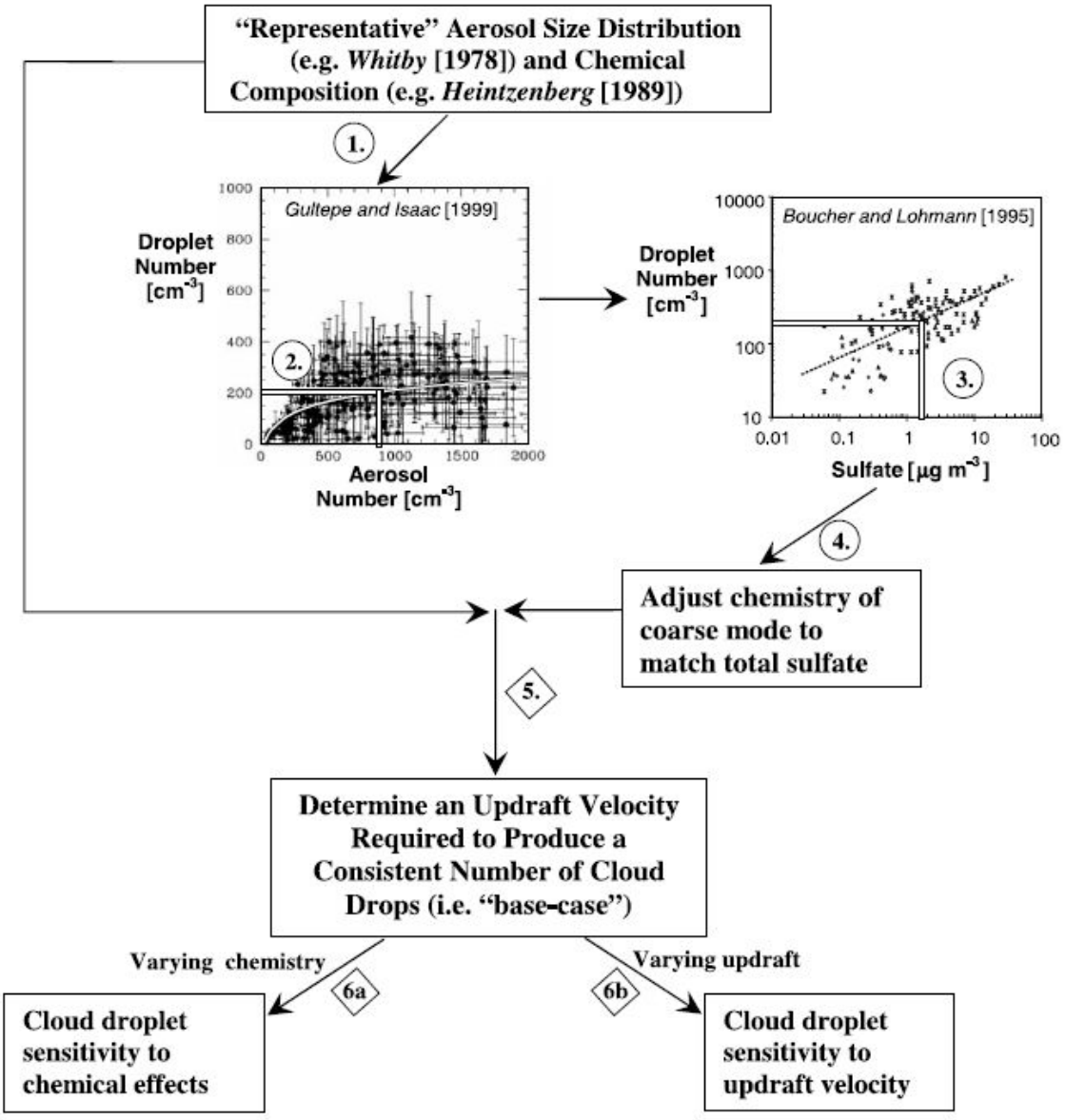


Figure 1.1 Flow diagram illustrating the ''inverse modeling'' analysis methodology used for determining cloud droplet number concentration sensitivities. Steps 1–4 (numbers in circles) involve manipulation of observational data, while the remaining steps (numbers in diamonds) employ the cloud parcel model.

The Aerosol

Aerosol around the globe are diverse in their size distribution, number concentration and chemical composition, and exhibit significant spatiotemporal variability. As changes in aerosol physical characteristics are known to have a significant

effect on the resulting cloud droplet number, the aerosol characteristics used in this analysis must encompass this diversity.

Regardless of the origin of the air mass, often three distinct modes are observed in the aerosol size distribution (nuclei, accumulation and coarse modes). The nuclei and accumulation modes together represent what are often referred to as "fine particles" (with geometric mean diameters less than 0.1 μm). *Whitby* [1978] characterized sulfur-containing aerosols by averaging multiple size distribution measurements made at several sites over a decade. The following classes were defined: 1) marine surface background, 2) continental background, 3) average continental background, 4) background plus aged urban plume, 5) background plus local sources, 6) urban average, 7) urban plus freeway [*Whitby and Sverdrup,* 1978]. These measurements were fit to trimodal lognormal distributions, as shown for marine, continental, and polluted aerosol in Table 1.1.

Fine particle chemical compositions have been analyzed by *Heintzenberg* [1989], using data from 21 cities in the United States, China, Europe and Japan; 15 non-urban continental sites in Sweden, Brazil, the United States and United Kingdom; and 13 locations in remote marine regions (Table 1.2). The fine particles mainly consist of sulfate, carbonaceous material (including elemental and organic carbon), ammonia and nitrate. While inorganic compounds are relatively easy to resolve by online chemical analysis, a substantial portion of organic matter in atmospheric aerosols has remained uncharacterized due to the wide range of carbon numbers, functional groups and solubilities in extraction media [*Saxena and Hildemann*, 1996]. The organic mass fraction in polluted and continental aerosol often comprises an estimated 20% of fine particle mass [*Heintzenberg*, 1989; *Ramanathan et al*., 2001; *Neusüß et al.*, 2002].

However, the organic mass fraction may potentially be as high as 70% for a highly polluted aerosol [*Saxena and Hildemann*, 1996]. It is estimated that organic carbon (OC) can represent up to 50% of the PM_{10} mass over the continental U.S. [*Saxena and Hildemann*, 1996; *Seinfeld and Pandis*, 1998]. Given that the total organic mass can represent up to 1.1 times the OC mass for non-urban aerosol [*Turpin and Lim*, 2001], organic compounds may represent up to 100% of the aerosol mass in continental aerosol. For marine aerosol, the organic mass fraction may be as high as 41-67% [*Heintzenberg*, 1989].

Aerosol used in this study

Three different aerosol (marine, continental and polluted) are represented in this study. The trimodal lognormal size distributions used in this analysis are based on the distributions of *Whitby* [1978], scaling the modal aerosol number concentrations to be within the range of the *Gultepe and Isaac* [1999] observations (Table 1.3). *Heintzenberg's* [1989] observed sulfate and organic mass fractions represent the fine particle composition for these cases (Table 1.2). The polluted coarse mode aerosol composition is estimated by averaging mass fraction observations reported by *Ramanathan et al*. [2001], *Neusüβ et al.* [2002] and *Finlayson-Pitts and Pitts* [1986]. The marine coarse mode aerosol composition estimated by *Fitzgerald* [1991] is used, and the continental coarse mode composition is assumed to be 90% insoluble and 10% ammonium sulfate. We vary the fine particle organic mass fractions from 0 to 0.41 (marine), from 0 to 0.45 (continental) and 0 to 0.61 (polluted), which are below the ranges previously noted. When the organic mass fraction is increased, the sulfate mass

fraction remains as specified by *Heintzenberg* [1989], and the insoluble mass fraction is adjusted. This is an important difference from many studies (e.g. *Li et al* [1998]), in which highly hygroscopic inorganic salts are replaced with partially soluble organic compounds.

Table 1.3. Base-case modal aerosol number concentrations (N_i [cm^{-3}]) as obtained from the procedure outlined in the text. The other modal size distribution parameters are given in Table 1. Base-case droplet number (N_d [cm^{-3}]) and total aerosol sulfate mass (m_{SO4}, $\mu g\ m^{-3}$) as constrained by the *Gultepe and Isaac* [1999]* and *Boucher and Lohmann* [1995]** correlations.

	Modal Number Concentration (cm^{-3})				**Parameters Constrained by Droplet Correlations**	
Aerosol Type	Nuclei	Accumulation	Coarse	Total (N_{ap})	N_d *	m_{SO4} **
Marine	230	177	3.1	410	150	1.75
Clean Continental	555	444	4.1	1003	299	4.46
Diluted Polluted	1152	348	5.4	1505	352	6.62

The water-soluble organic component (by a simplification of chemical composition observed in Po Valley, Italy) is assumed to be composed of (by mass) 18% levoglucosan ($C_6H_{10}O_5$, density = 1600 kg m^{-3}, van't Hoff factor = 1), 41% succinic acid ($C_6O_4H_6$, density = 1572 kg m^{-3}, van't Hoff factor = 3), and 41% fulvic acid ($C_{33}H_{32}O_{19}$, density = 1500 kg m^{-3}, van't Hoff factor = 5) [*Nenes et al*., 2002]. The average solubility is assumed to be 0.02 kg/kg H_2O (or, 0.1 moles C L^{-1}).

Aerosol - Droplet Number Correlations

The data represented by the *Boucher and Lohmann* [1995] and *Gultepe and Isaac* [1999] correlations cover a wide range of conditions of cloud formation. The *Boucher*

and Lohmann [1995] correlations are based on four datasets, which include 85 observations of cloud droplet number and cloud water sulfate within stratiform and cumuliform clouds over North America [*Leaitch et al*., 1992]; 15 observations of nss sulfate and CCN active at 0.3% supersaturation at Cheeka Peak, Washington [*Berresheim et al*., 1993; *Quinn et al*., 1993]; 12 observations of dimethylsulfide (DMS), nss sulfate mass, and CCN active over the Northeast Atlantic [*Hegg et al*., 1993]; and 14 observations of accumulation mode particle concentrations and sulfate mass concentrations over the North Atlantic [*Van Dingenen et al*., unpublished data].

The *Gultepe and Isaac* [1999] plots of cloud droplet number concentration versus aerosol number concentration is based on five datasets, which include observations in Syracuse, New York; Ontario (EMEFS I and EMEFS II); Nova Scotia (NARE); Bay of Fundy and central Ontario (RACE). There were more than 10,000 observations collected over a period of eleven years. The cloud types observed were primarily stratus and stratocumulus.

These observations exhibit a high degree of variability. Thus, we do not use the correlations to predict the number of droplets for individual updrafts. Rather, the correlations are used to estimate a representative updraft velocity that is required to produce the typical observed droplet concentration for cloud-systems in different environments (represented by average aerosol chemical and physical characteristics, and by the representative "base-case" updraft velocity). The *Gultepe and Isaac* [1999] and *Boucher and Lohmann* [1995] correlations are currently being used in GCMs, and the inherent variability they are subject to contributes to the large predictive uncertainty in

the models. By evaluating the sensitivities within the context of these correlations, we are providing an assessment within the framework of the current methodology.

The Cloud Parcel Model

The cloud parcel model [*Nenes et al*., 2001] captures the explicit aerosol microphysics of cloud droplet formation by diffusional growth. The model simulates the evolution of liquid water cloud droplet distributions in a non-precipitating, adiabatic updraft and has been used in numerous studies, including a successful CCN/Cloud droplet number closure study using *in-situ* observations from the NASA Crystal-FACE mission [*Conant et al*, in press]. The presence of slightly soluble and surfactant substances in CCN is treated explicitly, using the *Facchini et al*. [1999] correlation to characterize the surface tension of the growing droplets. The model computes the time-dependent particle sizes, water vapor supersaturation, pressure and temperature. The initial parcel conditions assumed are a relative humidity of 98%, temperature of 284.2 K, and pressure of 939 mb. The aerosol is not initially in equilibrium with the environment. The updraft is assumed constant, since we are only interested in the cloud drop activation process, which generally occurs on the order of seconds; the buoyancy of the cloud parcel does not change significantly within this time. The number of droplets is computed by finding the CCN of highest critical supersaturation that activates (i.e. with a diameter larger than its critical diameter, evaluated at cloud top). Particles larger than this characteristic CCN are considered droplets. This definition of cloud droplets includes large CCN, which have not attained their critical diameter but are as large as activated drops (~ 1 μm), and does not include CCN that deactivate and become interstitial aerosol.

A film-breaking model is used to evaluate the effect of Film-Forming Compounds (FFCs). The model assumes that the presence of FFCs on the droplet surface decreases the condensation coefficient to 10^{-5}. The FFC is distributed among the aerosol by mass, which is appropriate for primary sources, whereas a surface area weighted distribution would be more appropriate for secondary organics that have entered the particles via condensation [*Feingold and Chuang*, 2002]. As the droplet grows, the film thickness decreases. At the point when a monolayer of FFC (0.5 nm thick) is achieved, the film breaks and the condensation coefficient immediately increases to 0.045. The FFC mass fraction is assumed equal to the base-case organic mass fraction, only for determining how long it takes the film to break. When FFCs are not present, a constant condensation coefficient of 0.045 is assumed, uniform for all particles. In addition, a simulation is performed with a constant condensation coefficient of 0.005, to represent the maximum potential effect of FFCs. A thermal accommodation coefficient of unity is assumed [*Shaw and Lamb*, 1999]. It should be noted that the structure and evolution of films, in addition to the size-resolved chemical composition of the films themselves, are so uncertain that the mechanism of the film-breaking model is highly speculative.

Empirical Correlations and Model Setup

The *Boucher and Lohmann* [1995] and *Gultepe and Isaac* [1999] relationships correlate cloud droplet number concentration with different aerosol characteristics. Employing both relationships consistently limits two of three key aerosol-cloud interaction parameters (sulfate mass, aerosol and droplet number). By specifying a total aerosol number concentration (N_{ap}) for each environment (Table 1.3), cloud droplet

number concentration (N_d) is calculated according to the empirical best fit relationships of *Gultepe and Isaac* [1999], as shown below.

$$N_d = \begin{cases} -595 + 298\log(N_{ap}) & \textit{Continental and Polluted} \quad (1.1a) \\ -273 + 162\log(N_{ap}) & \textit{Marine} \quad (1.1b) \end{cases}$$

The *Gultepe and Isaac* [1999] correlation (Equation (1.1a)) can be applied for N_{ap} up to 1,000 cm^{-3} and 1,500 cm^{-3} for the continental and polluted environments, respectively, since this is the range of the observations. Because of this, the continental and polluted fine particle number concentrations from *Whitby* [1978] are reduced so that the total aerosol number concentrations are 1,000 cm^{-3} and 1,500 cm^{-3}, respectively, while the mean diameter and mean dispersion are kept constant. Reducing the particle number concentration can be justified physically as dilution of an urban plume or vertical mixing of a continental air mass. Thus, the polluted case should be thought of as "diluted polluted" and the continental as "clean continental".

The cloud droplet number concentration, computed from Equation 1.1, is introduced into the *Boucher and Lohmann* [1995] correlation to obtain the total aerosol sulfate mass concentration (m_{SO4}):

$$m_{SO4} = 10^{\left\{\frac{\log(N_d)-2.21}{0.41}\right\}} \qquad \textit{Average} \qquad (1.2a)$$

$$m_{SO4} = 10^{\left\{\frac{\log(N_d)-2.06}{0.48}\right\}} \qquad \textit{Maritime} \qquad (1.2b)$$

Table 1.3 shows the base-case droplet number (N_d) and total aerosol sulfate mass (m_{SO4}) as constrained by these correlations.

Aerosol mass is often dominated by the larger particles, while number is dominated by smaller particles. Because of this, we need to be careful in how the sulfate is distributed throughout the size distribution. The sulfate mass determined by the *Boucher and Lohmann* [1995] correlation, m_{SO4}, is equal to the sum of the sulfate mass within each lognormal mode. The sulfate mass concentration of each lognormal mode (m_{SO4i}) is calculated according to Equations 1.3-1.5.

$$m_{SO4i} = \varepsilon_{SO4i} \rho_{api} V_i \tag{1.3}$$

where,

$$\rho_{api} = \frac{1}{\frac{\varepsilon_{oi}}{\rho_{oi}} + \frac{\varepsilon_{si}}{\rho_{si}} + \frac{\varepsilon_{insi}}{\rho_{insi}}} \tag{1.4}$$

The subscript s denotes properties of the soluble component, o stands for the organic component (which is slightly soluble), ins stands for the insoluble component, and the trailing subscript i indicates the modes (Nuclei, Accumulation and Coarse). In the absence of other soluble compounds, the sulfate mass fraction (ε_{SO4i}) is related to the soluble mass fraction (ε_{si}) by the ratio of their molecular weights (M_{SO4} / M_s), where M_s is the molecular weight of ammonium sulfate. For the marine coarse aerosol, the addition of NaCl yields: $\varepsilon_{si} = \varepsilon_{(NH_4)_2 SO_4 i} + \varepsilon_{NaCli}$ where $\varepsilon_{(NH_4)_2 SO_4 i} = \varepsilon_{SO4i} \left(\frac{M_{(NH_4)_2 SO_4}}{M_{SO4}} \right)$.

The volume concentration (V_i) is calculated from the number concentration (N_i), geometric mean diameter ($\overline{D}_{gi}$) and geometric standard deviation (σ_{gi}) for each mode, according to the following equation.

$$V_i = N_i\left(\frac{\pi}{6}\right)\exp\left(3\ln\overline{D}_{gi} + \frac{9}{2}\ln^2\sigma_{gi}\right) \qquad (1.5)$$

Given that a variety of combinations of m_{SO4i} can give m_{SO4}, we consider values that are consistent with observations. In this study, we set the fine particle mass fractions to the values reported by *Heintzenberg* [1989] (Table 1.2), and then compute the coarse mode sulfate mass fraction from the constraint $\Sigma m_{SO4i} = m_{SO4}$. If the computed coarse mode sulfate mass fraction is not within observed values, then we assume instead an observed coarse mode sulfate fraction and adjust the coarse mode number concentration so that $\Sigma m_{SO4i} = m_{SO4}$.

Adjustment of the chemical composition or number concentration of the coarse mode can be justified in two ways. First, coarse mode measurements are often the least certain of the three modes, due to limitations in the instrumentation [*Baron and Willeke*, 2001]. Second, the contribution of the coarse mode particles to cloud droplet number is negligible, on the order of 1-10 cm^{-3}. Therefore, given that unrealistic coarse particle sulfate mass fraction can strongly influence sulfate mass burden, it is preferable to first assign the sulfate mass for the fine particles and then attribute the remaining sulfate mass, given by the *Boucher and Lohmann* [1995] correlations, to the coarse particles.

Using the procedure outlined above, coarse mode sulfate mass fractions are calculated for the marine and polluted aerosol (keeping coarse mode number concentrations constant). The calculated coarse mode sulfate mass fraction for the polluted aerosol is 0.11, midway between the observed range, 0.02 and 0.25 [*Ramanathan et al*., 2001; *Neusüβ et al.*, 2002; *Finlayson-Pitts and Pitts*, 1986]. Coarse mode particles in the marine boundary layer are primarily composed of sea salt, with much smaller amounts of nitrates and mineral dust [*Fitzgerald*, 1991]. Sea salt consists of ~7.68% (by mass) sulfate [*Seinfeld and Pandis*, 1998], so that, in the absence of other mechanisms, the coarse mode mass fraction of sulfate should be less than 0.08 for the marine aerosol. Our analysis yields a coarse mode sulfate mass fraction of 0.01, which is slightly lower than expected.

The continental aerosol distribution used lacks sufficient coarse mode particles to yield a m_{SO4} consistent with the *Boucher and Lohmann* [1995] correlation. Increasing the coarse mode number concentration from 0.72 cm^{-3} to 4.1 cm^{-3} satisfies the constraint $\Sigma m_{SO4i} = m_{SO4}$. This change has a negligible impact on CCN and droplet number concentrations.

Results

Base-case Updraft Velocity

Ensuring that the aerosol chemistry and size distribution are consistent with observations is a necessary but not sufficient condition for the plausibility of our analysis. The base-case updraft velocity must also be consistent with observations; otherwise, the sensitivities calculated may not be representative of the ambient atmosphere, as they have

been shown to be strong functions of updraft velocity and chemical composition [e.g., *Rissman et al*., 2004]. The base-case updraft velocity is inferred, rather than prescribed, because updraft is highly uncertain, as it is both difficult to measure and highly variable.

Coalescence and entrainment may have affected observations of droplet number, although these processes are not explicitly addressed within the parcel model. However, these processes can only reduce droplet number. Thus, the calculated base-case updraft velocity actually represents the minimum cooling rate required to produce the number of cloud droplets that are predicted by the empirical correlations. Where entrainment does exist, this means that a greater updraft velocity is required to produce the observed number of droplets. A higher updraft is expected to enhance the relative sensitivity of cloud droplet number to surface tension effects [*Rissman et al*, 2004].

The base-case updraft velocity is determined iteratively. Updraft velocity is varied until cloud droplet number calculated from the cloud parcel model matches the *Gultepe and Isaac* [1999] and *Boucher and Lohmann* [1995] correlations. The resulting base-case updraft velocities are ~0.7-1.5 m s^{-1} for the continental case and ~2-3.5 m s^{-1} for the polluted case, which are within the expected range (e.g. 0-1 m s^{-1} for stratiform and ~1-17 m s^{-1} for continental cumulus clouds [*Seinfeld and Pandis*, 1998]). *Mason* [1971] found that updrafts in non-precipitating continental cumulus clouds are typically no greater than 5-7 m s^{-1}. The maximum parcel supersaturations for the continental and polluted base-cases are 0.7-0.8% and 1.2-1.4%, respectively. Supersaturations in the ambient atmosphere are usually less than 1% and almost never exceed 2% [*Seinfeld and Pandis*, 1998]. Although the base-case updraft velocities and maximum supersaturations are higher than average values measured *in situ*, this is expected. Within a single cloud,

the higher end of the updraft velocity spectrum is expected to control the total number of cloud droplets formed. Thus, when a single updraft is used to represent the production of cloud droplets, its intensity is expected to be larger than average, but still within the observed range. Thus, the base-case aerosol size distribution and chemical composition are reasonable representations of the ambient aerosol for the continental and polluted cases.

Surface tension depression from the presence of the organics is not considered for the base-case calculations; if surfactants were considered, the base-case updraft velocities would be cut in half and the maximum supersaturations would be reduced to 0.4-0.5% and 0.8-0.9%, for the continental and polluted cases, respectively.

If the condensation coefficient were increased from 0.045 to 1.0, the maximum supersaturation for the base-case does not change significantly, but the base-case updraft velocity doubles for both the continental and polluted cases. With a higher condensation coefficient, an increased rate of condensation in the initial stages of cloud formation leads to a lower cloud supersaturation, and thus a lower cloud droplet number. Since the droplet number is constrained, the required updraft velocity must increase in order to provide the same driving force for condensational growth.

The updraft velocity for the marine environment is expected to be lower than updraft velocities over continents. However, using the *Whitby* [1978] distribution, the base-case updraft velocity for the marine case is ~13 m s^{-1} (neglecting surface tension effects), which is apparently greatly overestimated. If we use a different size distribution from *Heintzenberg* [2000] and *Jaenicke* [1993] (Table 1.1), the base-case updraft velocity is reduced to 0.1-0.35 m s^{-1}. While the total number of aerosol particles remains nearly

the same as from *Whitby* [1978] (within 2%), this alternative particle size distribution has a larger proportion of particles in the accumulation mode, where the majority of CCN are found. The maximum parcel supersaturation for this new base-case is less than 0.5%, whereas using the *Whitby* [1978] remote marine distribution the maximum supersaturation was > 5%, which is not realistic for the atmosphere. Thus, we use the *Heintzenberg* [2000]/*Jaenicke* [1993] aerosol size distribution for the marine case in our analysis.

Heintzenberg [2000] grouped a total of 64 independent observations of marine fine aerosol size distributions from all over the world according to latitude (Table 1.1). Interestingly, the *Whitby* [1978] size distribution most closely approximates the latitude range 60-75^{o}S, in terms of the proportion of aerosol in the nuclei and accumulation modes. This latitude range is very remote, and in fact, *Whitby* [1978] actually describe the observations as representative of a "remote marine" environment. By comparison, the 24 independent observations of fine aerosol size distribution that are listed within the latitude range 15-60^{o}N by *Heintzenberg* [2000] are likely influenced by anthropogenic activities. Since, the *Boucher and Lohmann* [1995] and *Gultepe and Isaac* [1999] observations are from the northern hemisphere, we take an average of the size distribution parameters in the latitude range 15-60^{o}N from *Heintzenberg* [2000] to represent the fine marine aerosol in our analysis. The *Jaenicke* [1993] distribution is used to represent sea salt aerosol, which closely resembles the *Whitby* [1978] marine coarse mode aerosol distribution. With this new marine size distribution, the calculated coarse mode sulfate mass fraction increases from 0.01 to 0.05, which is closer to the expected value of ~0.08 for seawater.

Sensitivity of Droplet Number to Updraft Velocity

The observations covered by the correlations include both stratiform and cumuliform datasets. For this reason, we consider a range of updrafts between 0.1 and 5 m s^{-1} for the continental and polluted cases, and between 0.05 and 3 m s^{-1} for the marine case, to cover the expected variability of droplet number from dynamical effects in both cloud types [*Mason*, 1971].

For the updraft velocity sensitivity analysis, the cloud parcel model is run twice (first at a high updraft velocity and then at a low updraft velocity) for each of the three aerosol number concentrations (1.0, 0.75 and 0.50 times the base-case aerosol number concentration) and for each of the three environments (marine, continental and polluted). In these simulations, the organic component of the aerosol is not considered a surfactant, meaning that the surface tension remains constant as the droplet grows.

For the marine base-case (using the *Heintzenberg* [2000]/*Jaenicke* [1993] distribution), cloud droplet number varies from 91 to 336 cm^{-3} as a result of changes in updraft velocity (Figure 1.2). The maximum parcel supersaturation corresponding to the 3 m s^{-1} updraft velocity for this case is 1.25-1.5%, which is on the high end of observations. This indicates that either the high updraft is very unlikely, or it indicates the presence of an aerosol with a chemical composition and/or size distribution that differs significantly from the average. Increasing the condensation coefficient to 1.0 decreases the maximum supersaturation for 3 m s^{-1} updrafts to 0.9-1.1%. However, the number of droplets also decreases by 11-18%.

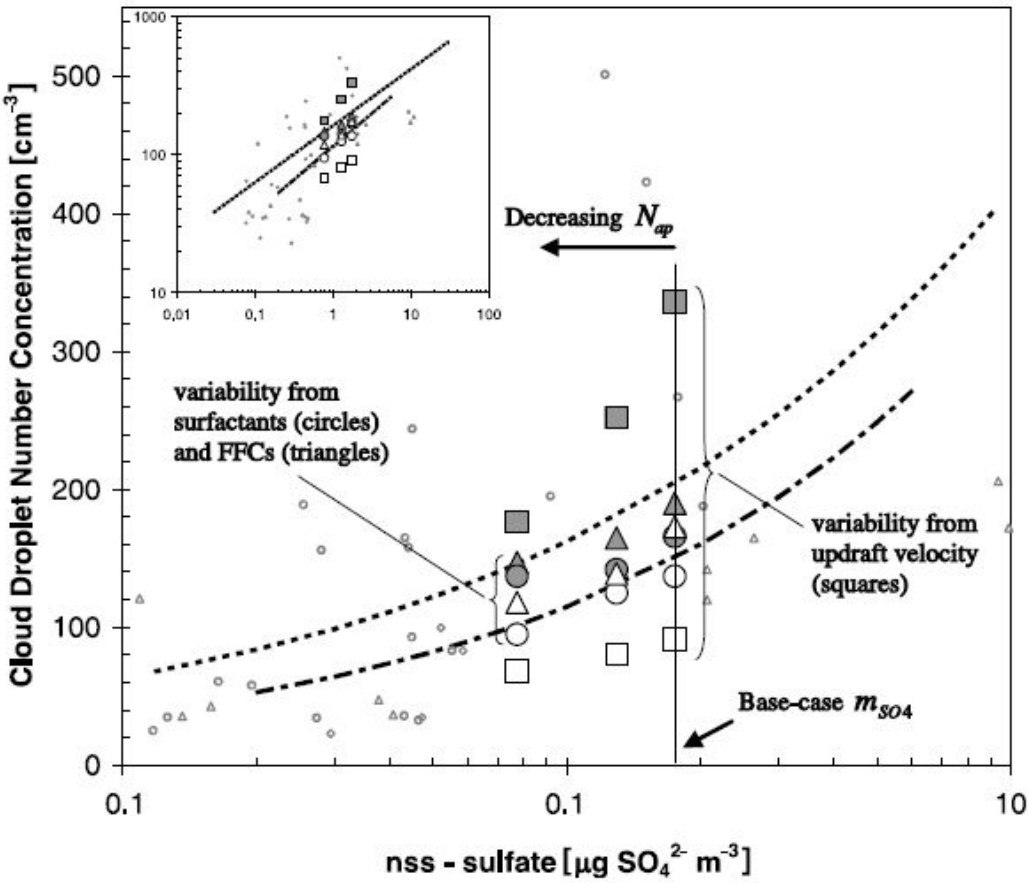


Figure 1.2. Marine cloud droplet number sensitivity to updraft velocity and chemical effects. Maritime observations, average correlation (dotted line), and maritime correlation (dash-dotted line) are from *Boucher and Lohmann* [1995]. Marine case cloud parcel model results for high updraft velocity (shaded squares), low updraft velocity (open squares), high organic mass fraction (shaded circles), low organic mass fraction (open circles), constant condensation coefficient (0.005, shaded triangles), and changing condensation coefficient (10^{-5}–0.045, open triangles) are overlaid on the observational data. The inset shows the full range of the observations on a log-log scale.

For the continental base-case, cloud droplet number varies from 112-510 cm^{-3} (Figure 1.3), and for the polluted base-case, cloud droplet number varies from 91-495 cm^{-3} as a result of changes in updraft velocity (Figure 1.4). For the continental case, this variability (~400 cm^{-3}) encompasses a majority of the scatter in the observations. However, for the polluted case, a significant fraction of the observations appear to be unexplained by the very large updraft variability.

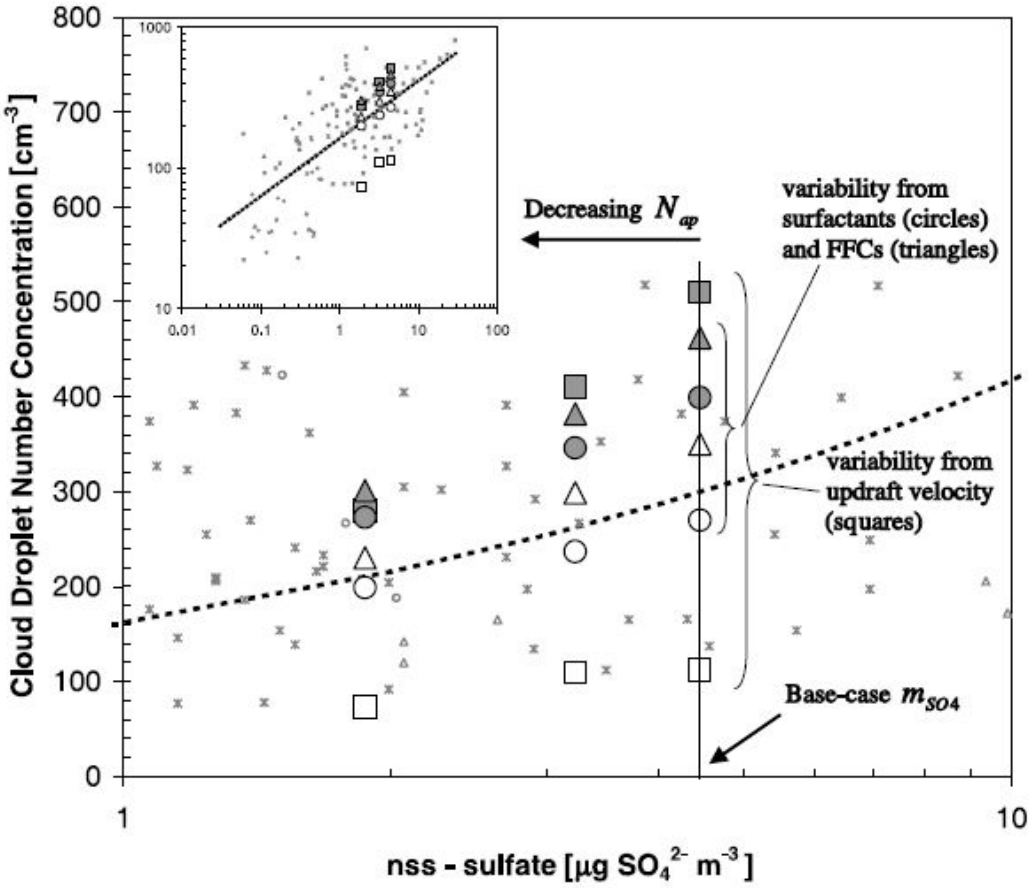


Figure 1.3. Same as Figure 1.2 but for continental aerosol with the average correlation and including all observations from *Boucher and Lohmann* [1995].

The maximum parcel supersaturations within 5 m s^{-1} updrafts are 1.6-1.9% and 1.7-2.0% for the continental and polluted cases, respectively. Changing the condensation coefficient to 1.0 changes the maximum supersaturations to 1-1.4% and 1.2-1.5%. However, the number of droplets decreases with this higher condensation coefficient, by 18-19% and 20-27%, respectively. Including the surface tension effect would also slightly decrease the maximum supersaturation within 5 m s^{-1} updrafts, but would result in an increase in cloud droplet number by up to 39%.

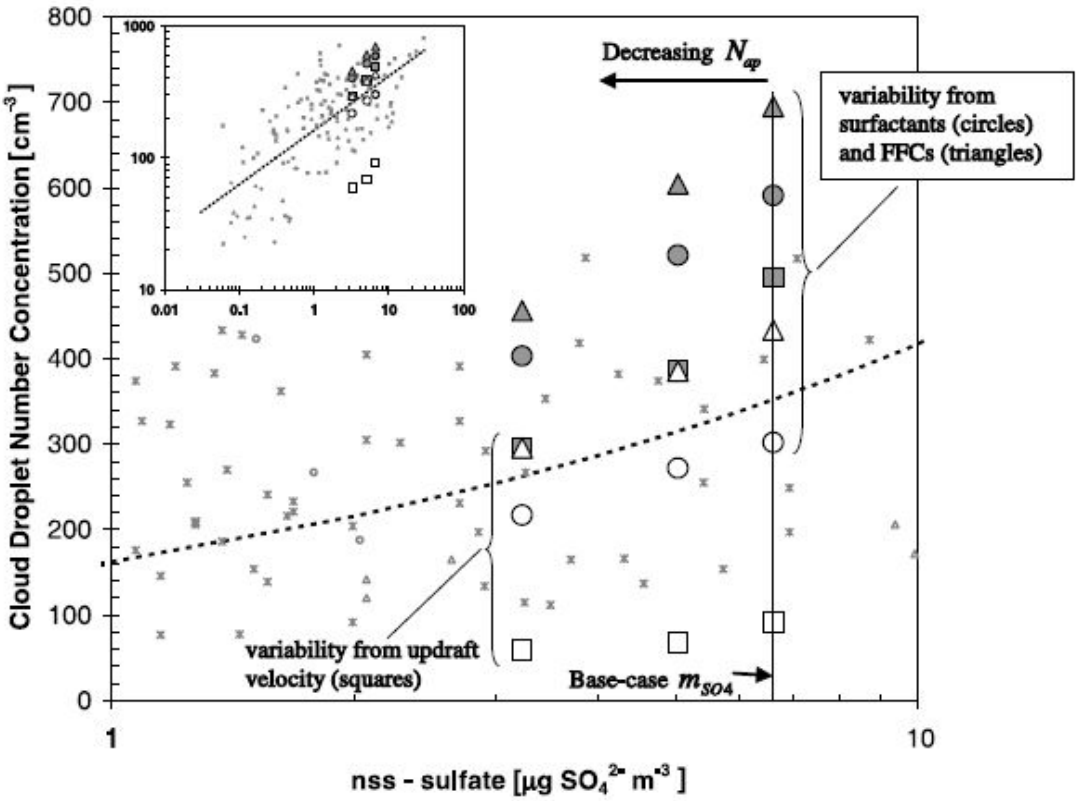


Figure 1.4. Same as Figure 1.3 but for polluted aerosol.

Sensitivity of Droplet Number to Chemical Effects

The cloud parcel model is run twice (high and low organic mass fractions specified in Table 1.4) for each of the three number concentrations and for each of the three aerosol types, to determine the sensitivity of cloud droplet number to surfactants. Only the fine particle organic mass fractions (which contribute the most to the CCN) are manipulated. These simulations utilize a constant condensation coefficient of 0.045 under the base-case updraft conditions.

Table 1.4. Base-case, lower and upper limit values for updraft velocity and fine particle organic mass fractions used for assessing the sensitivity to dynamical and chemical effects, respectively. The range of base-case updraft velocities for each aerosol type is for each of the three different aerosol number concentrations (100%, 75% and 50% of the base-case N_{ap} given in Table 3). The base-case fine particle organic mass fraction is from *Heintzenberg* [1989] and the upper limit in organic mass fraction is estimated from *Seinfeld and Pandis* [1998].

Aerosol type	**Updraft Velocity (m s^{-1})**			**Fine Particle Organic Mass Fraction**		
	Base	Lower	Upper	Base	Lower	Upper
Marine	0.1, 0.16, 0.35	0.05	3	0.11	0	0.41
Clean Continental	0.7, 1.0, 1.5	0.1	5	0.24	0	0.45
Diluted Polluted	2.0, 3.0, 3.5	0.1	5	0.31	0	0.61

Two additional simulations are performed to address the sensitivity of droplet number to a delayed condensational growth rate that may result from the presence of FFCs on the droplet surface. Surface tension effects are neglected for these simulations. First, the condensation coefficient is decreased by approximately one order of magnitude (from 0.045 to 0.005). Then a non-constant condensation coefficient is assessed using a film-breaking model, for which the lowered condensation coefficient (10^{-5}) changes to 0.045 when the film breaks. Three different aerosol number concentrations and three different aerosol types are assessed, at the base-case updraft velocity and base-case organic mass fraction.

For the marine base-case, increasing the organic mass fraction from 0 to 0.41 increases the number of cloud droplets from 137 to 166 cm^{-3} (Figure 1.2). This increase (~30 cm^{-3}) is mainly due to the effect of surface tension depression by the organic species, but is also influenced by the replacement of insoluble compounds with slightly soluble compounds. For the constant 0.005 condensation coefficient, the number of cloud droplets for the marine base-case increases further to 190 cm^{-3}. Using the film-

breaking model yields a droplet number of 173 cm^{-3}. Thus, the overall sensitivity of droplet number to chemical effects for the marine base-case is ~50 cm^{-3}. This is ~ 20% of the cloud droplet sensitivity from updraft variability.

As a result of surface tension effects, increasing the organic mass fraction increases the number of droplets from 270 to 399 cm^{-3} (continental base-case), and from 302 to 591 cm^{-3} (polluted base-case). The constant 0.005 condensation coefficient simulation increases the number of droplets further to 462 cm^{-3} and 695 cm^{-3}, for the continental and polluted base-cases, respectively. Thus, the cloud droplet number sensitivity to surfactants is 32-36% (continental) and 79-96% (polluted) of the sensitivity induced by updraft variability. However, it is important to note that the number of droplets resulting from surface tension effects can be much greater than the droplet number resulting from high updraft velocity. In other words, surface tension effects shifts the variability to higher droplet concentrations. This is typically the case for the polluted aerosol.

Surface tension effects increased the number of cloud droplets by 9-35% (marine), 30-33% (continental) and 54-68% (polluted) from the base-case. *Mircea et al* [2002] also found that the change in droplet number resulting from replacing insoluble compounds with surfactants was greater for the urban aerosol (110% increase in droplet number from the base-case) and rural aerosol (97% increase) than for marine aerosol (13% increase).

The constant 0.005 condensation coefficient simulations produce the greatest number of cloud droplets resulting from chemical effects. One of the interesting results is that the highest sensitivity of cloud droplet number to condensation coefficient appears

to be at or near typical observations of cloud droplet condensation coefficient (i.e. 0.045). Decreasing the condensation coefficient further (below 10^{-3}) has an almost negligible effect on droplet number, as most of the aerosol particles have already activated by this point. As mentioned previously, condensation coefficients on the order of 10^{-5} have been suggested for atmospheric aerosol influenced by FFCs. When the film-breaking model is introduced, the effect on droplet number is less pronounced than with a constant condensation coefficient; using the film-breaking model produces 91% (for the marine base-case), 76% (continental) and 62% (polluted) of the droplet number resulting from the constant condensation coefficient simulation. However, the droplet size dispersion increases significantly with the film-breaking model, as seen by *Feingold and Chuang* [2002]. In addition, for the polluted case, the increase in droplet number using the film-breaking model is nearly equivalent to the effect from a 5 m s^{-1} updraft.

Chemical and Dynamical Effects for Variable Aerosol Number

It is instructive to examine the variability from chemical and dynamical effects for other values of the aerosol number concentration. The striking feature for all three aerosol is the remarkable robustness of the variability; chemical effects remain significant, even when decreasing the aerosol number concentration by 25% and 50%. Since the *Gultepe and Isaac* [1999] observations of aerosol concentration only go up to 1,000 cm^{-3} (for continental aerosol) and 1,500 cm^{-3} (for the polluted aerosol), the correlations cannot be used to extrapolate the base-case updraft velocity, and we cannot assess the sensitivity for higher concentration plumes, although there are indications that the sensitivity may change under such conditions [*Rissman et al*, 2004].

In general, the relative sensitivity of cloud droplet number to surfactants increases as the aerosol number concentration decreases. This is most important for the marine case while it appears negligible for the continental and polluted cases. For the marine case, the sensitivity of droplet number to surfactants increases from 15% to 35% when the aerosol number concentration is reduced by 50% from the base-case. The marine base-case updraft velocities are on the most sensitive region of the relative organic surfactant sensitivity plot of *Rissman et al* [2004]. At the lower aerosol number concentration, a higher base-case updraft is required. As updraft velocity increases (0.1 m s^{-1} for the base-case N_{ap}, 0.16 m s^{-1} with 75% N_{ap} and 0.35 m s^{-1} with 50% N_{ap}) surface tension effects have a larger relative effect on droplet number, as expected from the results of *Rissman et al* [2004]. Conversely, the continental base-case updraft velocities are within a stable regime on the *Rissman et al* [2004] relative sensitivity plot, and an increase in the base-case updraft velocities causes only a slight increase in the relative sensitivity of droplet number to surfactants.

Implications for the Aerosol Indirect Effect

The first indirect effect is related to changes in cloud reflectivity, which can be characterized fairly well with two of the following three parameters: cloud liquid water content, effective radius and droplet number. By assuming a constant liquid water content (q_c), a change in droplet number (N_d) can be roughly related to a change in cloud reflectivity (R_c). The approximation, $\Delta R_c \sim 0.075\ \Delta \ln(N_d)$, is valid within 10% for an initial cloud reflectivity between 0.28 and 0.72 [*Seinfeld and Pandis*, 1998]. We

assume an initial R_c of 0.5 and plot the average percent change in R_c resulting from changes in cloud droplet number from updraft variability and chemical effects (Figure 1.5). This rough approximation shows that chemical effects, which includes both surface tension effects and changes in the condensation coefficient, may enhance cloud reflectivity by 4-10% , with respect to the base-case cloud droplet number. Comparatively, variations in updraft velocity are expected to enhance cloud reflectivity by 2-12%.

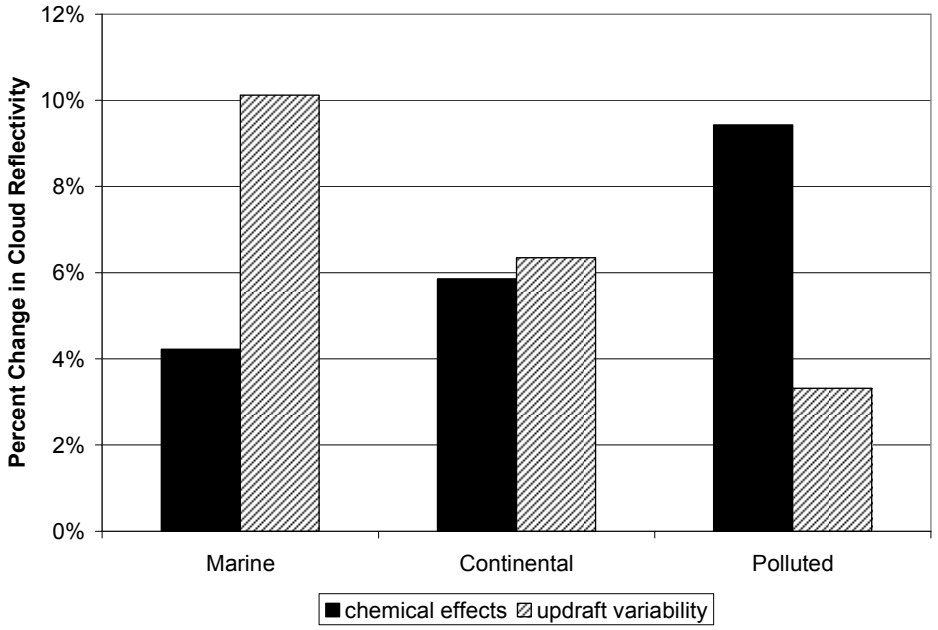


Figure 1.5. Estimated percent change in cloud reflectivity resulting from increases in droplet number from chemical effects and updraft variability, assuming a constant liquid water content and using a parameterization from *Seinfeld and Pandis* [1998]. An initial cloud reflectivity of 0.5 is assumed.

The second indirect effect, which is related to cloud lifetime, is an even greater challenge to quantify. We look at the rate of autoconversion, Q_{aut}, to represent the

second indirect effect, since autoconversion is the rate of initial generation of rain/drizzle from cloud water, which has direct implications for cloud lifetime. The *Khairoutdinov and Kogan* [2000] parameterization describes Q_{aut} as a function of droplet number and cloud liquid water content, $Q_{aut} = 1350 q_c^{2.47} N_d^{-1.79}$. Assuming a constant liquid water content, the increase in droplet number resulting from chemical effects suggests that Q_{aut} may decrease by 34-63%. This is due to the smaller sizes of the droplets, which have smaller settling velocities, thereby decreasing their rate of collision. For comparison, a high updraft velocity may decrease Q_{aut} by 19-76%.

Conclusions

This study assesses the variability in cloud droplet number that my result from the effect of organic species on surface tension and from the effect of film forming compounds on the water vapor condensation coefficient. The cloud droplet number variability is compared to the variability caused by uncertainties in updraft velocity. An inverse-modeling approach is employed for this task. Using a detailed numerical cloud parcel model, observed aerosol characteristics and correlations of cloud droplet vs. sulfate and cloud droplet vs. aerosol number, a most probable size distribution and updraft velocity for polluted and clean conditions is obtained. The variation in cloud droplet number from expected variations in aerosol chemistry and updraft velocity is then compared to the observed cloud droplet number scatter in the empirical aerosol sulfate-cloud droplet number correlation.

Three important results come out of this study. First, chemical effects can potentially have a significant effect on cloud droplet number concentration for conditions ranging from marine to polluted in the regions surrounding the North American continent and Atlantic ocean. Chemical effects may account for an average of 28% (marine), 49% (continental) and greater than 100% (polluted) of the variability in cloud droplet number, as compared to the variability from updraft velocity. This underlines the importance of including chemical effects within GCM assessments of the aerosol indirect effect, and challenges the common belief that the variability seen in empirical aerosol-cloud droplet number relationships is primarily from the highly variable cloud dynamics.

Another important finding is that surface tension effects may enhance the sensitivity of droplet number to variations in updraft velocity. Thus, the microphysical characteristics of clouds originating from organic CCN are likely more sensitive to the shape of the updraft velocity spectrum, than for clouds composed of purely inorganic CCN. Including surface tension effects increases the number of cloud droplets formed in 5 m s^{-1} updrafts by 55-63% for the polluted case and 30-39% for the continental case, and increases the number of cloud droplets formed in 3 m s^{-1} updrafts by 14-16% for the marine case. Thus, surface tension effects could help to explain the high end of the measured cloud droplet number variability.

Another significant finding is that the relative effect of organic species on cloud droplet number appears relatively insensitive to the aerosol number concentration for a wide range of aerosol and updraft conditions typically found in GCM simulations. This suggests that the relative importance of chemical effects on cloud droplet number may

not be masked by fluctuations in aerosol number concentration expected on the spatial scale of a typical GCM grid cell.

CHAPTER 2

MAPPING THE OPERATION OF THE DMT CONTINUOUS FLOW CCN COUNTER

This work thoroughly analyzes a new commercial instrument for measuring Cloud Condensation Nuclei (CCN), the Droplet Measurement Technologies Cylindrical Continuous-Flow Streamwise Thermal Gradient CCN Chamber (CFSTGC). This instrument can measure CCN concentrations at supersaturations from 0.07% to greater than 2%, at a 1 Hz sampling rate that is sufficient for airborne operation. Our analysis employs a fully coupled numerical flow model to simulate the water vapor supersaturation, temperature, velocity profiles and CCN growth in the CFSTGC for its entire range of operation (aerosol sample flow-rates 0.25-2.0 L min^{-1}, temperature differences 2-15 K and ambient pressures 100-1000 mb). The model was evaluated by comparing simulated instrument responses for calibration aerosol against actual measurements from an existing CCN instrument. The model was used to evaluate the CCN detection efficiency for a wide range of ambient pressures, flow rates, temperature gradients and droplet growth kinetics. Simulations overestimate the instrument supersaturation when the thermal resistance across the walls of the flow chamber is not considered. We have developed a methodology to determine the thermal resistance and temperature drop across the wetted walls of the flow chamber, by combining simulations and calibration experiments. Finally, we provide parameterizations for determining the thermal resistance, the instrument supersaturation and the optimal detection threshold for the optical particle counter.

Lance S, J. Medina, J.N. Smith, A. Nenes, Mapping the operation of the DMT Continuous Flow CCN counter, *Aeros. Sci. Techn*., 40 (4), 2006. Published [2006] Taylor & Francis.

Introduction

The fraction of aerosol that can become droplets in ambient clouds is known as Cloud Condensation Nuclei (CCN). Knowledge of CCN concentrations is fundamentally important for aerosol-cloud-climate interaction studies, because it provides the direct quantitative link between aerosol and clouds. Thermodynamic theory [*Köhler* , 1936] predicts the minimum supersaturation required for a particle to "activate" (or to become a cloud droplet), also known as the particle "critical supersaturation". The theory requires knowledge of particle chemical composition and dry particle size. In the presence of soluble gases, the composition of the gas phase may also be required. Although aerosol microphysical properties (such as particle size distribution and number concentration) can be measured rapidly, complete chemical analysis is more challenging due to the complexity and variability of ambient aerosol [*Saxena and Hildemann*, 1996]. When the physicochemical properties of the aerosol are unknown or incomplete, CCN concentrations are not available from theory and must be measured by exposing particles to a controlled water vapor supersaturation and counting the droplets that form. Observations of CCN are important for evaluating and constraining regional and global aerosol models, as well as global climate modeling simulations of the aerosol indirect effect. CCN measurements are also important for use with aerosol of known composition to study unresolved chemical effects and to test the theories regarding aerosol-cloud interactions.

Instruments that measure CCN can be classified by how they generate water vapor supersaturation, based on *i*) the nonlinear dependence of water vapor pressure upon temperature, or *ii*) the difference between water vapor diffusivity and thermal diffusivity.

The first type includes Static Diffusion Cloud Chambers (SDCC) [*Twomey*, 1963; *Lala and Jiusto*, 1977] and Continuous Flow Parallel Plate Diffusion Chambers (CFDC) [*Sinnarwalla and Alofs*, 1973; *Fukuta and Saxena*, 1979; *Hudson*, 1989; *Van Reken et al*, 2004], which have an applied temperature gradient perpendicular to the flow. The second type requires continuous, laminar flow, and a temperature gradient that is in the streamwise direction [*Hoppel et al*, 1979; *Chuang et al*, 2000; *Roberts and Nenes*, 2005]. Many of these designs have been theoretically analyzed using detailed numerical models by *Nenes et al* [2001].

Droplet Measurement Technologies (DMT; www.dropletmeasurement.com) has developed a new CCN counter based on the design of *Roberts and Nenes* [2005], which generates supersaturation in an axisymmetric flow by applying a temperature gradient in the streamwise direction. The goal of this study is to fully characterize and map the performance of the DMT design for the functional range of operating conditions, using computational fluid dynamics software in combination with measured instrument responses to single-component laboratory generated aerosol.

Instrument Description

The DMT Continuous-Flow Streamwise Thermal-Gradient CCN Counter (CFSTGC, Figure 2.1) is designed to operate on a ground-based or airborne platform and can generate supersaturations between 0.06% and above 2%. An ambient sample is introduced into the instrument, split into "sheath" and "aerosol" flows (typically with a sheath-to-aerosol flow ratio of 10). The sheath flow is filtered, humidified and heated, and provides a particle-free "blanket" of air within the CCN column that constrains the

particles to the centerline of the flow chamber. The cylindrical column measures 0.5 m in length, with an 11.5 mm inner radius and a wall thickness of 10.0 mm. The inner wall of the CCN column is wetted continuously by supplying 4 mL hr^{-1} (at the default "low" flow setting) of water onto a 2.5 mm thick porous ceramic material that lines the inner wall of the column. A positive temperature gradient is applied to the CCN column in the streamwise direction; the column is vertically oriented, with the flow moving from top to bottom. Water vapor supersaturation is generated within the CCN column, where the particles grow by condensation. Particles are considered droplets when they are large enough for detection by an optical particle counter (OPC) at the exit of the CCN column.

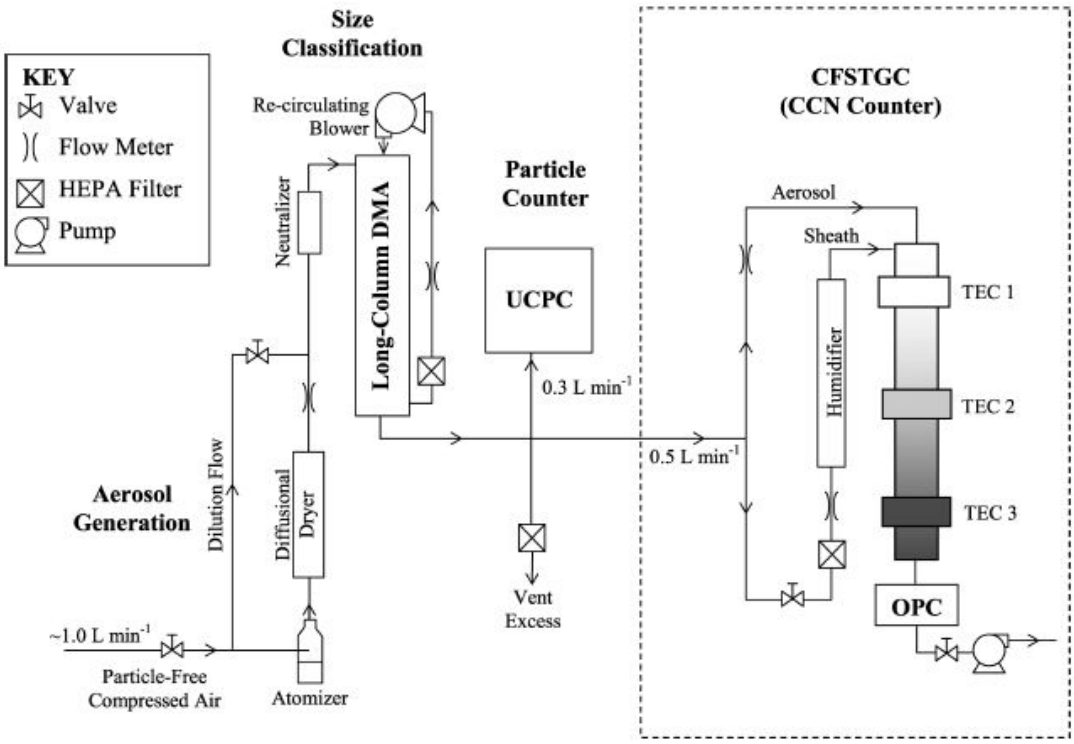


Figure 2.1. Schematic of the CFSTGC calibration setup. A schematic of the CFSTGC is also shown within the dotted line.

To generate supersaturation, the CFSTGC requires a temperature gradient in the streamwise direction and a continuous, laminar flow. When the flow is fully developed, heat and water vapor are transported in the radial direction by diffusion. Water vapor that is saturated with respect to the wall temperature diffuses faster than heat; thus the flow region is supersaturated with water vapor, since water vapor is continuously exposed to temperatures lower than at the wall [*Roberts and Nenes*, 2005]. Supersaturation is quasi-parabolic for a cross section of the CCN column, with the maximum supersaturation at the centerline of the column. Supersaturation is primarily controlled by the streamwise temperature gradient, total flow rate, and pressure. Once the flows have developed, the supersaturation of each streamline is nearly constant, reaching a slight maximum before the exit of the column because of the weak inverse dependence on absolute temperature [*Roberts and Nenes*, 2005]. The temperature gradient is maintained with three sets of thermal electric coolers (TECs) along the length of the column, and the flow rate is controlled via a proportional valve.

There is no direct way of controlling the temperature gradient of the wet inner walls that are responsible for generating supersaturation. Instead, the thermoelectric coolers control the temperature at the outer walls of the chamber. However, there is a temperature drop through the walls of the CFSTGC due to the continuous removal of heat at the inner wall by forced convection and evaporation, and due to the thermal resistance of the materials through which the heat must travel. As a result, the temperature gradient developed in the inner wall is smaller than applied by the TECs. If this temperature drop is not accounted for, the instrument supersaturation may be overestimated. The magnitude of this temperature drop depends on the instrument operating conditions. For

instance, a higher flow rate leads to greater forced convection at the inner wall surface, and thus a greater temperature drop through the walls of the column. A procedure for estimating this temperature drop is outlined later.

Instrument and Droplet Growth Models

The CFSTGC instrument model [*Roberts and Nenes*, 2005] numerically solves the equations that govern heat, mass and momentum transfer throughout the flow chamber. The model computes temperature, velocity and water vapor concentration profiles in the column. Inputs to the model are total volumetric flow rate (Q), sheath-to-aerosol flow ratio (SAR), pressure (P), and the inner wall streamwise temperature difference (ΔT_{inner}) between the exit and entrance (T_h' and T_c', respectively) of the column. For all atmospherically relevant measurements, the impacts of CCN growth on the gas phase water vapor and heat balance are negligible [*Nenes et al*., 2001; *Roberts and Nenes*, 2005]. Thus, the simulated supersaturation, velocity, and temperature profiles are used to compute the growth and activation of CCN as they flow through the chamber (with a user-defined size distribution and composition). Integration of the droplet growth equations is accomplished by the LSODE (Livermore Solver for ODEs) solver [*Hindmarsh*, 1983]. For more details refer to *Roberts and Nenes* [2005].

To analyze the CFSTGC, we vary ΔT_{inner}, Q, and P over their operational range and simulate the instrument performance for the combinations of these parameters given in Table 1. The maximum ΔT_{inner} and minimum Q are set to limit secondary flows developed by thermal buoyancy. The minimum ΔT_{inner} and maximum Q are limited by

the detectability of activated droplets and by the desire for establishing developed flow fields in the flow chamber, respectively. For all simulations considered, the temperature of the air (both sheath and aerosol flows) entering the column is 293 K, the SAR is 10 and the liquid water flow rate is 4 mL hr^{-1} (which corresponds to the "low" default setting in the instrument control software). The flow field is discretized into 100 grid points in the streamwise direction and 100 grid points in the radial direction.

For the simulations in this study, we consider CCN described by a single, broad lognormal mode of ammonium sulfate aerosol with a mean dry diameter of 0.07 μm, geometric dispersion of 2.0, and number concentration of 60 cm^{-3}. The water vapor condensation coefficient, α_c, is assumed to be 0.042 [*Feingold and Chuang*, 2002]. An additional simulation is run with α_c = 0.005 [*Chuang*, 2003], to explore the instrument response to slowly growing CCN. Simulations with α_c > 0.042 are not considered, as the instrument performance would always improve.

Characterization of Wall Thermal Resistance

Definition of Thermal Efficiency

Supersaturation strongly depends on the inner wall streamwise temperature difference ($\Delta T_{inner} = T_h' - T_c'$) which may be a fraction of the temperature difference imposed by the TECs at the outer wall of the column ($\Delta T_{outer} = T_h - T_c$), where T_h is the (hot) temperature at the exit and T_c is the (cold) temperature at the entrance of the flow chamber (Figure 2.2). The temperature drop across the walls is expressed in terms of a non-dimensional thermal efficiency, η, as:

$$\eta = (T_h^{'} - T_c^{'}) / (T_h - T_c) = (\Delta T_{inner} / \Delta T_{outer}) \tag{2.1}$$

$\eta = 1$ corresponds to a situation when there is no temperature drop across the walls, while anything less than unity implies that the supersaturation in the instrument is lower than that inferred from the TEC temperature readings. The thermal efficiency varies with the operating conditions, and must be determined to predict the real supersaturation developed in the instrument. η can be determined if the overall thermal resistance, R_T, is known. R_T is a material property, and is not expected to change significantly over the temperature range that will be used in the CFSTGC.

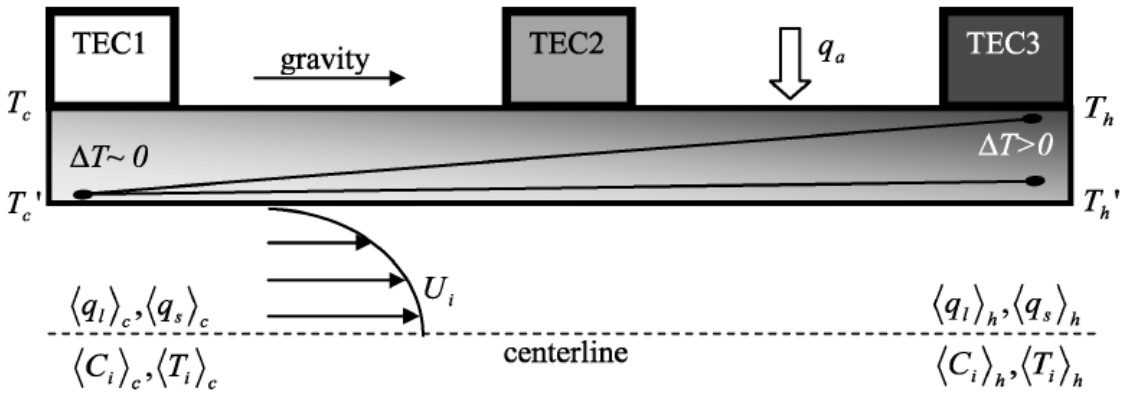


Figure 2.2. Cross-sectional representation of the CCN column turned on its side. The temperature drop through the wall (ΔT) increases as the flow approaches the exit of the column. Thus, the effective streamwise temperature difference applied to the air ($\Delta T_{inner} = T_h' - T_c'$) is less than the outer wall streamwise temperature difference that is controlled by the Thermal Electric Coolors (TECs) ($\Delta T_{outer} = T_h - T_c$).

Experimental Determination of Thermal Efficiency

Calibration experiments are performed to constrain the thermal efficiency of the CCN column under specific conditions. Figure 2.1 shows the experimental setup. An ammonium sulfate or sodium chloride aqueous solution is atomized (using ~1.0 L min^{-1} of dry filtered air), passed through a diffusional drier, diluted and then classified by a Differential Mobility Analyzer (DMA) (TSI, Inc., model 3081) with 10.0 L min^{-1} re-circulating sheath flow. While keeping the DMA voltage constant, the classified flow is sampled by an Ultrafine Condensation Particle Counter (UCPC) (TSI 3025A) and the CFSTGC. Over a period of 5 minutes, the concentration of total particles (or, condensation nuclei, CN) and CCN are measured, and the average activation fraction (CCN/CN) is computed. This process is repeated over many classified particle sizes, so that CCN/CN ranges from zero to unity. The resulting CCN/CN curve, or "activation curve," exhibits a characteristic sigmoidal shape (e.g., Figure 2.3). The instrument supersaturation is then equal to the critical supersaturation of the particle (calculated from Köhler theory) obtained from the activation curve at a 50% activated fraction.

Activation curves using NaCl and $(NH_4)_2SO_4$ (Figure 2.3) were generated under the following operating conditions: 5.35 K applied streamwise temperature difference, 0.5 L min^{-1} total flow rate, 10 SAR and ~0.8 atm pressure. To avoid coincidence counting errors in the UCPC, the total particle concentration is always less than 2000 cm^{-3}. A Scanning Mobility Particle Sizer (SMPS) was used briefly to validate the size of the classified aerosol particles entering the CFSTGC; the classified particle size was confirmed by the SMPS system to within 1 nm. When applying Köhler theory, thermodynamic properties are calculated at the outer wall mean temperature. The

sigmoidal shape of the activation curve is marred by a second aerosol mode composed of doubly charged particles (less than 10% of the classified aerosol) that have a much lower critical supersaturation than singly charged particles of the same mobility (because the former are physically larger). Using a van't Hoff factor of 2 for NaCl and 3 for $(NH_4)_2SO_4$ and a dynamic shape factor of 1.02 for NaCl and 1.0 for $(NH_4)_2SO_4$ (Zelenyuk et al, in review), the instrument supersaturation for the experiments shown in Figure 2.3 is calibrated to be $0.255 \pm 0.015\%$. Most of the variability can be attributed to the calibrations from one day, April 15th.

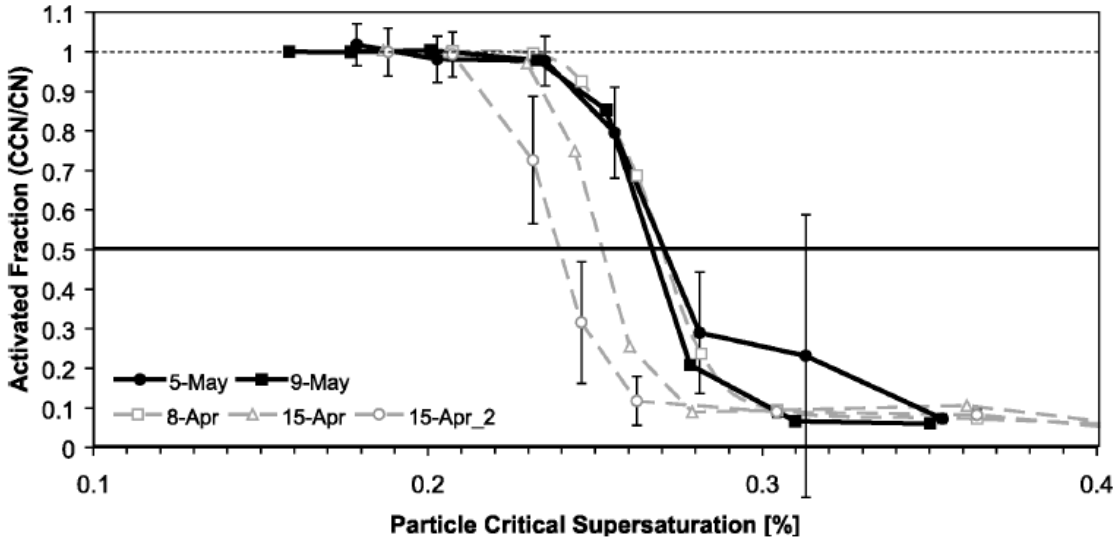


Figure 2.3. Activation curve for $(NH_4)_2SO_4$ (grey dotted) and NaCl (black solid) aerosol with $\Delta T_{outer} = 5.35$K, $Q = 0.5$ L min^{-1} and $P = 0.8$ atm. The activation curves are used to estimate the instrument supersaturation and to calibrate the thermal resistance of the CFSTGC walls. The instrument supersaturation is determined by the inflection point of the activation curve (at 50% activated fraction). Error bars show one standard deviation in the activated fraction, for both the highest and lowest supersaturation calibrations.

Although the supersaturation uncertainty is small, it is important to understand its source. Variability in the atomized aerosol size distribution can account for only up to ~20% of the range in the calibrated supersaturation. Measured outer wall temperature fluctuations (< 0.1°C) can only account for 1%. Additional uncertainty may be associated with changes in the liquid water drip rate. An increase in the water drip rate may remove more heat from the column walls, thereby potentially lowering the inner wall temperature and supersaturation. Furthermore, changes in the wetting efficiency will change the void fraction within the ceramic lining, which can have a notable impact on the thermal resistance.

Simulations suggest that, for the conditions of the calibration experiments, the supersaturation should be between 0.34% and 0.36% if the wall thermal resistance is neglected. To reconcile observed with simulated supersaturation, ΔT_{inner} must be 4.1 ± 0.25 K rather than the ΔT_{outer} of 5.35 K. Comparing ΔT_{outer} and ΔT_{inner} via Equation 2.1, η is equal to 75 ± 4%.

η is expected to vary with operating conditions, however the thermal resistance is not. Thus, using the above calibration experiments to estimate the thermal resistance, we can then use the instrument model to predict the thermal efficiency over a wide range of operating conditions. Additional calibration experiments at a higher flow rate and temperature gradient will further constrain our thermal resistance calculations. A procedure for estimating the thermal resistance is described later.

Theoretical Determination of Thermal Efficiency

A simple heat transfer model can be used to calculate the thermal resistance through the wetted walls. At steady state, conservation of energy dictates that the enthalpy increase in the gas phase (from the entrance to the exit of the column) is equal the heat applied at the outer wall (q_a), as shown in Equation 2.2.

$$\left[\langle q_l \rangle_h - \langle q_l \rangle_c\right] + \left[\langle q_s \rangle_h - \langle q_s \rangle_c\right] = q_a \tag{2.2}$$

where q_s is the sensible heat of the water and air, q_l is the latent heat from the evaporation of water, and the subscripts c and h indicate the entrance (cold) and exit (hot) of the CFSTGC, respectively.

The latent heat from the evaporation of water from the column walls is given by,

$$\Delta q_l = \langle q_l \rangle_h - \langle q_l \rangle_c = \Delta H_v \left[\left\langle \dot{m}_{H_2O}(z) \right\rangle_h - \left\langle \dot{m}_{H_2O}(z) \right\rangle_c\right] \tag{2.3}$$

where $\dot{m}_{H2O}$ is the mass flow of water vapor in the streamwise direction and ΔH_v is the enthalpy of vaporization for liquid water. The mass flow of water vapor, $\dot{m}_{H2O}(z)$, is calculated from the simulations as

$$\dot{m}_{H2O}(z) = 2\pi M_w \int_0^R rU(r,z)C(r,z)dr \tag{2.4}$$

where $U(r,z)$ is the axial velocity, $C(r,z)$ is the water vapor mass concentration, M_w is the molecular weight of water, and z and r are the axial and radial coordinates, respectively.

The sensible heat, $\Delta q_s = \left[\langle q_s \rangle_h - \langle q_s \rangle_c\right]$, is calculated as follows,

$$\Delta q_s = 2\pi \int_0^R \left[\left\langle C_{pm}(r,z)\dot{m}(r,z)T(r,z)\right\rangle_h - \left\langle C_{pm}(r,z)\dot{m}(r,z)T(r,z)\right\rangle_c\right] r dr + \dot{m}_w C_{pw}(T_h^{'} - T_c^{'}) \tag{2.5}$$

where $\dot{m}(r,z)$ is the mass flow of air in the streamwise direction, $C_{pm}(r,z)$ is the heat capacity of moist air, $T(r,z)$ is the air temperature, $\dot{m}_w$ is the mass flow of liquid water through the column, C_{pw} is the liquid water heat capacity and $(T_h^{'} - T_c^{'})$ is the streamwise temperature difference at the inner-wall surface. The last term in Equation 5 expresses the heat transferred to the liquid water film.

Using the ideal gas law, $\dot{m}(r,z)$ is given by,

$$\dot{m}(r,z) = U(r,z)\left(\frac{P(r,z)M_a}{RT(r,z)}\right) \tag{2.6}$$

where M_a is the average molecular weight of moist air, $P(r,z)$ is the absolute pressure and R is the universal gas constant.

The heat capacity of moist air, $C_{pm}(r,z)$, is calculated from the dry air heat capacity, $C_p(r,z)$, and the heat capacity of water vapor, $C_{pw}(r,z)$ [*Smith et al*, 1996]:

$$C_{pm}(r,z) = C_p(r,z)\left(1 - \frac{\dot{m}_{H2O}(r,z)}{\dot{m}(r,z)}\frac{M_a}{M_w}\right) + C_{pw}(r,z)\left(\frac{\dot{m}_{H2O}(r,z)}{\dot{m}(r,z)}\frac{M_a}{M_w}\right) \tag{2.7}$$

$$C_p(r,z) = (3.355 + 0.000575T(r,z) - 1600T(r,z)^{-2})R \tag{2.8}$$

$$C_{pw}(r,z) = (3.470 + 0.00145T(r,z) + 12100T(r,z)^{-2})R \tag{2.9}$$

Once the sensible and latent heats are calculated, q_a can be calculated via Equation 2.2. This energy is applied to the outside of the column, travels through the aluminum walls, porous ceramic lining and liquid water film, evaporates water on the inner surface of the column and heats the gas phase. The applied energy is related to the inner wall temperature by using the equation for conductive heat transfer, which, for cylindrical coordinates, is given by [*Kreith and Bohn*, 1997],

$$q_a = \left[2\pi L k \frac{T_o - T_i}{\ln(r_o / r_i)}\right]_{Al} = \left[2\pi L k \frac{T_o - T_i}{\ln(r_o / r_i)}\right]_{c} = \left[2\pi L k \frac{T_o - T_i}{\ln(r_o / r_i)}\right]_{H2O} \tag{2.10}$$

where the subscripts i and o represent the inner and outer radius (r) and temperature (T) of the aluminum wall (Al), porous ceramic lining (c) and liquid water film ($H2O$) and k represents the corresponding thermal conductivity.

Solving Equation 2.10 in terms of the overall temperature drop through the wall (from the outer radius of the aluminum walls to the inner radius of the liquid water film),

$$q_a = (\overline{T} - \overline{T}')\left[\left(\frac{2\pi L k}{\ln(r_o / r_i)}\right)_{Al} + \left(\frac{2\pi L k}{\ln(r_o / r_i)}\right)_{c} + \left(\frac{2\pi L k}{\ln(r_o / r_i)}\right)_{H2O}\right] \tag{2.11}$$

where $\overline{T}$ is the mean outer wall temperature, which is measured and controlled, and $\overline{T}'$ is the mean inner wall temperature, which is calculated using the instrument model in accordance with the calibration results. The overall thermal resistance of the wall and wetted film, R_T, is then given by:

$$R_T = \left[\left(\frac{\ln(r_o / r_i)}{k}\right)_{Al} + \left(\frac{\ln(r_o / r_i)}{k}\right)_{c} + \left(\frac{\ln(r_o / r_i)}{k}\right)_{H2O}\right]\frac{1}{2\pi L} \tag{2.12}$$

Thus, to obtain the thermal resistance from the calibrations, we must know the mean inner and outer wall temperature and the total applied energy.

$$R_T = \frac{(\overline{T} - \overline{T}')}{q_a} \tag{2.13}$$

From our calibration experiments, the calculated thermal resistance ranges from 2.7 K W^{-1} to 4.6 K W^{-1}, with an average of ~2.7 K W^{-1}. These values are for a liquid water drip rate of 4 mL hr^{-1} (the stated flow rate in the instrument hardware manual for the "low" peristaltic pump setting). However, due to changes in the peristaltic pump speed, the liquid water drip rate may have been higher for some of the calibrations. To estimate the effect on thermal resistance we doubled the liquid water drip rate in the

calculations for those experiments. With an 8 mL hr^{-1} liquid water drip rate, the range in thermal resistance becomes 2.7 K W^{-1} to 2.9 K W^{-1}, with an average of 2.3 K W^{-1}.

We performed additional calibration experiments with a higher flow rate and a higher temperature gradient, respectively, to confirm that the thermal resistance is within this expected range. With a flow rate of 0.5 L min^{-1} and a ΔT_{outer} of 7.9 K, the thermal efficiency is 78%, resulting in a calculated thermal resistance of 2.1 K W^{-1} (with 4 mL hr^{-1} assumed water drip rate) and 2.9 K W^{-1} (with 8 mL hr^{-1} assumed drip rate). Increasing the flow rate to 0.6 L min^{-1}, with a ΔT_{outer} of 5.35 K, the thermal efficiency is 71%, with a calculated thermal resistance of 2.1 – 2.4 K W^{-1}.

If indeed the decrease in instrument supersaturation is from the thermal resistance across the chamber wall, then the calibrated thermal resistance should be close to that calculated with Equation 2.12. With a wall thickness ($\delta_{Al} = (r_o - r_i)_{ss}$=10 mm), porous ceramic lining thickness (δ_c=2.54 mm), water film thickness (δ_{H2O}=2.54 mm), thermal conductivity of ceramic (k_c=4.2 W m^{-1} K^{-1} for 'zeramic', www.prgtech.com), thermal conductivity of water (k_{H2O}=0.6 W m^{-1} K^{-1}) and aluminum (k_{Al}=238 W m^{-1} K^{-1}) [*Kreith and Bohn*, 1997], and column inner radius and length (R=11.5 mm and L=0.5 m, respectively), the expected thermal resistance is R_T=0.2 K W^{-1}, tenfold less than calibrations indicate. However, the column is not quite as simple as Equation 2.12 implies; since the walls are smooth and the ceramic is porous, there is always a "contact resistance" between the aluminum walls and the porous ceramic lining, which could be significant [*Kreith and Bohn*, 1997]. We approximate the effect of a contact resistance by adding a thin "air layer" in series with the ceramic (δ_{air}=1 mm, k_{air} = 0.0258 W m^{-1}

K^{-1} [*Kreith and Bohn*,1997]), and the expected thermal resistance increases to 1.2 K W^{-1}. Air bubbles, or non-uniform wetting of the ceramic throughout its whole volume would have a similar effect on the thermal resistance. Any departure from the ideal smooth contact of materials or uniform material properties is expected to increase the thermal resistance; hence, the thermal resistance calculated directly from Equation 2.12 is expected to be a lower estimate.

Mapping Thermal Efficiency

To map the thermal efficiency over a wide range of operating conditions, we first specify ΔT_{inner}, since this is required by the instrument model. The heat transfer model, combined with the numerical simulation of the flow field, is used to determine the total energy, q_a, applied to the air and water flowing through the column. The thermal resistance, R_T, obtained from calibration experiments is used with Equation 2.13 to determine ΔT_{outer}, as

$$\Delta T_{outer} = \Delta T_{inner} + 2\left[\left(T_c^{'} - T_c\right) + q_a R_T\right] \tag{2.14}$$

Both T_c and $T_c^{'}$ are known, as they are measured. With ΔT_{outer} known, thermal efficiency can then be calculated from Equation 2.1.

Table 2.1. Input Variables to the CFSTGC instrument model: pressure (P, atm), inner wall streamwise temperature difference (ΔT_{inner}, K) and total volumetric flow-rate (Q, L min^{-1})

Property	Values considered							
P	0.1	0.4	0.7	1.0				
ΔT_{inner}	2.0	5.25	8.5	11.75	15.0			
Q	0.25	0.5	0.75	1.0	1.25	1.5	1.75	2.0

The instrument model is run using the calibrated thermal resistance to determine thermal efficiency for all combinations of the operating conditions listed in Table 2.1. Although ΔT_{inner} is needed in order to perform the heat transfer calculations, it is much more convenient to have a direct estimate of thermal efficiency as a function of ΔT_{outer}. In order to determine this relationship explicitly, we have performed a multivariate regression of the simulations (R^2=0.99):

$$\eta = A_1 P + A_2 Q + A_3 T_c' + A_4 \Delta T_{outer} + A_5 P^2 + A_6 P^3 + A_7 Q^2 + A_8 Q^3 + A_9 T_c' + A_{10}(T_c' - 293K)/Q + A_{11}\Delta T_{outer}^{\ 2} + A_{12}\Delta T_{outer}^{\ 3} + A_{13} \quad (2.15)$$

where Q is the total volumetric flow rate, P is the absolute pressure within the column and T_c' is the temperature of the air at the entrance of the column. Aside from providing a convenient means for explicitly addressing thermal efficiency in terms of ΔT_{outer}, the regression can be used in place of the instrument model, which may not be readily available to the instrument operator. Thus, the parameterization is provided as a convenience to the user, by reducing many computationally intensive calculations to a

single algebraic equation. It should be noted that Equation 2.15 may be applied only for instruments with the same physical specifications as reported here, and extrapolation beyond the range of operational conditions used to generate the regression is not recommended.

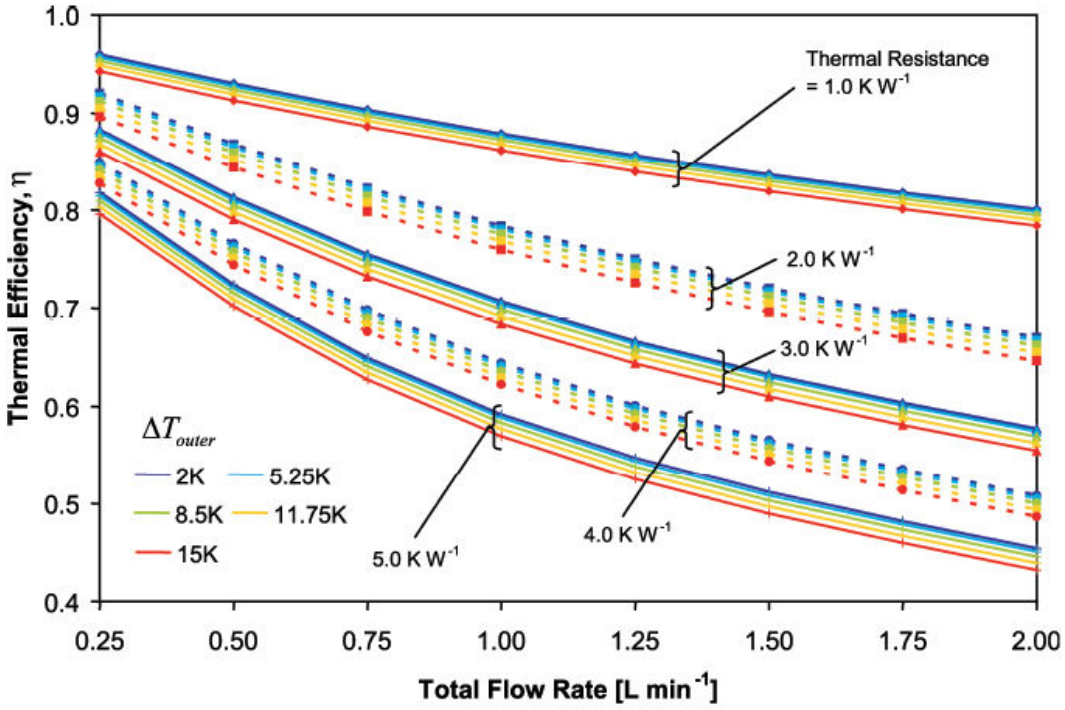


Figure 2.4. Thermal Efficiency through the walls of the CFSTGC versus total flow rate, for a given ΔT_{outer} (indicated by color) and R_T. Dotted and solid lines are to easily distinguish between different values of thermal resistance. ΔT_{inner} can be calculated by multiplying η by ΔT_{outer}. Pressure is 1 atm and a SAR of 10 is used.

To include the effect of thermal resistance, we have performed the regression of thermal efficiency (Equation 2.15) multiple times using different values of thermal resistance (1.0-5.0 K W^{-1}), each with an $R^2 > 0.99$. Each value for thermal resistance produces a different set of coefficients. Then we performed polynomial regression of the coefficients with respect to thermal resistance, using the lowest order that results in an R^2

> 0.995. The result is a series of 13 coefficients, many of which are in terms of thermal resistance (Table 2.2), which are then used in Equation 2.15 to estimate thermal efficiency. Figure 2.4 shows the thermal efficiency as a function of Q and ΔT_{outer}, for different values of thermal resistance, at 1 atm pressure and an inlet temperature of 293 K. The thermal efficiency ranges from 40% to 95%, and is most sensitive to Q and R_T, with a weaker dependence on ΔT_{outer}, T_c' and P. The pressure and inlet temperature dependences are not shown in Figure 2.4, but can be calculated via Equation 2.15. The parameterization duplicates the full simulations to within 0.8% (absolute) of the thermal efficiency, for the given range in operating conditions.

Table 2.2. Regression coefficients for Equation 2.15. R_T is the thermal resistance [K W^{-1}]

Coefficient	Regression	Units
A_1	$1.49 \times 10^{-3} R_T^2 - 1.09 \times 10^{-2} R_T - 3.78 \times 10^{-2}$	atm^{-1}
A_2	$1.54 \times 10^{-2} R_T^2 - 2.14 \times 10^{-1} R_T + 9.66 \times 10^{-2}$	min L^{-1}
A_3	$-2.63 \times 10^{-7} R_T^2 + 3.56 \times 10^{-6} R_T + 1.04 \times 10^{-3}$	K^{-1}
A_4	$9.59 \times 10^{-5} R_T^2 - 6.72 \times 10^{-4} R_T - 4.63 \times 10^{-5}$	K^{-1}
A_5	2.51×10^{-2}	atm^{-2}
A_6	-6.75×10^{-3}	atm^{-3}
A_7	$-4.83 \times 10^{-3} R_T^2 + 9.82 \times 10^{-2} R_T - 1.03 \times 10^{-1}$	min^2 L^{-2}
A_8	$-1.41 \times 10^{-2} R_T + 1.94 \times 10^{-2}$	min^3 L^{-3}
A_9	-1.40×10^{-5}	K^{-2}
A_{10}	$9.66 \times 10^{-5} R_T^2 - 9.90 \times 10^{-4} R_T + 2.68 \times 10^{-3}$	L K^{-1} min^{-1}
A_{11}	-5.20×10^{-5}	K^{-2}
A_{12}	1.00×10^{-6}	K^{-3}
A_{13}	$-4.21 \times 10^{-3} R_T^2 + 1.97 \times 10^{-2} R_T + 1.90$	unitless

With our calibrated thermal resistance of 3.5 K W^{-1}, the thermal efficiency ranges from 50% to 85%, corresponding to a maximum temperature drop through the CFSTGC

walls ($T_h - T_h^{'}$) from 0.25 K to over 7.0 K (assuming that the inner and outer wall temperatures are equal at the inlet). With a flow rate of 1 L min^{-1} and ΔT_{outer} of 11.75 K, ΔT_{inner} is 4.0 K lower (7.75 K). Thus, for this example the maximum temperature drop through the walls ($T_h - T_h'$) is 4.0 K, and a supersaturation of 1.4% is generated with ΔT_{inner} = 7.75 K. Another simulation using $\Delta T_{inner} = \Delta T_{outer}$ = 11.75 K (i.e., neglecting thermal resistance) predicts an instrument supersaturation of 2.2%, resulting in a 0.8% absolute overestimate in supersaturation.

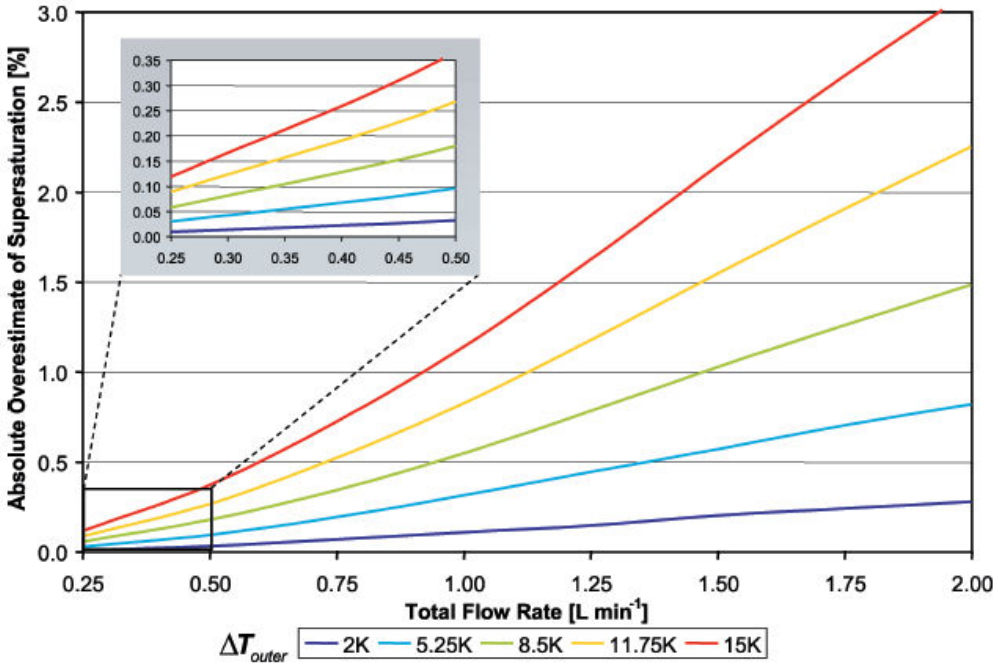


Figure 2.5. Absolute overestimate of supersaturation resulting when thermal efficiency is neglected, as a function of flow rate and ΔT_{outer} (represented by color). All simulations are at 1 atm pressure, SAR of 10 and with a thermal resistance of 3.5 K W^{-1}.

Figure 2.5 summarizes the overestimate in supersaturation that results from neglecting thermal efficiency, as a function of flow rate and ΔT_{outer}, at 1 atm pressure,

293 K inlet temperature and with a thermal resistance of 3.5 K W^{-1}. The overestimate in supersaturation can be as large as 3% (absolute difference) at high flow rates and temperature gradients.

Mapping Supersaturation

We parameterize the instrument supersaturation based on the inner wall temperatures, using multivariate nonlinear regression. The scaling analysis from *Roberts and Nenes* [2005] approximates the functional dependence of supersaturation upon the instrument operating conditions (for fully developed flow, temperature and concentration fields) as,

$$S \approx \frac{B_1 \Delta T_{inner} QP}{\left(\overline{T}' - \frac{B_2 \Delta T_{inner} QP}{\overline{T}'(B_3 + B_4 \overline{T}')} \right)^2} \left(\frac{1}{\overline{T}'(B_3 + B_4 \overline{T}')} - \frac{1}{B_5 \overline{T}'^{1.94}} \right) \tag{2.16}$$

where B_1, B_2, B_3, B_4 and B_5 are regression parameters. We use the mean temperature of the inner wall, $\overline{T}' = (T_h' + T_c')/2$, as the representative instrument temperature, and we use ΔT_{inner} calculated from Equations 2.1 and 2.15. $\overline{T}'$ is calculated by solving for T_h' from Equation 2.1 (since T_c', ΔT_{outer} and η are known). We estimate the coefficients by fitting Equation 2.16 to the instrument model calculations. The coefficients are B_1 = 877 K m^{-1}, B_2 = 1.3 m^{-1}, B_3 = 3.75×10^{-4} J m^{-1} s^{-1} K^{-1}, B_4 = 1.27×10^{-5} J m^{-1} s^{-1} K^{-2} and B_5 = 2.24×10^{-5} N s^{-1} $K^{-1.94}$, respectively, yielding an R^2 of 0.998 with a standard error of 0.03% supersaturation (absolute). These coefficients are applicable for total flow rates less than

1.25 L min^{-1}. At higher flow rates, the temperature profile is not fully developed at the exit of the column, and the regression begins to stray from the detailed simulations. Extrapolating to flow rates above 1.25 L min^{-1} can result in a 20% overestimate of supersaturation. It should also be noted that the range of inlet temperatures, T_c', used to derive these coefficients is from 293 K to 310 K, and extrapolation beyond this range may result in undesirable error. The regression is also not recommended for pressures lower than 0.4 atm.

Recommended Procedure for Calibrating Thermal Resistance

It is expected that the thermal resistance will vary between instruments, and that the thermal properties of a single instrument may change over time. Since small changes in the thermal properties of the materials can have an important impact on supersaturation, a thermal resistance of 3.5 K W^{-1} should not be used for all DMT CFSTGC units. Rather, the following procedure should be used to characterize the thermal resistance of a given CFSTGC unit and to estimate the unit's thermal efficiency and supersaturation.

In the absence of the instrument model, the recommended procedure for mapping out the thermal efficiency is as follows: 1) Calibrate the instrument experimentally using classified aerosol. Infer the instrument supersaturation from the resulting activation curve. 2) Use the multivariate regression of supersaturation (Equation 2.16) as a proxy for the instrument model, to determine the ΔT_{inner} required to reproduce the calibrated supersaturation. Use ΔT_{inner} and the known ΔT_{outer} to calculate thermal efficiency at the calibration operating conditions via Equation 2.1. 3) Use the multivariate regression of

thermal efficiency (Equation 2.15) to determine the thermal resistance of the instrument. 4) With the thermal resistance known, Equation 2.15 can be used under any operating conditions to estimate the thermal efficiency and thus the true ΔT_{inner}. Equation 2.16 can then be used to estimate the instrument supersaturation.

Particle Growth and CCN Counting

CCN are counted by growing to a size large enough to be detected in the OPC. Overcounting will occur if the OPC detection threshold is within the size range of unactivated haze aerosol. Similarly, undercounting of CCN will occur if the OPC detection threshold is larger than the minimum activated droplet size. It is therefore important to determine the appropriate OPC detection threshold to avoid counting biases.

The Optimal OPC Detection Threshold

In determining the optimal OPC detection threshold, β, we employ the droplet growth model. We consider the growth of a broad lognormal aerosol distribution through each streamline of the aerosol flow. The OPC views droplets simultaneously from all streamlines; thus, even with a perfectly monodisperse aerosol, slightly different supersaturations and residence times for each streamline broadens the droplet size distribution measured by the OPC. The simulations are expressed as "growth curves," or in terms of the wet particle diameter at the exit of the flow chamber as a function of the particle critical supersaturation (which is related to dry particle size). Figure 2.6 shows a typical "growth curve" and visually demonstrates the criteria for a good OPC detection

threshold. Particles with critical supersaturations above the instrument supersaturation do not activate, and thus remain as interstitial haze aerosol, while those that do activate grow quickly to a much larger size. β occurs at the transition between these two aerosol modes, at the inflection point of the growth curve, and thus represents the minimum droplet size at the outlet of the CCN column.

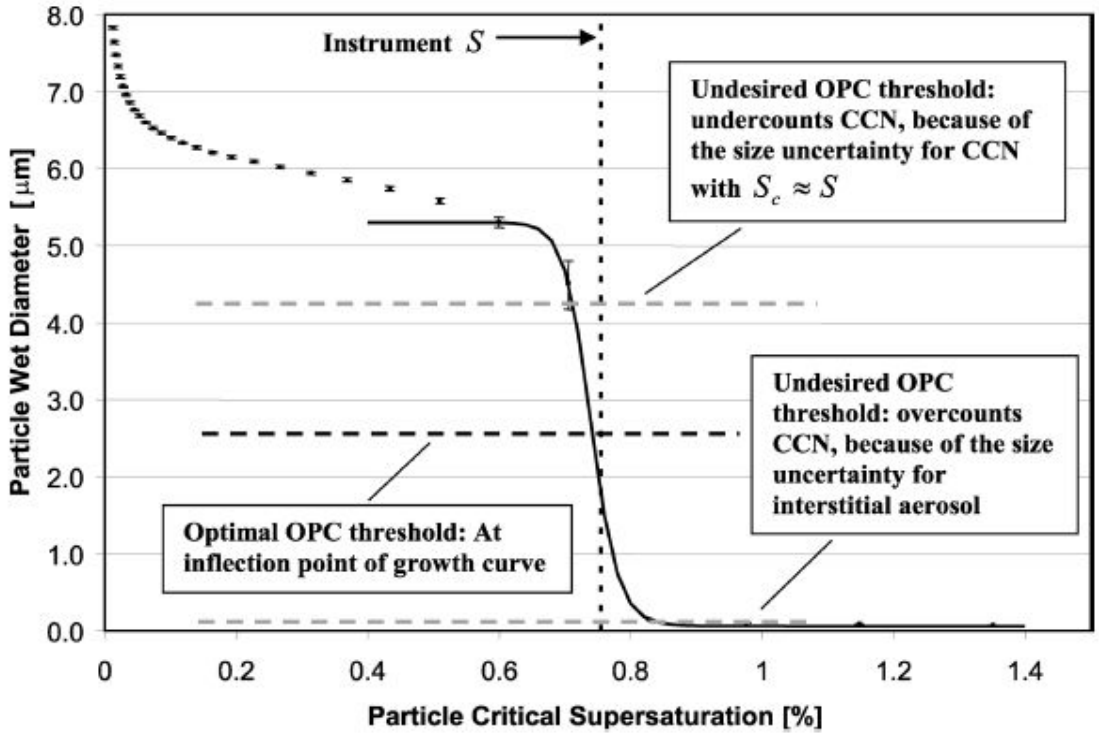


Figure 2.6. Example model growth curve (wet particle diameter versus particle critical supersaturation), showing the criteria for an acceptable OPC detection threshold. Error bars show the uncertainty in particle size due to non-uniform supersaturation and residence times. Also shown is the sigmoidal curve used to fit the model results at the inflection point.

To determine the inflection point of the growth curves, the droplet growth simulations are fit to a sigmoidal function,

$$D_p\Big|_{out} = \frac{B - A}{1 + (S_c / D)^C} + A \tag{2.17}$$

where A and B are the two asymptotes of the sigmoid, C and D are the other sigmoidal parameters, S_c is the particle critical supersaturation and $D_p\Big|_{out}$ is the outlet wet particle size. At the inflection point, $D_p\Big|_{out}$ becomes the average of the sigmoidal upper and lower limits, $\beta = (A + B)/2$.

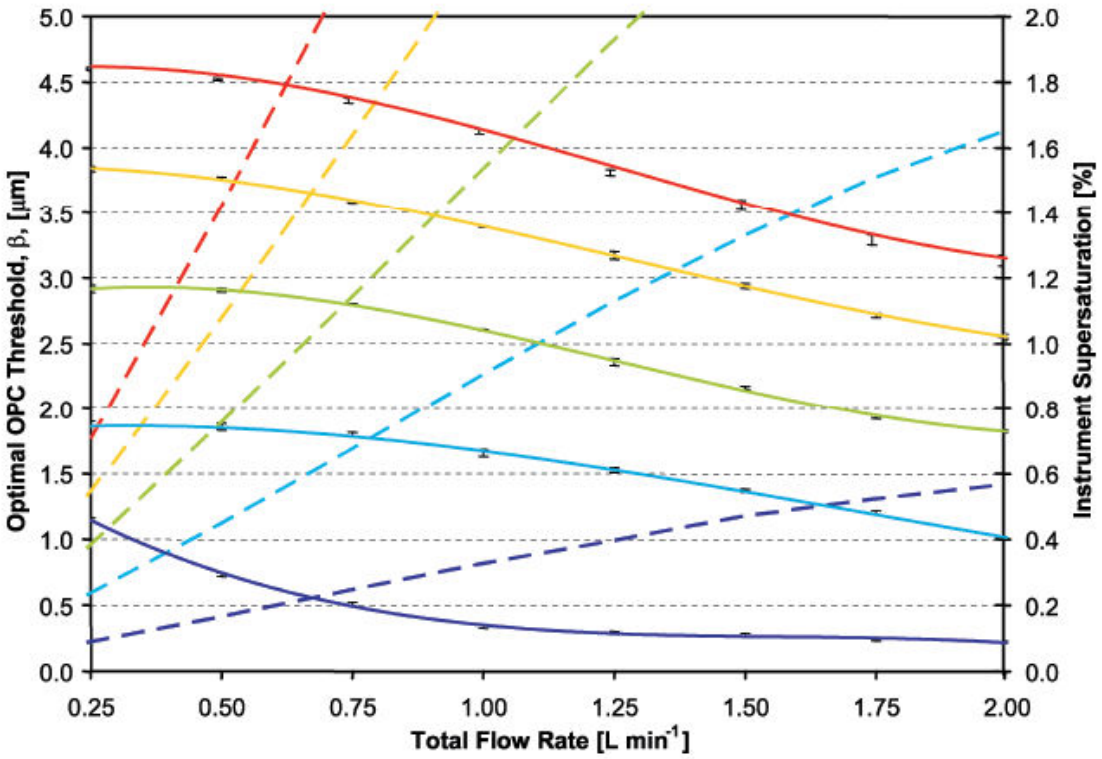


Figure 2.7. Instrument supersaturation (dotted lines) and optimal OPC detection threshold (solid lines) versus flow rate, for five different values of ΔT_{inner} (represented by color). Error bars represent the range in outlet droplet size for the same dry particle diameter (with S_c equal to the instrument supersaturation) exposed to the supersaturations and residence times of different streamlines.

Figure 2.7 displays β (solid) for a wide range of operating conditions (the error bars indicate the effect of variable supersaturation and residence time). The instrument supersaturation (dotted) is also plotted on the right axis, for the same operating conditions.

To illustrate the relationship between the outlet droplet size and the instrument operating conditions we present a simplified diffusional growth equation for activated droplets. Neglecting curvature and solute effects, the growth rate can be expressed as [*Roberts and Nenes*, 2005],

$$\frac{dD_p}{dt} = \frac{GS}{D_p} \tag{2.18}$$

where $G \approx$ const. Assuming that the CCN are in equilibrium with the instrument supersaturation (S) upon activation, integrating Equation 2.19 from the point of activation until the droplets reach the OPC gives,

$$D_p\Big|_{out} = \sqrt{D_c^2 + 2GS\tau} \tag{2.19}$$

where D_c is the CCN critical diameter and τ is the length of time that the droplets are exposed to S. The instrument supersaturation increases with ΔT_{inner}, and thus droplet growth increases (due to a greater driving force for condensation). However, droplet growth decreases as Q increases (even though S is proportional to Q) because the time

available for growth is shorter. At the lowest ΔT_{inner}, the optimal OPC detection threshold begins to increase, since D_c becomes larger as S decreases, for particles with $S_c \sim S$ [*Seinfeld and Pandis*, 1998].

$$D_c = \left(\frac{8 M_w \sigma}{3 R T \rho_w} \right) \frac{1}{S_c} \tag{2.20}$$

where σ is the surface tension of the CCN droplet at the point of activation and M_w, ρ_w are the molecular weight and density of liquid water, respectively. Thus, the outlet droplet size for particles with $S_c = S$ (the minimum droplet size) can be approximated from the instrument supersaturation, mean temperature and the time available for droplet growth following activation.

In order to determine τ, we first estimate the time it takes for the supersaturation to develop. We use empirical equations for the hydraulic (x_H), molecular (x_M) and thermal entrance lengths (x_T) [*Kreith and Bohn*, 1997] to estimate the "supersaturation entrance length" (x_S),

$$x_H = 0.05 \, \mathrm{Re}_D \, D \tag{2.21}$$

$$x_M = 0.05 \, \mathrm{Re}_D \, ScD \tag{2.22}$$

$$x_T = 0.05 \, \mathrm{Re}_D \, \mathrm{Pr} \, D \tag{2.23}$$

where D is the inner diameter of the CCN column and Re_D, Pr and Sc are the dimensionless Reynolds, Prandtl and Schmidt numbers, respectively. As $Sc < \mathrm{Pr} < 1$, the hydraulic entrance length is greater than the thermal or molecular entrance lengths, which means that the velocity profile develops relatively slowly. Thus the development of supersaturation is limited foremost by the development of the laminar velocity profile. However, since the supersaturation profile is affected by the upstream conditions, there is an additional length of time after the velocity profile has developed during which the supersaturation is still developing. This secondary limitation is a byproduct of the way in which supersaturation is generated. The transfer of heat and water vapor from the walls to the centerline of the column takes a finite amount of time (τ_T and τ_M, respectively) during which the flow continues to pass through the CCN column. As a result, the supersaturation at a given point in the column is controlled by the conditions a certain distance upstream. Since heat transfer is slower than the molecular transport of water vapor ($\tau_T > \tau_M$), after the velocity profile has developed the limiting factor for the development of supersaturation is the timescale for thermal diffusion. Thus, the supersaturation entrance length can be approximated by,

$$x_S \sim x_H + \tau_T U \tag{2.23}$$

where $\tau_T = D^2 / 4\alpha_T$, U is the average bulk velocity ($4Q/\pi D^2$) and α_T is thermal diffusivity. Assuming that droplets with $S_c = S$ are in equilibrium with the surrounding water vapor at the point of activation, the time available for droplet growth in the CCN column is therefore,

$$\tau = \frac{(L - x_s)}{U} \tag{2.24}$$

where L is the column length. It should be noted that τ is actually the minimum amount of time available for droplet growth, since all particles with $S_c < S$ can activate before the instrument supersaturation has developed.

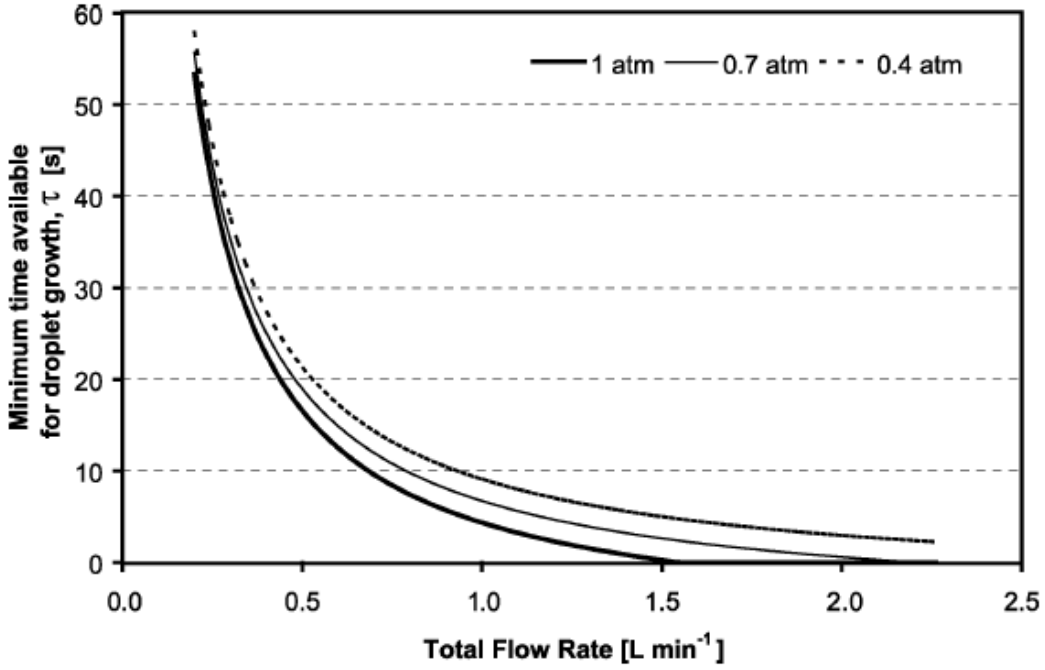


Figure 2.8. Minimum time available for droplet growth in the CCN column vs. total flow rate, for three different pressures.

Figure 2.8 shows τ as a function of flow rate for three different pressures at a mean temperature of 293K. The typical range in temperature expected for the instrument has a much smaller effect on τ than flow rate or pressure. When τ goes to zero, this

means that the supersaturation has not developed before the exit of the CCN column. For these conditions, the instrument supersaturation reported in Figure 2.7 is simply the supersaturation at the exit of the column.

Using the scaling analysis in Equations 2.19-2.24, we parameterize the optimal OPC threshold according to the following functional form.

$$\beta = (\sqrt{C_1/(TS)^2 + C_2 S(C_3 - x_s)/Q} - C_4)/C_5 \tag{2.25}$$

where C_1=1000 μm^2/K^2, C_2=7.6 μm^2 min L^{-1} m^{-1}, C_3=1.14 m, C_4=0.9 μm and C_5=0.81 results in a standard error with respect to the droplet growth simulations of 0.2 μm, which is lower than the OPC bin resolution of 0.5 μm. The coefficients C_3, C_4 and C_5 are added to the parameterization to correct for the simplifying assumptions that are made in the scaling analysis (e.g. that G is constant). As with the thermal efficiency and supersaturation parameterizations, Equation 2.25 is provided simply as a convenience to the user. The parameterization of β applies for pressures of 0.4-1.0 atm, ΔT_{inner} of 2-15 K, total flow rate of 0.25-2.0 L min^{-1} and α_c of 0.042. Smaller values for α_c will lower the droplet growth rate and β, as described previously.

Resolution Ratio

The measurement of CCN concentration in the OPC must not depend on the droplet growth kinetics; this requires that all activated CCN with S_c smaller than the instrument supersaturation become distinctly larger than unactivated aerosol. In order to

quantify our ability to distinguish between droplets and interstitial particles, we use a normalized "resolution ratio" as defined below [*Nenes et al*, 2001],

$$\frac{R_{S_c}}{R_{D_p}} = \frac{S_c}{D_p}\frac{\Delta D_p}{\Delta S_c}\bigg|_S \tag{2.26}$$

where R_{S_c} is the normalized resolution of critical supersaturation, R_{Dp} is the normalized resolution of droplet diameter, and $\Delta D_p / \Delta S_c$ is the slope of the growth curve. We evaluate R_{S_c} / R_{D_p} for the CCN experiencing the least amount of growth, i.e., for those particles with $S_c = S$. A larger value for the resolution ratio means that there is a larger range in outlet particle diameter at S, making it is easier to distinguish between activated and unactivated aerosol. For example, a resolution ratio of 20 means that a 0.5% range in S_c corresponds to a 10% range in outlet particle diameter. We estimate that a resolution ratio greater than 5 is needed to unambiguously distinguish between interstitial aerosol and droplets. Figure 2.9 shows the resolution ratio as a function of ΔT_{inner}, averaging over all flow rates. R_{S_c} / R_{D_p} is negative, indicating the inverse relationship between particle diameter and particle critical supersaturation. The magnitude of the resolution ratio increases with ΔT_{inner}, becoming greater than 15 for ΔT_{inner} above 5 K. At ΔT_{inner} less than 5 K, R_{S_c} / R_{Dp} drops below 5, indicating that the growth curve is without a discernable inflection point.

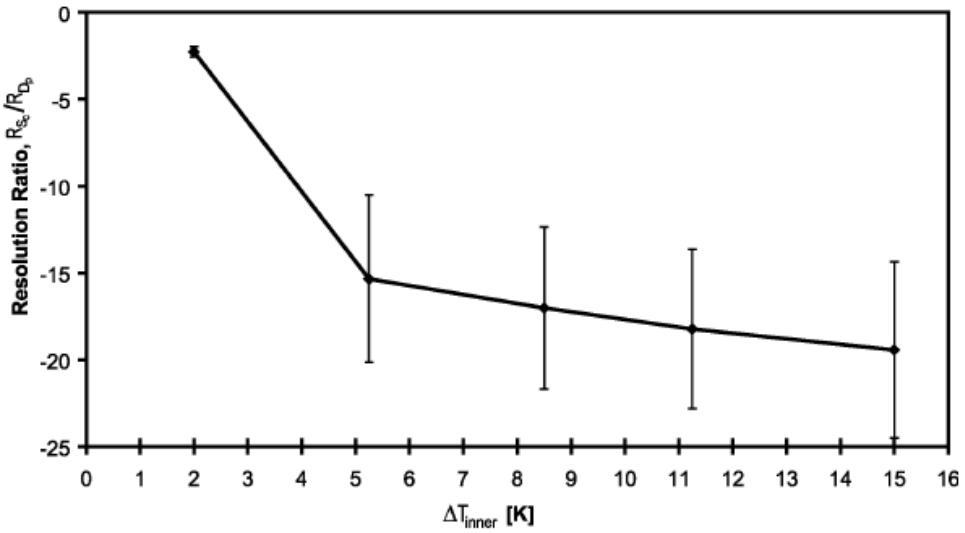


Figure 2.9. Resolution Ratio vs. ΔT_{inner} at 1 atm pressure.

Although the DMT CFSTGC can generate supersaturations below 0.1%, the resolution ratio can become very small for particles with $S_c < 0.1\%$. Particles with low S_c have a large unactivated equilibrium size that can be of the same order as droplets (~1 μm), resulting in a continuous growth curve without any abrupt indication of particle activation, which makes it difficult to estimate the appropriate droplet cutoff size. Slowly growing CCN can also result in a low resolution ratio. Below, we propose a technique for determining β for situations when the resolution ratio is small.

CCN with Slow Growth Kinetics

Decreasing the condensation coefficient to 0.005 does not change the particle equilibrium vapor pressure, but it reduces the droplet growth rate. All else being equal, a lower α_c means that the particles do not grow as much by the time they reach the outlet

of the flow chamber. At low supersaturations, CCN with low α_c may not grow to the minimum OPC detection threshold of 0.75 μm. Figure 2.10 summarizes the optimal OPC detection threshold for particles with α_c of 0.005 at 1 atm pressure. It is important to note that when β is lower than 0.75 μm, CCN are undercounted. Since the instrument supersaturation does not depend on the droplet growth kinetics (for CCN concentrations of atmospheric relevance), S remains the same as the simulations using a α_c of 0.042.

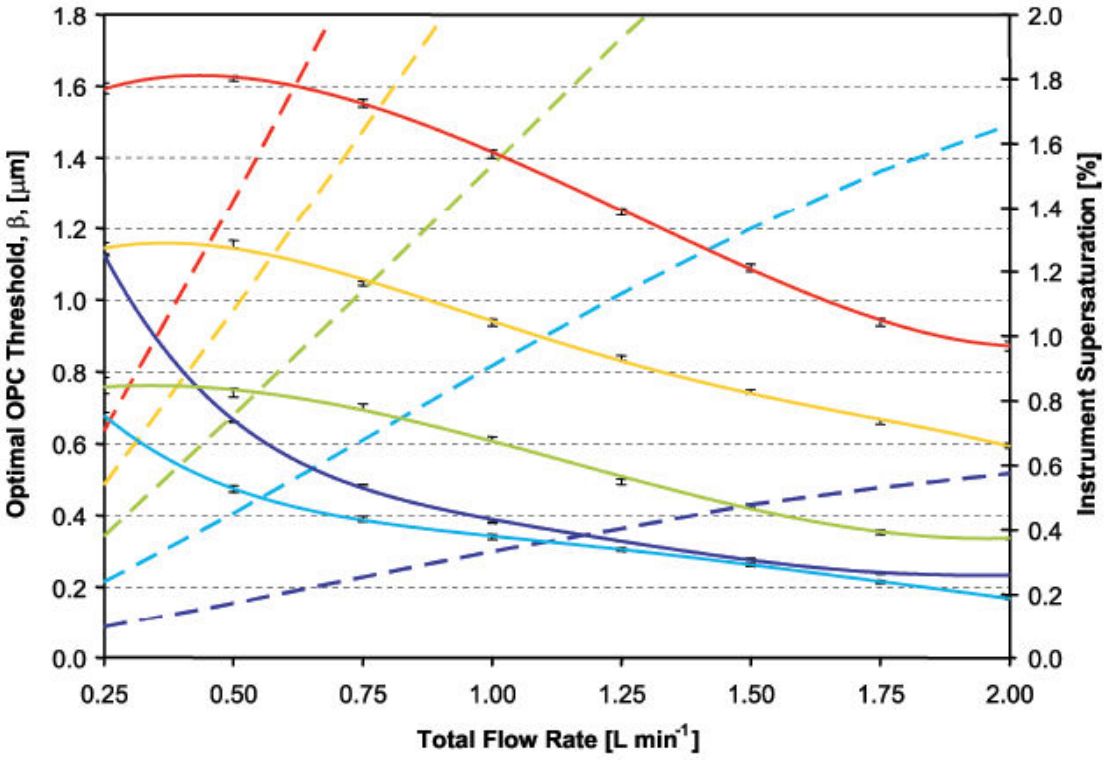


Figure 2.10. Instrument supersaturation (dotted lines) and optimal OPC detection threshold (solid lines) versus flow rate for slow-growing particles (with α_c equal to 0.005). Colors represent different values of ΔT_{inner}. Error bars represent the range in outlet droplet size for the same dry particle diameter (with S_c equal to the instrument supersaturation) exposed to the supersaturations and residence times of different streamlines.

Again, we use Equation 2.19 to understand the relationship between β and the operating conditions. As with the simulations using a 0.042 α_c, β increases with temperature, as S (and thus droplet growth) increases. Although supersaturation also increases with flow rate, β decreases with increasing flow rate, as the time available for droplet growth becomes shorter. At low supersaturations, D_c for CCN with $S_c = S$ increases. Although these CCN may be large enough for detection, the droplet number may be difficult to ascertain, as the equilibrium size of the unactivated particles becomes close to the size of droplets.

Distinguishing Slow Growing and Low S_c Particles from Droplets

A proposed technique for distinguishing droplets from unactivated aerosol is to increase the residence time of the particles within the CCN column, while maintaining the same supersaturation. Figure 2.11 shows how doubling the residence time allows kinetically limited CCN to grow and differentiate from particles that are in equilibrium with the instrument supersaturation and do not activate.

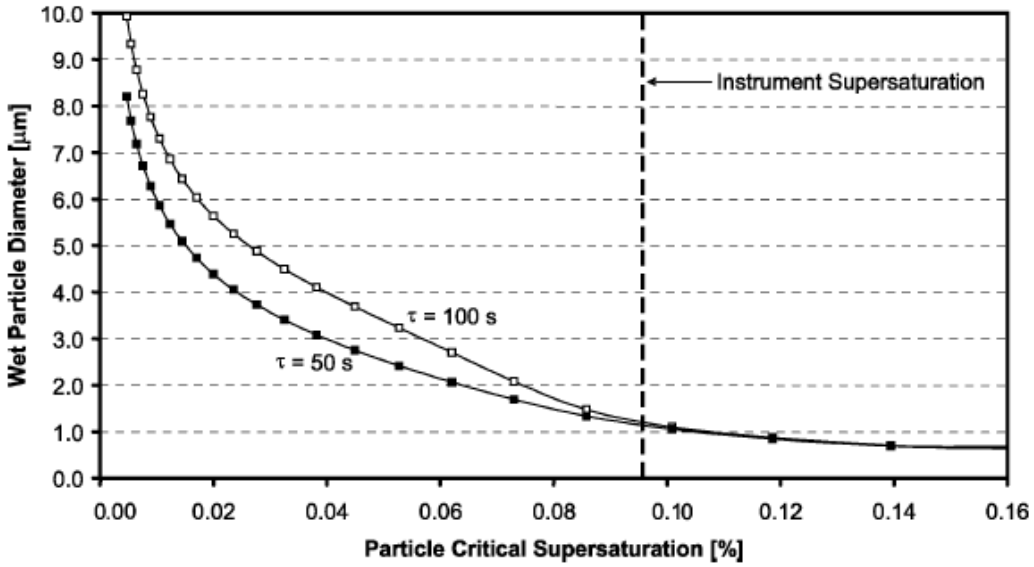


Figure 2.11. Modeled droplet growth curves at low instrument supersaturation (< 0.1%), with 50 s and 100 s residence times.

The point of divergence corresponds to the instrument supersaturation. Thus, it is not necessary to observe completely separate size modes (droplet and interstitial), in order to distinguish between activated and unactivated particles. Decreasing the total flow rate will increase the residence time, while the supersaturation can be held constant by simultaneously decreasing ΔT_{inner}. This technique still needs further exploration, but can potentially extend the practical operating range of the CFSTGC to supersaturations significantly below 0.1%, and may also be used for observing CCN with slower growth kinetics.

Summary

We have mapped the operation of the DMT Continuous Flow CCN Counter. First, the instrument is calibrated experimentally using atomized inorganic salt aerosol,

and the instrument supersaturation is inferred from the resulting activation curves. Then we use the instrument model to determine ΔT_{inner} from the calibrated supersaturation. Combining the model simulations and a simple heat transfer model, we determine that the thermal resistance of our CCN column is 3.4 ± 0.5 K W^{-1}. We also provide a multivariate regression of the calculated thermal efficiency and instrument supersaturation, to be used as a proxy for the instrument model.

Using the calibrated thermal resistance, we estimate that the thermal efficiency ranges from 50% to 85% for the range of modeled operating conditions, corresponding to a maximum temperature drop through the walls of the CCN column between 0.25 K and 7.0 K. Although pressure has a significant effect on the instrument supersaturation, it has little effect on thermal efficiency. Without taking into account the thermal efficiency, the instrument supersaturation is overestimated by up to 3% (absolute difference). We also simulate thermal efficiency for other values of thermal resistance, and provide a recommended procedure for determining thermal efficiency for specific DMT CCN units.

A droplet growth model is used to determine the optimal OPC detection threshold, which is recommended to avoid counting biases. Using an OPC detection threshold that is within the size uncertainty of the droplets may lead to underestimation of droplet counts. For most of the particles, the optimal OPC detection threshold is above 1 μm. However, for slow growing particles (e.g. with small condensation coefficients) or for particles with very low critical supersaturations, the outlet droplet size may be smaller than the minimum OPC detection threshold.

The ability to distinguish between droplets and interstitial aerosol is quantified with a dimensionless resolution ratio; a higher resolution ratio means that droplets and

interstitial aerosol are more easily distinguished. For particles with very low critical supersaturations or for slow growing particles, the resolution ratio becomes small. A technique is described for distinguishing between interstitial aerosol and droplets when the resolution ratio is small. Exploration of the instrument response for conditions or modes of operation not considered in this study, such as when used in Scanning Mobility CCN Analysis (*Nenes and Medina*, 2007) (i.e., in conjunction with a Differential Mobility Analyzer within scanning voltage mode) may further characterize the DMT CCN counter. However, this study provides the reader with a comprehensive set of tools and procedures to exploit most of the potential of this powerful instrument.

CHAPTER 3

INFERRING THE AEROSOL MIXING-STATE FROM MEASURED AMBIENT CLOUD ACTIVATION SPECTRA DURING THE MILAGRO CAMPAIGN

Introduction

The greater Mexico City area is home to nearly 20 million people, making it one of the largest metropolitan areas in the world. The city is situated on a dry lake bed at an altitude of ~7400 feet and is surrounded by mountains, resulting in a unique environment whereby the gas and particulate emissions are often trapped in a high-altitude subtropical valley, undergoing rapid photochemical oxidation and mixing with fresh emissions to produce a complex soup of dense pollution. One of the more interesting questions is how this pollution evolves and affects the regional environment as it flows out of the Mexico City basin. This is the major question addressed using the extensive dataset obtained from a month-long investigation of air quality within and downwind of Mexico City during March, 2006 called Megacities Impacts on Regional and Global Environments (MIRAGE).

MIRAGE, a part of a larger international study MILAGRO (Megacity Initiative: Local and Global Research Observations), encompassed measurements from several aircraft and ground-based sites [*Fast et al*, 2007]. Our measurements focused on the water uptake ability of ambient aerosol downwind of Mexico City at the University of

Tecámac ground site, known as 'T1'. These measurements provide a wealth of information about the chemical composition of the particles, from which we can infer the aerosol mixing-state and the thermodynamic properties of the aerosol. These properties are essential for understanding the impact of aerosols on climate (whether through the "direct," "indirect" or "semidirect" effects), and also give clues to the chemical composition and aging of the aerosol. Information obtained about the aerosol mixing-state includes the quantity of soluble material internally mixed (the solute volume fraction) and also the fraction of particles that are externally mixed (with a significantly different composition, resulting in markedly different hygroscopic behavior).

Our measurements, obtained at the peak of the "dry season," spanned from March 16th-April 1st. During this time we were intermittently impacted by strong dust events, heavy rains, local biomass burning, vehicular emissions from a nearby roadway, extremely high ammonium concentrations and the Mexico City plume. We were also intermittently impacted by emissions from the nearby Tula power plant (~40 km away), correlating with winds from the northwest and high SO_2 concentrations.

Experimental Method

We continuously sampled ambient air through ~2 ft of 1/4" copper tubing, which was thermally insulated and covered in reflective foil to prevent heating of the sample, and which protruded out the side and ~1 ft above the roof of a portable laboratory. The entrance to the sample inlet curved downwards to prevent the influx of large particles and droplets settling from above. An inline impactor located inside the laboratory removed particles greater than 1 μm, and was cleaned twice each day due to the heavy dust load.

The sampled sub-micron aerosol was electrostatically classified with a differential mobility analyzer (nanoDMA, *TSI 3085*) [*Chen et al*, 1998] using a new ^{210}Po radioactive source. Downstream of the nanoDMA, the flow was split between a Droplet Measurement Technologies (DMT) Cloud Condensation Nuclei counter (CCNc) [*Roberts and Nenes*, 2005; *Lance et al*, 2006] and a Condensation Particle Counter (CPC, *TSI 3760*). These measurements give us the "activated fraction," or the fraction of particles that grow into cloud droplets for a given water vapor supersaturation and a given dry particle size. The nanoDMA was operated with a sheath flow of 6 L min^{-1}, while the CCNc and CPC pulled 0.75 and 1.5 L min^{-1}, respectively, resulting in a DMA sheath-to-aerosol flow ratio (SAR) of ~2.7. The particle concentration measured for a 100 nm slice of the particle size distribution with this SAR typically ranged from 100 to 1000 cm^{-3} during the study, indicating that the airmass was highly polluted. Classifying the particles upstream of the CCNc allowed us to measure CCN concentrations without depleting the CCNc supersaturation.

The CCNc was calibrated several times throughout the study, exposing classified NaCl aerosol of varying particle sizes to a constant supersaturation to monitor the thermal resistance of the instrument, as described in Chapter 2. The thermal resistance increased from 4 to 4.3 K W^{-1} during the two weeks of the study, likely due to the build-up of minerals in the column walls from using drinking water instead of distilled water, the latter of which was not easily available. The CCNc was operated at 0.75 L min^{-1}, which results in a residence time of ~17 seconds in the column of the instrument. For droplets with a condensation coefficient of 0.042 or larger, this amount of time is adequate for the particles to be detected as activated droplet in the CCNc, growing to a size greater than

0.75 μm for supersaturations greater than ~0.2% [*Lance et al*, 2006]. However, at the very lowest supersaturations, we may be undercounting CCN if the ambient particles have a coating which inhibits the uptake of water, as they may not grow large enough to be detected.

A Humidified Tandem Differential Mobility Analyzer (HTDMA) [*Rader and McMurry*, 1986] was built to measure the hygroscopicity of aerosols, the stable (equilibrium) uptake of water by particles exposed to a Relative Humidity (RH) less than 100%. From a polydisperse aerosol size distribution, the instrument allows a given particle size, d_o, to pass through the first DMA (Figure 3.1). Then the aerosol is exposed to a controlled RH in a central humidifier. The particles grow to an equilibrium size that is based on their dry particle size and soluble mass. The second DMA is operated in stepping mode to obtain the size distribution after humidification, where d is the particle diameter at the peak of the distribution. The results are then described in terms of the growth factor, $g(RH) = d / d_o$. We used laboratory generated NaCl aerosol to calibrate the HTDMA several times throughout the study, using the hygroscopic growth code based on the program ISORROPIA [*Nenes et al*, 1998] to account for non-ideal solution thermodynamics.

The HTDMA was maintained at a controlled temperature of 30^{o} C using a recirculating air bath and blanket heaters. The inlet and central humidity were controlled via multi-tube Nafion humidifiers, which have semi-permeable membranes that allow water vapor to be transferred from a counter-flow purge stream. A "moist gas" and a "dry gas" (illustrated as dashed lines in Figure 3.1) are combined, using PID control loops in the labview software to control the humidity of the sample flow at the exit of

each of these humidifiers. The "moist gas" is obtained by bubbling the compressed gas (generally N_2) through a liquid water impinger. The temperatures of the impingers are controlled independently to overcome cooling from evaporation. Humidity is monitored at eight locations within the HTDMA (at the inlet and outlet of both the sample and sheath flows in both DMAs) with Vaisala humidity probes, which have a stated accuracy of ±2% RH at RH < 90%. Figure 3.2 shows the sampling setup of the CCNc and HTDMA in parallel to each other.

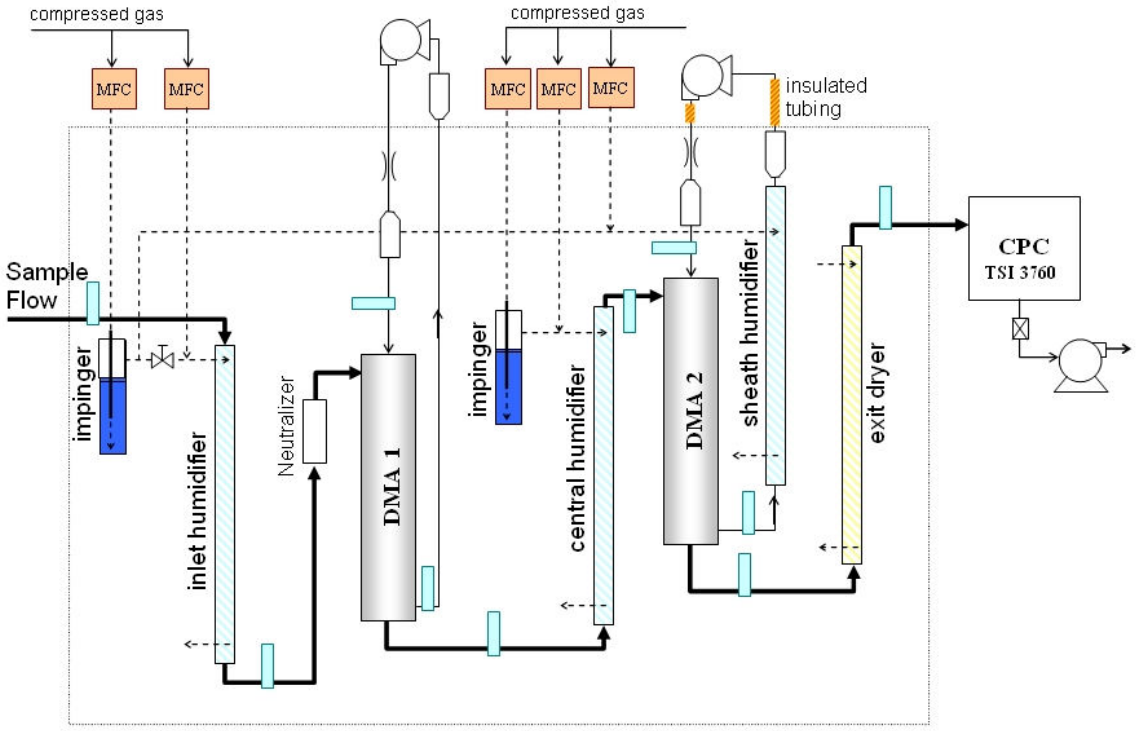


Figure 3.1. Schematic of the HTDMA.

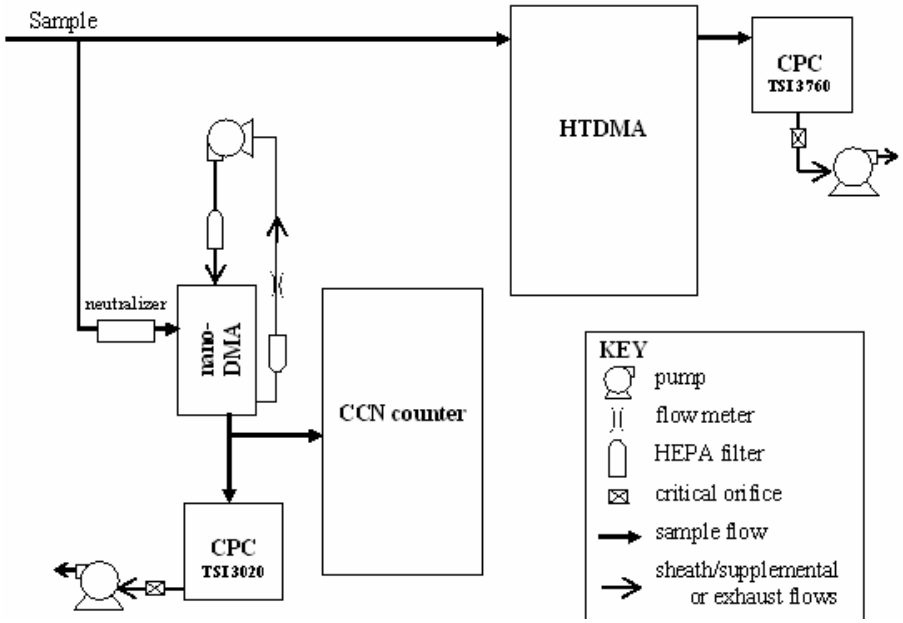


Figure 3.2. Parallel Sampling Setup of the HTDMA and CCNc

We show the operation schedule of the two instruments in Figure 3.3. The HTDMA was set at a constant supersaturation of 88% throughout the study, with the first DMA classifying a different particle size (20, 40, 60, 80 and 100 nm) every 6 minutes. Meanwhile, every 3 minutes the nanoDMA upstream of the CCNc stepped through the same five particle sizes, and the CCNc supersaturation was increased by ~0.09%. We exclude the 20 nm CCNc data from our analysis, to allow the instrument supersaturation to reach steady state (in addition to the fact that the 20 nm particles do not typically activate below 1% supersaturation); the shaded regions in Figure 3.3 show the data that is excluded for these reasons. Given 36 seconds for the supersaturation to stabilize (with an additional 20 seconds after each change in the particle size setpoint), each activated fraction measurement is an average over 16 seconds of observed CCN and particle number concentrations. An additional 3 minutes was given for the supersaturation to stabilize when starting the 30 minute cycle over again, to overcome the thermal inertia of

the CCNc. This means that nearly 4 minutes of measurements are excluded from our analysis after the supersaturation was changed from the highest to the lowest setting.

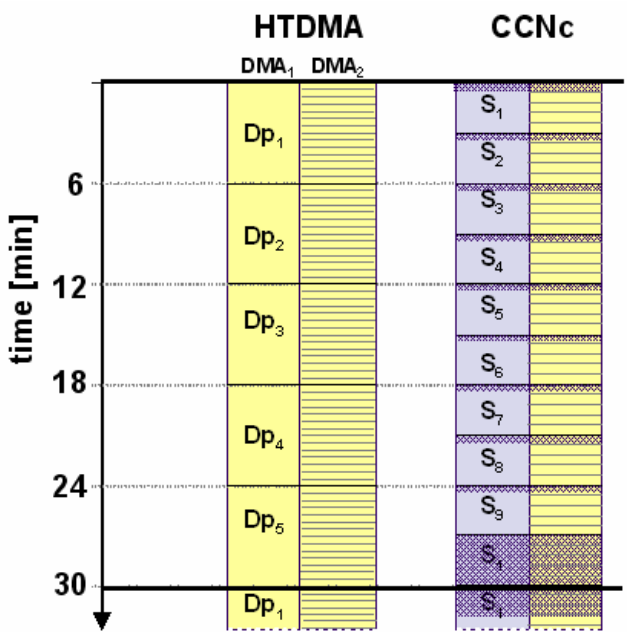


Figure 3.3. Operation Schedule of the HTDMA and CCNc throughout the study.

Data acquisition software was written for both instruments to allow coordinated measurements and to continuously and autonomously control and record the HTDMA, nanoDMA and CCNc measurements during the study.

Analysis Method

Every 30 minutes we obtained an "activation spectra," the activated fraction as a function of supersaturation, for four particle sizes. See Figure 3.4 for an example of an observed activation spectrum (open diamonds) for a nominal 100 nm ambient aerosol at ~21:00 UTC on March 27, 2006. The vertical error bars denote one standard deviation in

the activated fraction, the ratio of CCN to total particle (or condensation nuclei, CN) number concentrations during the 16 second interval when each measurement was taken. A single point on the activation spectrum indicates the fraction of particles with a critical supersaturation (S_c) less than or equal to the instrument supersaturation (S), and each point on the activation spectrum was taken within 3 minutes of the adjacent point.

Sigmoidal Fit of CCN Activation Spectra

We fit the activation spectrum to a sigmoidal function of the following form:

$$\frac{CCN}{CN} = \left(\frac{E^*}{1 + \left(S/S^*\right)^C} \right) \tag{3.1}$$

where *CCN/CN* is the fraction of particles that activate at *S*, E^* is the upper asymptote of the sigmoid, S^* is the location of the inflection point and *C* is proportional to the slope (negative since the activated fraction increases with supersaturation). E^* indicates the fraction of externally-mixed, unactivated particles, S^* indicates the "characteristic" critical supersaturation of the aerosol population, and C reveals the degree of chemical heterogeneity of the activated particles.

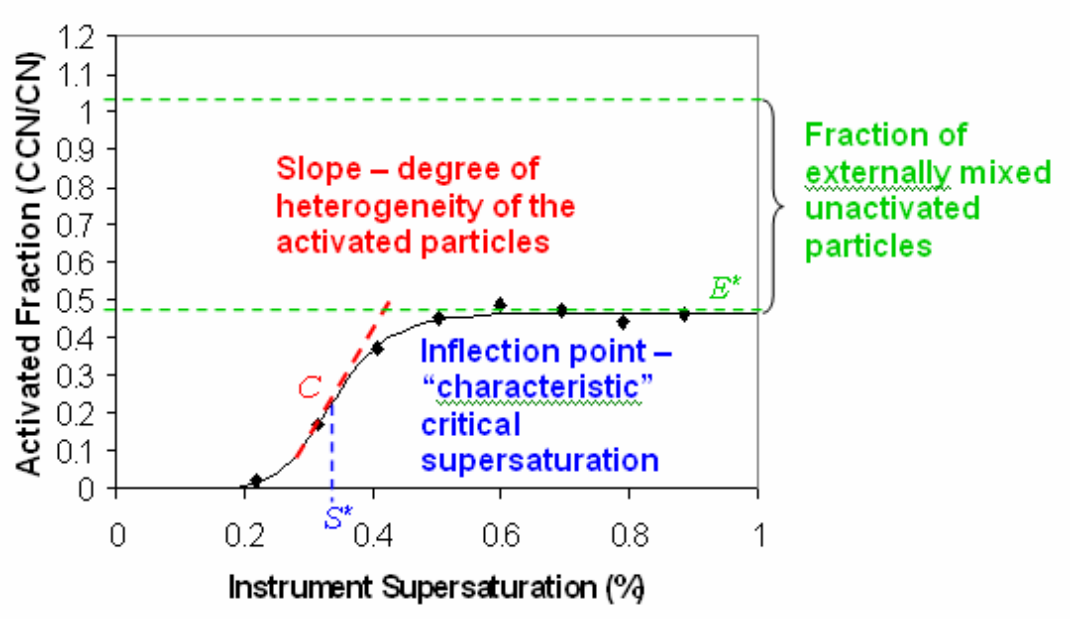


Figure 3.4. Example activation spectrum from March 16th at ~13:00 UTC with explanation of the sigmoidal fit parameters.

The normalized sigmoidal fit describes the chemical characteristics of the activated particles.

$$\left(\frac{CCN}{CN}\right)^{*} = \frac{1}{E^{*}}\left(\frac{CCN}{CN}\right) = \left(\frac{1}{1+\left(S/S^{*}\right)^{C}}\right) \tag{3.2}$$

Differentiating the activation spectrum yields the probability distribution of S_c, $p(S_c)$, or the fraction of particles with $S_c = S$. Thus, the activation spectrum is the cumulative distribution of $p(S_c)$.

$$p(S_c) = \frac{d}{dS}\left(\frac{CCN}{CN}\right) \tag{3.3}$$

If all particles in the aerosol population have $S_c = S$, this would result in a delta function for $p(S_c)$ and a step function for the activation spectrum, and would require a truly monodisperse, singly-charged, single-component aerosol population of uniform shape exposed to a single supersaturation. The observed ambient activation spectra always have lower slopes than this purely hypothetical limit, due to non-uniformity in both the aerosol chemical and physical properties, as well as non-uniformity in the streamline supersaturations of the instrument. With the 10:1 sheath-to-aerosol flow ratio used in the CCNc, the variability in instrument supersaturation for the cross-section of aerosol flow is minimal.

The chemical and particle size dispersions both contribute to the slope of the activation spectrum through their respective effects on S_c, as constrained by Köhler Theory,

$$S_c = 100\left[\exp\left(\frac{4A^3}{27B}\right)^{1/2} - 1\right] \qquad A = \frac{4M_w\sigma}{RT\rho_w}, \quad B = SVF \cdot d_p^3 \tag{3.4}$$

where M_w, σ and ρ_w are the molecular weight, surface tension and density of water, R is the universal gas constant, T is the temperature of the droplet and d_p is the particle dry diameter (assumed to be spherical). We assume that there is no surface tension depression from surface active compounds, as evidenced by surface tension experiments with extracted filter samples from the T1 site during the same time period [Padró et al, *in preparation*]. The Scaled water-soluble Volume Fraction (SVF) is a dimensionless term

that describes the internally mixed dry particle solute volume fraction scaled by characteristic properties of the solute and water. SVF can be determined for aerosols of known composition (assuming that the activity of the particular compound in water is known, which is represented in the ν term).

$$SVF = \frac{B}{d_p^3} = \frac{\varepsilon_s M_w \nu \rho_s}{\rho_w M_s} \tag{3.5}$$

where ε_s, M_s, ρ_s and ν are the solute dry volume fraction, molecular weight, density and van't Hoff factor, respectively. SVF is $1.3\,\varepsilon_s$ for NaCl, $0.6\,\varepsilon_s$ for $(NH_4)_2SO_4$ (assuming a van't Hoff factor of 2.5 [*Rose et al*, 2007]), $0.8\,\varepsilon_s$ for NH_4NO_3 and ~$0.2\,\varepsilon_s$ for low molecular weight organics (with M_{Org} = 125 amu, ν_{Org} =1, ρ_{Org} =1.4 g cm^{-3}). For a multi-component aerosol, SVF is calculated assuming volume additivity:

$$SVF = \sum_s SVF_s = \left(\frac{M_w}{\rho_w}\right)\sum_s \frac{\varepsilon_s \nu_s \rho_s}{M_s} \tag{3.6}$$

The "characteristic" SVF for the aerosol population, SVF^*, is calculated by rearranging Equation 3.4 and substituting S^* for S_c.

$$SVF^* = \frac{4A^3}{27 d_p^3}\left(\frac{1}{\ln[S^*/100+1]}\right)^2 \approx \frac{4A^3}{27 d_p^3}\left(\frac{100}{S^*}\right)^2 \tag{3.7}$$

Assuming that the aerosol population is monodisperse, we can directly calculate $p^s(SVF)$, the probability distribution of SVF, using the sigmoidal fit to the activation curve and substituting S_c (Equation 3.4) for S (in Equation 3.2).

$$\left(\frac{CCN}{CN}\right)^* = \frac{1}{1+\left(\frac{\omega \cdot SVF^{-1/2}}{S^*}\right)^C} \qquad \omega \approx 100\left[\frac{4A^3}{27d_p^3}\right]^{1/2} \tag{3.8}$$

$$p^s(SVF) = \frac{d}{dSVF}\left(\frac{CCN}{CN}\right)^* = \frac{C\left(\frac{\omega \cdot SVF^{-1/2}}{S^*}\right)^{C-1} \omega \cdot SVF^{-3/2}}{2S^*\left[1+\left(\frac{\omega \cdot SVF^{-1/2}}{S^*}\right)^C\right]^2} \tag{3.9}$$

Integrating $p^s(SVF) = dP^s / dSVF$ yields the fraction of particles with SVF between the limits of integration; this is analogous to the particle size distribution function, defined as $n(d_p) = dN / d(d_p)$, where integration yields the number concentration of particles with d_p between the limits of integration. A Taylor expansion approximation was used in Equations 3.7 and 3.8 to simplify the analytical solution. The resulting probability distribution is skewed to larger values of SVF, as shown in Figure 3.5 for March 30th at ~07:00 UTC, since the sigmoidal fit is symmetric with respect to S_c and yet there is a nonlinear relationship between SVF and S_c. Figure 3.5 shows hypothetical examples for $p^s(SVF)$, given a constant characteristic supersaturation, S^*,

and particle diameter, d_p, and given different values for C. As shown in the figure, the dispersion and skew are greater for lower values in the magnitude of C.

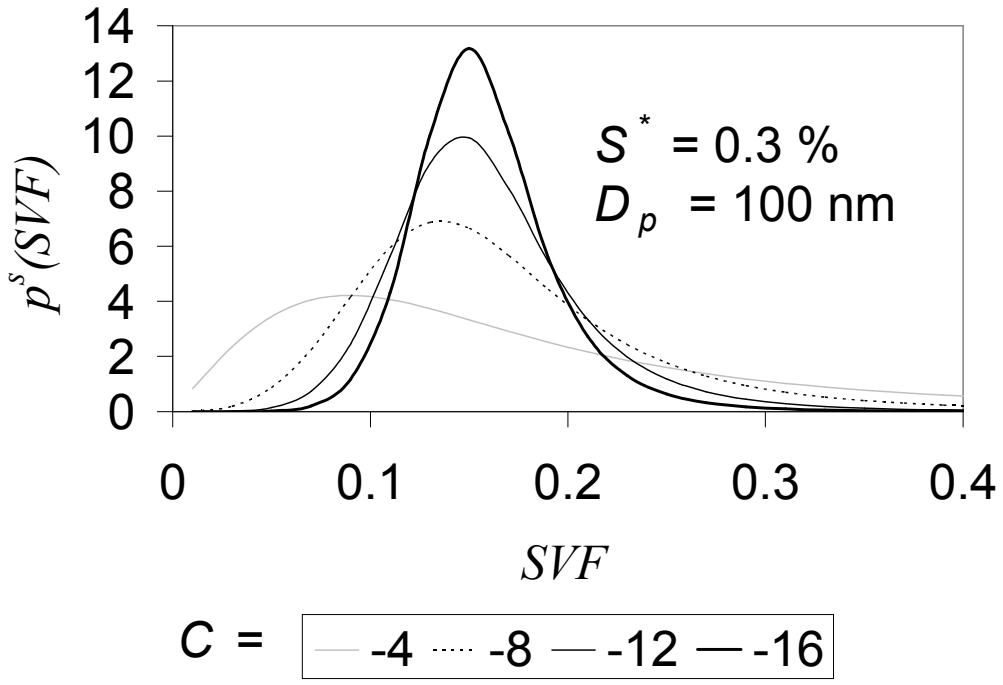


Figure 3.5. Probability distribution of scaled volume fraction (SVF) calculated using the sigmoidal fit with different C parameters.

In Figure 3.6, we show the standard deviation of the $p^s(SVF)$ distribution, calculated from Equations 3.9 and 3.10, for different values of S^* and C.

$$\sigma(SVF) = \frac{\int_0^\infty (SVF - \overline{SVF})^2 \, p^s(SVF) dSVF}{\int_0^\infty p^s(SVF) dSVF} \tag{3.10}$$

$\sigma(SVF)$ describes the chemical dispersion, or the degree of chemical heterogeneity for the CCN population. Given the same C and d_p, the chemical distribution is broader for lower values of S^*, yielding a greater $\sigma(SVF)$. Conversely, this means that for a given $\sigma(SVF)$, the slope of the activation spectrum is steeper at lower values of S^* (or for larger particle sizes).

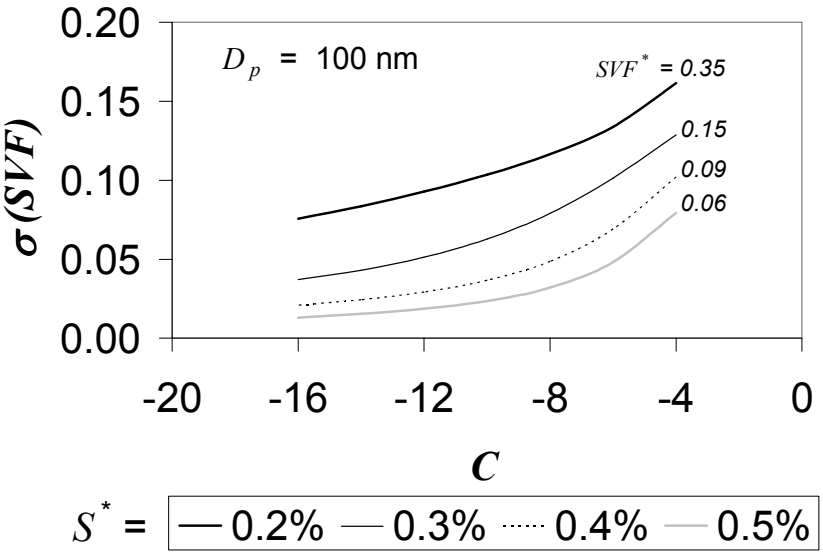


Figure 3.6. Translating the sigmoidal fit parameter (C) to a standard deviation, for different characteristic critical supersaturations (S^*).

This can be explained by differentiating Equation 3.7,

$$\frac{d(SVF^*)}{d(S^*/100)} = -\frac{8A^3}{27d_p^3}\left(\frac{100}{S^*}\right)^3 \approx \frac{\Delta SVF^*}{\Delta S^*/100} \tag{3.11}$$

where ΔSVF^* is the uncertainty of SVF^* and ΔS^* is the uncertainty in S^*. Thus, Equation 3.11 tells us how precisely we can determine SVF^* given the uncertainty in our fitted S^* parameter, and we see that this is highly dependent on both d_p and S^*. Figure 3.7 shows the ΔSVF^* for a 100 nm hypothetical aerosol, given different values of S^* and ΔS^*.

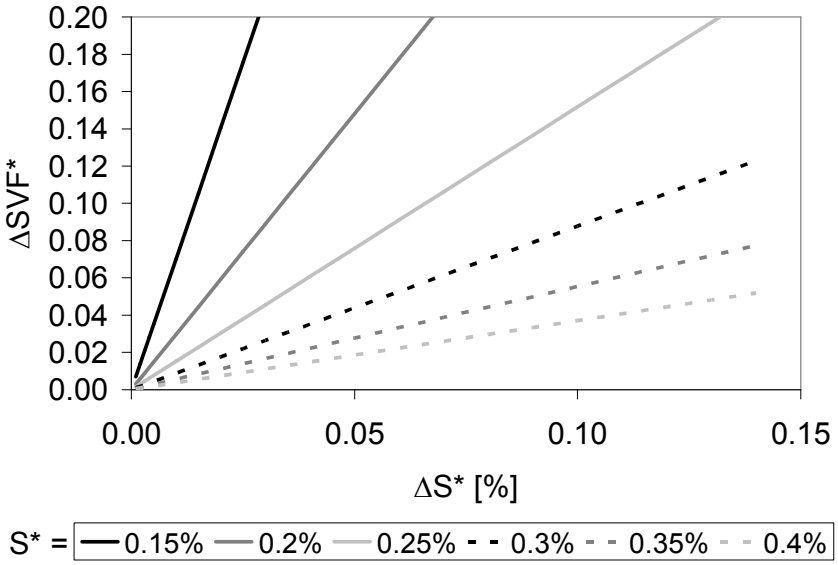


Figure 3.7. Uncertainty in SVF^* due to uncertainty in S^*

Comprehensive Analysis

To analyze the affect of the classified particle size distribution on the slope of the ambient activation spectra, we perform a "comprehensive analysis" in which the population of particles entering the CCNc are represented by two independent probability distributions, $p'(d_p)$ and $p''(SVF)$.

$p'(d_p)$ is estimated from the observed ambient dry particle size distribution ($n(d_p)$), the theoretical DMA transfer function (Ω) [*Wang and Flagan*, 1990] and the particle charging (ε_n), transmission (ε_t) and counting (ε_c) efficiencies.

$$p'(d_p) = \frac{dP'}{d(d_p)} = \frac{\sum_{i=1}^{3}\left(n(d_p)\cdot\Omega_i\cdot\varepsilon_i\cdot\varepsilon_t\cdot\varepsilon_c\right)}{\sum_{i=1}^{3}\left(\int_0^{\infty} n(d_p)\cdot\Omega_i\cdot\varepsilon_i\cdot\varepsilon_t\cdot\varepsilon_c\cdot dd_p\right)} \tag{3.12}$$

where i is the particle absolute value of charge. The transfer function, Ω_i, is first calculated for $i = 1$. We then calculate the particle diameters with equivalent electrical mobilities, but with multiple charge ($i = 2$ and $i = 3$), to determine Ω_2 and Ω_3. After correcting for charging, transmission and counting efficiencies and accounting for the ambient particle size distribution, we then sum the overlapping distributions to obtain the dry particle size distribution expected at the entrance of the CCNc instrument. The denominator of Equation 3.12 is the sum of all particles that are expected to reach the CCNc, and is independently verified by the total particle concentration recorded with the CPC parallel to the CCNc.

To illustrate how the particle size distribution independently affects the slope of the activation spectrum, we use Equation 3.4 to convert $p'(d_p)$ to a probability distribution of particle critical supersaturations ($p(S_c)$) given a constant SVF. With a homogeneous aerosol composition, each d_p corresponds to a unique S_c; this means that

all particles above a threshold dry size, d_p^*, activate for a given S. Integrating $p(S_c)$ from *0* to S gives the cumulative $p(S_c)$ distribution, or the activation spectrum.

$$\left(\frac{CCN}{CN}\right)\Bigg|_s = \int_0^S p(S_c)dS_c = \int_{d_p^*}^{\infty} p'(d_p)dd_p \tag{3.13}$$

The effect of particle size distribution on the slope of the activation spectrum has been experimentally investigated using aerosol of known, single-component chemistry. Figure 3.8 shows the activation spectra for a nominal 60 nm ammonium sulfate calibration aerosol (black diamonds), using a DMA sheath-to-aerosol ratio of 2.7. Vertical error bars show one standard deviation in the activated fraction. Horizontal error bars show one standard deviation in the instrument supersaturation (based on the instrument temperature, flow and pressure readings) plus one standard deviation in the particle critical supersaturation (based on the uncertainty in d_p and ν [*Rose et al*, 2007]). Also plotted (solid line) is the activation spectrum calculated from the particle size distribution assuming that $n(d_p)$ is constant over the width of the transfer function (since we did not measure the atomizer size distribution for this calibration experiment). We use Equation 3.5 to calculate SVF given that the dry soluble volume fraction is 1.0 and assuming a van't Hoff factor of 2.5 for ammonium sulfate [*Rose et al*, 2007]. We also assume that the particles have a spherical shape, which is realistic for atomized aqueous ammonium sulfate [*Zelenyuk et al*, 2006]. The small difference between the measured and predicted activation fractions for this calibration experiment is assumed to be caused by not accounting for the atomizer particle size distribution. Shown in Figure

3.8 for comparison is the nominal 100 nm ambient activation spectrum from March 30th, 2006 at ~09:00 UTC, using the same DMA sheath-to-aerosol-ratio as used in the calibration experiment.

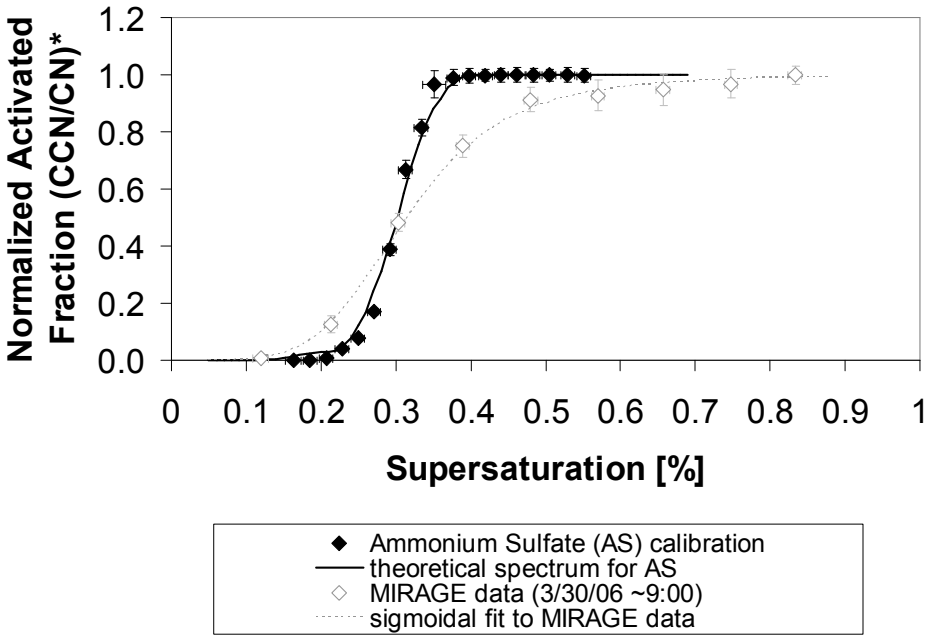


Figure 3.8. Measured activation spectra for ammonium sulfate (AS) aerosol with a nominal geometric mean diameter of 60nm (black diamonds). Also shown is the normalized ambient 100nm activation spectrum from March 30th ~09:00 UTC (open diamonds). The dotted line is the sigmoidal fit to the ambient data and the solid line is the theoretical activation spectrum for the AS calibration assuming that the atomizer size distribution is flat.

Since we are interested in the slope of the activation spectra, which is expected to decrease with increasing S_c, we chose a particle size for the calibration aerosol to yield a S_c comparable to the ambient data. We hypothesize that the lower slope of the ambient activation spectrum is mainly due to variability in particle chemical composition and, we expect to a lesser extent, due to variability in particle shape. For comparison, the

sigmoidal fit parameter *C* is -15 and -4.8 for the above ambient activation spectrum and calibration experiment, respectively. Although, for the calibration experiment, the *C* parameter cannot be used to describe the aerosol chemical heterogeneity, we know from a sigmoidal fit to the calibration data that a value of *C* greater in magnitude than 15 does not make sense for an aerosol population with $S^* \geq 0.3$ %. This limit is due to the fact that when the chemical dispersion is small enough (as is the case with our calibration aerosol), the size dispersion in the nanoDMA controls the slope of the activation spectrum.

To infer the chemical heterogeneity of the ambient CCN, we first assume that the aerosol composition can be represented by a normal probability distribution, $p''(SVF)$, that is constant for a narrow slice of the particle size distribution (across the width of the DMA transfer function).

$$p''(SVF) = \frac{dP''}{dSVF} = \frac{1}{\sigma\sqrt{2\pi}} \exp\left(-\frac{(SVF - \overline{SVF})^2}{2\sigma^2} \right) \tag{3.14}$$

where σ is the standard deviation and $\overline{SVF}$ is the mean of the distribution of SVF. We multiply $dP''(SVF)$ and $dP'(d_p)$ to calculate the joint probability $dP^*(SVF, d_p)$ of having particles with both d_p and SVF. Then we multiply by E, the fraction of particles that are CCN in the given population. A single combination of d_p and SVF constrains S_c according to Köhler Theory; however $dP^*(SVF, d_p) \neq dP(S_c)/E$ because other combinations of d_p and SVF also result in the same S_c. To determine the total

probability of all combinations of d_p and SVF that result in S_c we sum all $E \cdot dP^*(SVF, d_p)$ that result in S_c. This is done systematically by first determining SVF required to yield S_c for a given d_p, by rearranging Equation 3.4.

$$SVF = \left(\frac{4A^3}{27 d_p^3} \right) \frac{1}{[\ln(S_c/100 + 1)]^2} \tag{3.15}$$

which can be approximated as

$$SVF = \alpha \cdot d_p^{-3} S_c^{-2} \qquad \alpha = \frac{4}{27(100)^2} \left(\frac{4 M_w \sigma}{RT\rho_w} \right)^3 \tag{3.16}$$

Then $dP'(d_p)$ and $dP''(SVF)$ are calculated using Equations 3.12 and 3.14, respectively. $dP^*(SVF, d_p)$ is calculated by multiplying $dP''(SVF)$ and $dP'(d_p)$ for that particle size bin. Then the $dP^*(SVF, d_p)$ of the next size bin is calculated in the same way, and we sum all $dP^*(SVF, d_p)$ to determine $dP(S_c)/E$. The three parameters, E, σ and $\overline{SVF}$, are then solved for iteratively by minimizing the square error between the calculated and observed $p(S_c)$, which ultimately yields the $p''(SVF)$ distribution.

Another way of representing this algorithm is to substitute Equation 3.16 into Equation 3.14 to get $p''(\alpha \cdot d_p^{-3} S_c^{-2})$. Then the following relationship holds.

$$p(S_c) = \int_0^{\infty} E \cdot p'(d_p) \cdot p''(\alpha d_p^{-3} S_c^{-2}) d(d_p) \tag{3.17}$$

Equation 3.17 assumes that particle composition and mixing state is constant over the width of the classified particle size distribution, which may not be true. Figure 3.9 shows the activation spectra for 40, 60, 80 and 100nm particles on March 27th at ~21:00 UTC. During this time we see that the sigmoidal fit parameter SVF^* decreases for the larger activated particles, while the fraction of unactivated particles decreases slightly (as indicated by an increasing E^* parameter).

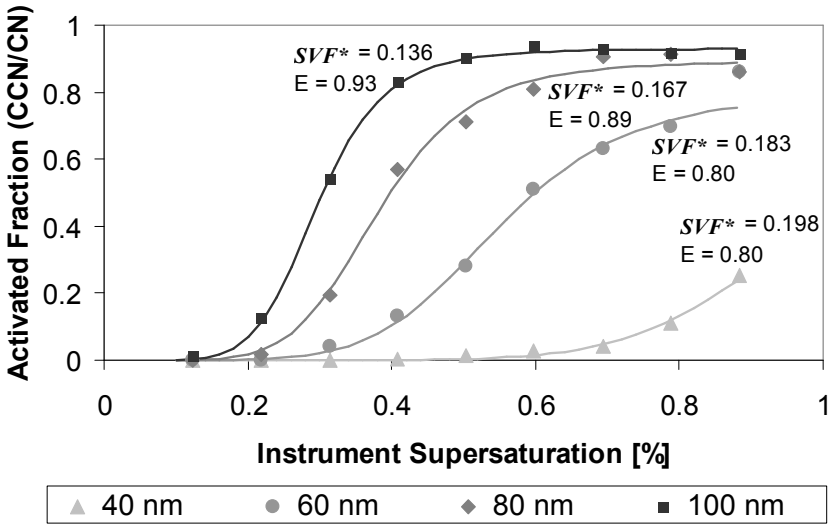


Figure 3.9. Example activation spectra as a function of particle diameter from March 27th at ~21:00 UTC, with the characteristic scaled volume fraction (SVF^*) and fraction of activated particles (E^*) shown. The larger the particles, the lower the SVF^* but the higher the E^*. This is consistent with the larger particles being more internally mixed.

Since the two normal parameters for the $p''(SVF)$ distribution vary continuously with particle size, the next step was to parameterize E, σ and $\overline{SVF}$ as functions of d_p. This may be important for understanding the CCN activity of the multiply-charged particles (since they are significantly larger than the nominal particle size, and are thus more likely to have a different composition and/or mixing state). Parameterizing the dependence of particle chemistry on size decreases the number of fit parameters from 12 (with a value for σ, $\overline{SVF}$ and E, for 4 particle sizes) to 6-10 (with a simple function for σ, $\overline{SVF}$ and E, each dependent upon d_p). The following equation shows the substitution of $\sigma(d_p)$, $E(d_p)$ and $\overline{SVF}(d_p)$ for σ, E and $\overline{SVF}$ in Equation 3.17.

$$P(S_c) = \frac{1}{\sigma\sqrt{2\pi}} \int_0^\infty E(d_p) \cdot P'(d_p) \cdot \exp\left(- \frac{(\alpha d_p^{-3} S_c^{-2} - \overline{SVF}(d_p))^2}{2\sigma(d_p)^2} \right) dd_p \qquad (3.18)$$

Solving Equation 3.18 ultimately gives the $p''(SVF)$ distribution as a continuous function of particle diameter, by iteratively fitting the cumulative $p(S_c)$ distribution to the observed activation spectrum. We use the σ, E and $\overline{SVF}$ parameters calculated by fitting each activation curve independently as initial guesses for the parameterizations of $\sigma(d_p)$, $E(d_p)$ and $\overline{SVF}(d_p)$ used in Equation 3.18. Linear, exponential, quadratic or sigmoidal functions for $\sigma(d_p)$, $\overline{SVF}(d_p)$ and $E(d_p)$ were used, whichever produced the smallest square error when comparing with these initial guesses. Figure 3.10 shows

an example of the parameterizations for $\sigma(d_p)$, $\overline{SVF}(d_p)$ and $E(d_p)$ on March 30th at ~07:00 UTC, and the resulting activation spectra calculated using Equation 3.18.

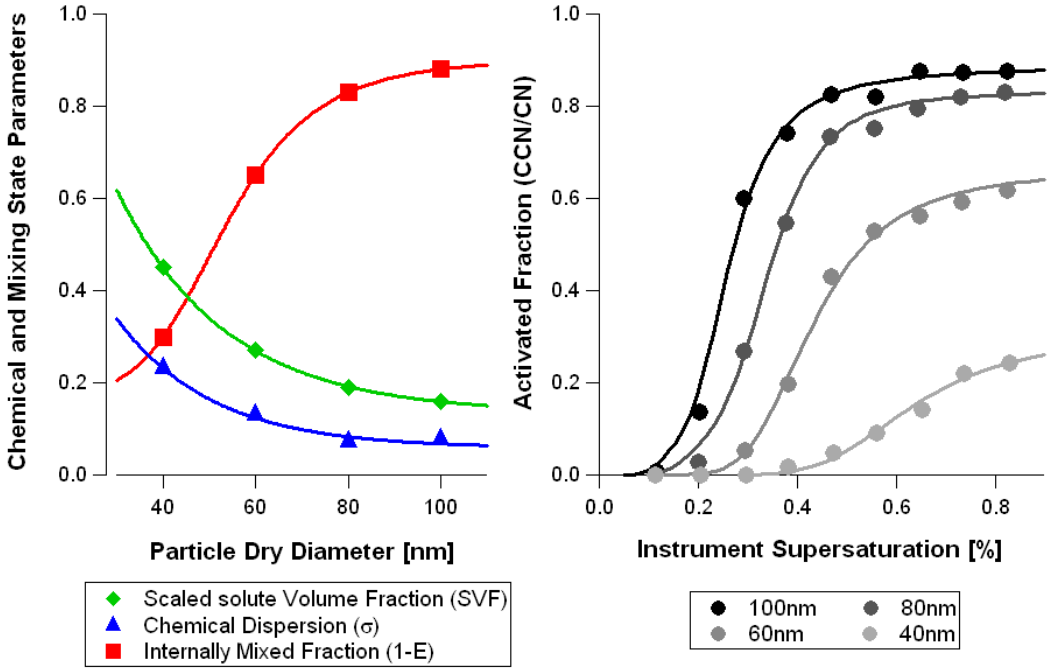


Figure 3.10. Example of the parameterizations for $\overline{SVF}(d_p)$ (green), $\sigma(d_p)$ (blue) and $E(d_p)$ (red) and the resulting fit for the activation spectra of all four dry particle sizes for March 27th at ~21:00 UTC.

The calculated activation spectra in Figure 3.10 fit the observations as well as or better than the sigmoidal fits, with 10 rather than 12 fit parameters overall, having an actual physical basis that underlies their shape. The shape of the chemical distribution as a function of dry particle size is less well understood, but we have a qualitative explanation for the general trend. Larger dry particles have a lower soluble fraction, but a larger fraction of these particles are CCN. This can be understood by the fact that, over the range of particle sizes measured, larger particles are typically more aged than smaller

particles. When small particles are formed or emitted, they may be very hygroscopic (such as freshly formed sulfuric acid particles) or very hydrophobic (such as soot). These will show up as clearly externally mixed particles in the activation spectra. However, with coagulation and with subsequent photochemical aging, the particles that grow from these "pure source aerosols" will be become more internally mixed, consistent with both a higher activated fraction and a lower soluble fraction.

Figure 3.11 compares the $p''(SVF)$ distribution calculated using the comprehensive analysis (Equation 3.12-3.18) to the $p^s(SVF)$ distribution calculated assuming a monodisperse aerosol population (Equation 3.9) for a nominal 100nm ambient aerosol on March 30th at ~07:00 UTC. The difference in the peak SVF for these two curves is less than 0.002, which yields a relative error of ~1%. However, the shapes of the curves are different, by definition.

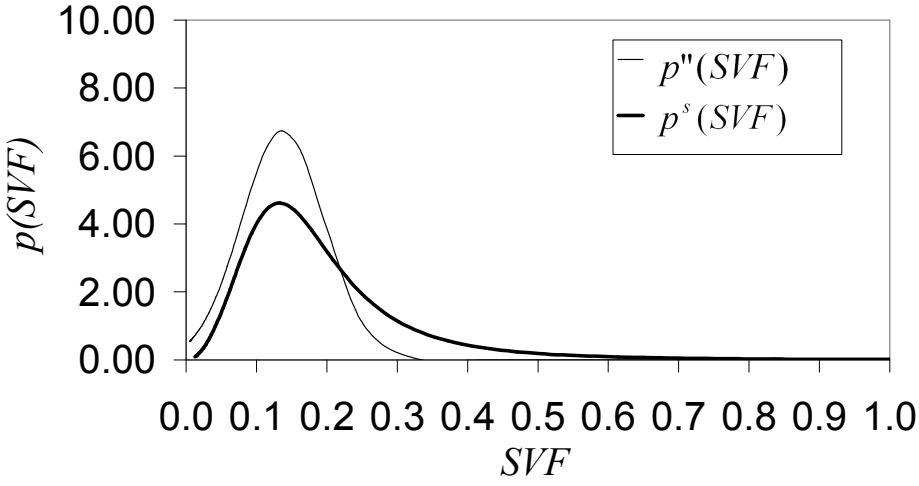


Figure 3.11. Probability distribution of the scaled volume fraction (SVF) for 100nm particles on March 30th at ~07:00 UTC, assuming first a monodisperse aerosol population (thick curve) and then using a comprehensive analysis (thin curve) which takes into account non-idealities of the nanoDMA and particle chemistry as a function of particle size.

Although we expect to have generated an equilibrium bipolar charge distribution prior to aerosol classification, we rarely observe an obvious "shoulder" in the ambient data at the lower S_c to indicate the presence of the larger multiply-charged particles. Possible reasons for the absence of a shoulder in the observed activation spectra are related to particle chemistry; the larger particles that are allowed to pass through the DMA because they are multiply-charged may have a different chemical composition, and this could eliminate or obscure the shoulder in several ways. We assume that charging efficiency is not chemistry-dependent. First, the larger activated particles may have a lower SVF^*, resulting in a S_c that is larger than expected and a shoulder that overlaps with the smaller singly-charged particles on the activation spectrum. Second, the fraction of unactivated externally-mixed particles may be higher at larger particle sizes causing the shoulder to shrink. Third, the chemical dispersion for the larger particles may be greater, causing the shoulder to blend with the dominant spectra. All of these mechanisms can be explored using the analysis method described with the given dataset.

Figure 3.12 shows the theoretical activation spectrum using the comprehensive analysis method given different assumptions for the variability in particle chemical composition (Equation 3.18), comparing to the observed activation spectrum for the 100 nm nominal particle size on March 27th at ~21:00 UTC.

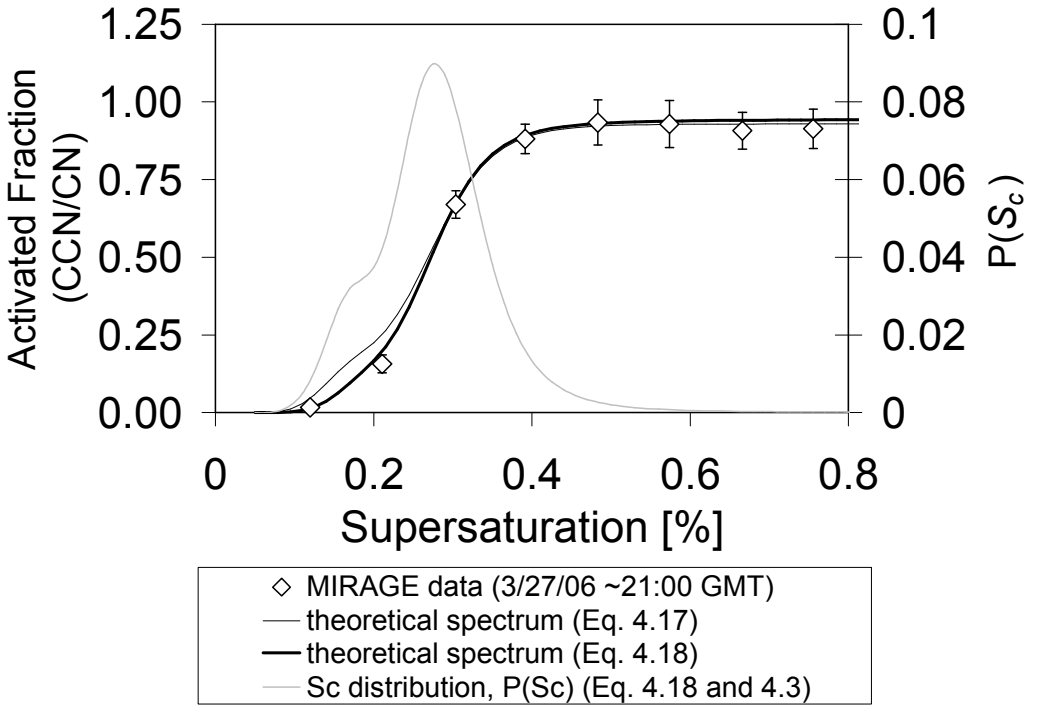


Figure 3.12. The "comprehensive analysis" fit for an example 100nm activation spectrum on March 27th at ~21:00 UTC (thick curve) given the chemical distribution illustrated in Figure 3.10. Also shown is the theoretical activation spectrum assuming chemistry is constant with d_p (thin curve). The grey curve shows the $p(S_c)$ distribution from the "comprehensive analysis".

The thin solid line illustrates the assumption that the chemical composition for all particle sizes can be described by a single $p''(SVF)$ distribution. In this example, failing to account for the chemical variability as a function of particle size results in an overestimate in the activation fraction at the lower supersaturations. By looking at the activation spectra of the 40, 60 and 80 nm particles during the same time, we can see that the reason is clearly that the larger multiply-charged particles are less hygroscopic, and thus the activation of these larger particles occurs at a higher supersaturation than otherwise expected. The fraction of externally-mixed unactivated particles decreases with size, so we don't expect that the multiply-charged shoulder has shrunk due to fewer

CCN at this size. Similarly, the chemical dispersion as a function of particle size cannot explain the lack of a shoulder in the activation spectrum, since the dispersion doesn't change significantly with size for this example. The thick solid line shows the theoretical activation spectrum accounting for the size resolved particle chemistry, using Equation 3.18. It should be emphasized that this curve is derived from the chemical composition inferred from the activation spectra of the other particle sizes, which are completely independent measurements from the 100 nm activation spectrum. Thus, the comprehensive analysis is not a "fit" but rather an independent "explanation" for the shape of the observed activation spectra.

Particle Size Distribution Approximation

We analyzed the effect of the DMA sheath-to-aerosol-ratio (SAR) on the slope of the activation spectrum. Using the size dependent $p''(SVF)$ distribution from the example above and varying the SAR in our calculations of $p'(d_p)$ for a 100 nm nominal particle size, we derived the predicted activation spectra using Equation 3.18. Surprisingly, we see that varying the SAR from 2.5 to 10.0 hardly has any discernable affect on the activation spectrum given the chemical variability inferred from the ambient measurements.

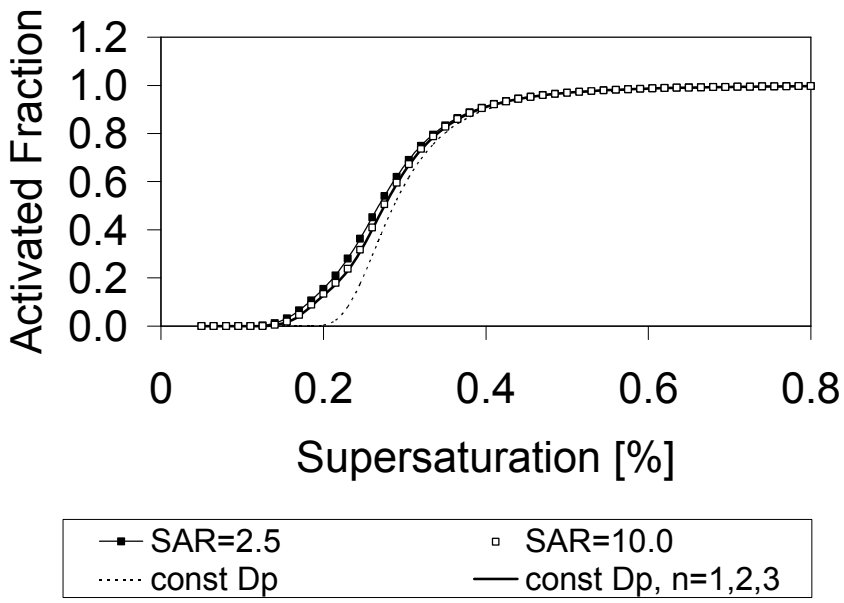


Figure 3.13. Theoretical activation spectra given the inferred ambient chemical distribution illustrated in Figure 3.10, varying the DMA sheath-to-aerosol ratio (SAR) from 2.5 to 10.0. Also shown is the activation spectrum assuming a completely monodisperse aerosol population (labeled "const d_p") and the activation spectrum assuming three monodisperse aerosol populations, each representing the fraction of singly, doubly and triply charged particles, respectively (labeled "const d_p, i = 1, 2, 3")

The $p''(SVF)$ distribution dominates, and the change of particle chemistry with size further smoothes the activation curve, so that variability in the width of the relatively narrow $p'(d_p)$ distribution becomes negligible. However, as shown in Figure 3.13, assuming a constant nominal diameter (dotted line) does have a large affect on the activation spectrum. The doubly and triply charged particles, whether broad or narrow in their size distribution, have an equally important affect on the activation spectra for this example. Also plotted in Figure 3.13 (thick solid line) is the activation spectrum assuming three particle sizes (d_p^{1+}, d_p^{2+} and d_p^{3+} corresponding to i = 1, 2, 3) with relative fractions governed by the charging, transmission and counting efficiencies for those particle sizes and their relative concentrations in the atmosphere. We represent this

approximation to the $p'(d_p)$ distribution as $p_i(d_p)$, which is equivalent to assuming an infinite SAR. We see that using these three diameters alone captures the essential particle size variability, and approximates the activation spectrum given a SAR of 10.0. We also see that only when the chemical variability is small that the DMA SAR makes a significant difference.

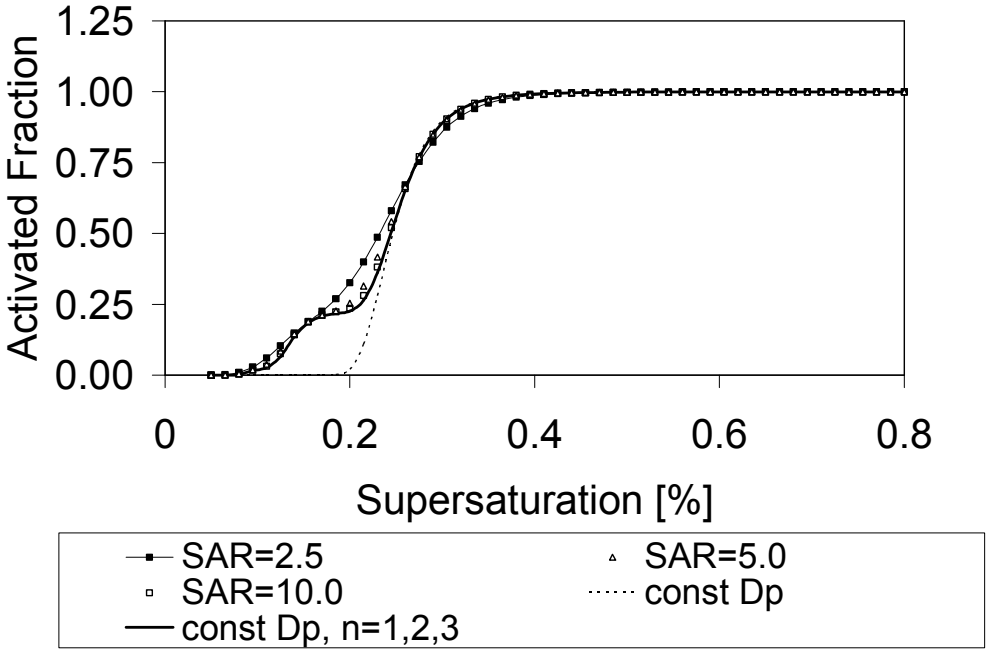


Figure 3.14. Same as Figure 3.13 except that the chemical distribution is assumed to be narrow (with σ = 0.05) and constant with particle size (E, $\overline{SVF}$ and $\sigma \neq f(d_p)$).

Figure 3.14 shows the activation spectra with an assumed SAR of 2.5, 5.0 and 10.0 given a hypothetical $p''(SVF)$ distribution with σ = 0.05 that is constant with particle size. In this case, the lowest SAR has a noticeable, although minor, broadening affect on the slope of the activation spectrum. For our ambient measurements σ is rarely as low as 0.05 and SVF^* consistently decreases with particle size. Thus, we believe that

Figure 3.14 may be an extreme case and that $p_i(d_p)$ may often be used when the SAR is above 5.0, considerably reducing the computational cost of the comprehensive analysis.

The $p'(d_p)$ approximation may be used directly in Equation 3.18, as illustrated in Figures 3.13 and 3.14, or by modifying the sigmoidal fit method to include 3 independent sigmoidal functions.

$$\frac{d}{dS}\left(\frac{CCN}{CN}\right) = \sum_{i=1}^{3} E_i^* \cdot p_i(D_p) \cdot \left[\frac{C_i \left(\frac{\omega_i \cdot SVF^{-1/2}}{S_i^*} \right)^{C_n - 1} \omega_i \cdot SVF^{-3/2}}{2S_i^* \left[1 + \left(\frac{\omega_i \cdot SVF^{-1/2}}{S_i^*} \right)^{C_i} \right]^2} \right] \left(\frac{dSVF}{dS} \right)_i \qquad (3.19)$$

where ω_i and $\left(\frac{dSVF}{dS}\right)_i$, calculated from Equations 3.8 and 3.11, respectively, are determined using d_p^{1+}, d_p^{2+} and d_p^{3+} (corresponding to i = 1, 2 and 3). For each activation spectrum, Equation 3.19 uses 9 fit parameters (3 for each of the following, E_i^*, C_i and S_i^*). The sigmoidal parameters are then parameterized as functions of d_p, so that all 4 particle sizes are simultaneously fitted, reducing the number of fit parameters to 6-9 (with 2-3 parameters each to describe $E_i^*(d_p)$, $C_i(d_p)$ and $S_i^*(d_p)$). We refer to the resulting chemical distribution as $p_i^s(SVF)$.

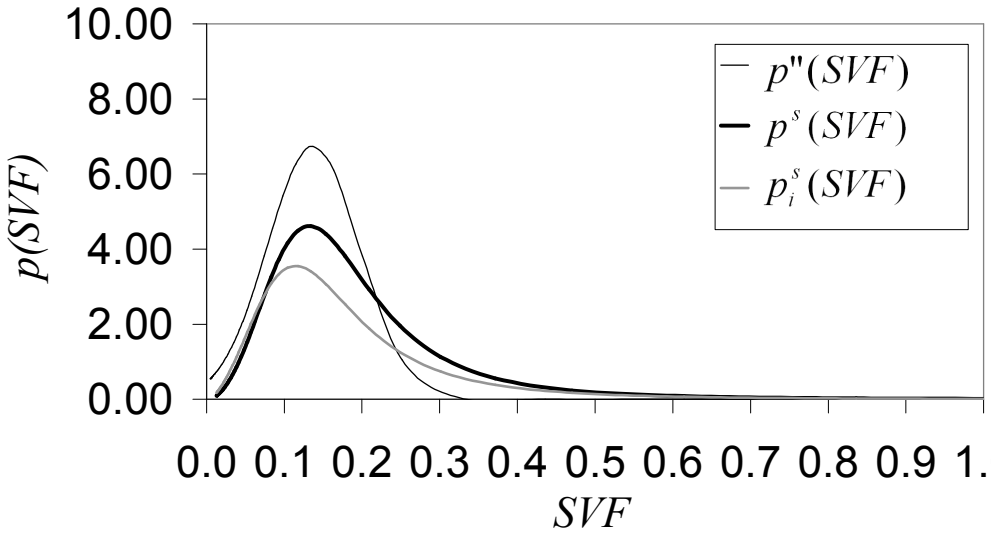


Figure 3.15. Same as Figure 3.11 with the addition of the SVF probability distribution calculated using the particle size distribution approximation, $p_i^s(SVF)$

Figure 3.15 shows the $p_i^s(SVF)$ distribution for ~07:00 GMT on March 30th, which are skewed due to the nonlinear dependence of S_c on SVF. $p_{i=1}^s(SVF)$ can be directly compared with the other methods for inferring chemical distributions, and we see that the peak SVF is underestimated by ~ 0.02, yielding a relative error of ~12%. However, due to the skew in the distribution, the average SVF of the new sigmoidal fit with $i = 1$ is much closer to the peak SVF from the comprehensive analysis than the average SVF from the sigmoidal fit neglecting multiply-charged particles.

Results

In Figure 3.16 e) we plot $p^s(SVF)$ as a function of time for the 100 nm nominal particle size from March 16-27th during the MIRAGE campaign. This is essentially

turning Figure 3.11 on its side, with the color intensity representing $p^s(SVF)$ and the x-axis becoming universal standard time (GMT).

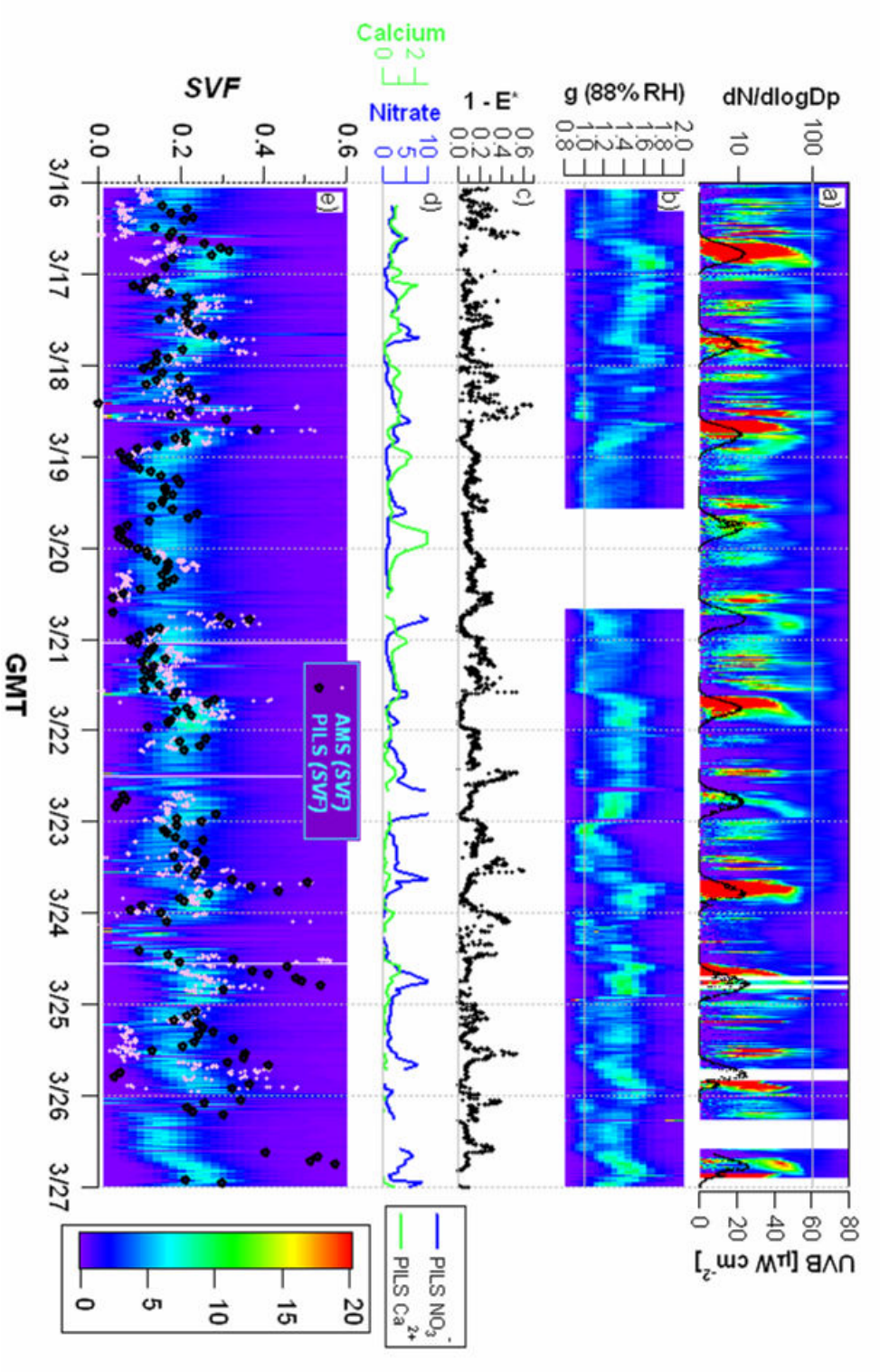


Figure 3.16. Timeseries of a) dry particle size distribution and solar insolation, b) hygroscopic growth factor distribution at 88% relative humidity, c) nonactivated fraction, d) nitrate and calcium ion mass loadings measured with the PILS and e) inferred Scaled solute Volume Fraction (*SVF*) and *SVF* from two direct chemical measurements.

The contour plot of inferred SVF has 3 minute resolution, since every time supersaturation is changed in the instrument, and thus one data point on the activation spectrum has changed, we fit the activation spectrum with a new sigmoid. Assuming that the soluble component can be represented by ammonium sulfate, the CCN soluble volume fraction, ε_s, for 100 nm particles is 26 ± 7% during this time period, which is not far off from the reported ε_s in *Kandler and Schütz* [2007] showing a range from ~10-60% with a best fit of ~35% for 100 nm particles under polluted conditions in central Europe.

Comparing the Inferred and Direct Chemical Measurements

We compare our inferred CCN chemical distribution, $p^s(SVF)$, with two independent measurements of particle chemistry at the T1 site in Figure 3.16 e). The Aerosol Mass Spectrometer (AMS) and Particle Into Liquid Sampler (PILS) provide measurements of particle chemistry for PM_1 and $PM_{2.5}$, respectively. It should be pointed out that the PILS measures only soluble components while the AMS measures only non-refractory components. We use Tapered Element Oscillating Microbalance (TEOM) measurements to constrain the total $PM_{2.5}$ mass. It is expected that the total mass loading, $[TEOM]$, has a bias in insoluble mass as compared to 100 nm particles since a significant fraction of particles with $d_p > 1$ μm are mineral dust, which can contribute substantially to the total mass. In addition, we expect that even given the mass of 100 nm particles, the amount of insoluble material in the CCN active population would still be overestimated, since the mass would include externally mixed particles that do not activate in the CCNc. To account for this, we multiply the mass loading by the fraction

of particles that do activate (using the independent fit parameter, E^*, from our measurements). Since E^* is a number fraction, and not a mass fraction, we account for the difference in density between the activated and unactivated particles, assuming that the activated particles are ammonium sulfate (AS) and that the unactivated particles are dust, to calculate the expected CCN mass. We use this estimate of the dry CCN mass to calculate the CCN soluble mass fraction from the direct chemical measurements.

$$\varepsilon_s = \frac{[s]}{[TEOM] \cdot E^* \cdot (\rho_{AS} / \rho_{dust})} \tag{3.20}$$

Substituting Equation 3.20 into Equation 3.6,

$$SVF = \frac{M_w / \rho_w}{[TEOM] \cdot E^* \cdot (\rho_{AS} / \rho_{dust})} \sum_s \left(\frac{[s] \nu_s \rho_s}{M_s} \right) \tag{3.21}$$

where $[s]$ represents the measured mass loadings for dissolved organic matter (Org), ammonium nitrate (AN) and ammonium sulfate (AS), the latter two of which are measured by both the PILS and AMS. We assume that none of the AN evaporates, however this may not be a correct assumption as the temperature within the laboratory fluctuated between 20 ^{o} and 25^{o} C during the study [*Schaap et al*, 2004]. We use the water soluble organic carbon ($WSOC$) measurements to calculate [Org], with the assumption that [Org]/[$WSOC$] = 2. ν_{Org} is assumed to be 1.0, ρ_{Org} is assumed to be 1.4 g cm^{-3} and the average molecular weight of the water soluble organics (M_{Org}) is

assumed to be 125 amu, determined from Köhler Theory Analysis of filter samples from the T1 site [Padró et al, *in prep*]. To distinguish when we are using the PILS or AMS data in Equation 3.21 for the inorganic content of the aerosol, we use the denotation "PILS (SVF)" and "AMS (SVF)," respectively. When the mass loading of dust is high, we expect the PILS (SVF) and AMS (SVF) to underestimate the SVF of 100 nm particles, since we expect that dust will impact the $[TEOM]$ more significantly than the mass of 100 nm particles. Figure 3.16 d) shows that during times when the PILS (SVF) and AMS (SVF) are lower than our inferred SVF the measured PILS $[Ca^{2+}]$ concentration is often higher, indicating a larger influence of dust. One exception to this, when the PILS (SVF) was low but no significant $[Ca^{2+}]$ was observed, coincided with a local fire within a few hundred yards of the site during midday on March 22nd. One explanation is that the fresh biomass burning emissions were surface active and significantly lowered the surface tension of the aqueous particles thereby increasing their CCN activity but not affecting SVF from the direct chemical measurements. However, it is not clear why the AMS (SVF) does not show the same behavior as the PILS (SVF) during this time.

The hygroscopic growth factor measurements provide additional clues about the particle chemistry and mixing state. Figure 3.16 b) shows the normalized growth factor distribution at 88% Relative Humidity, g(88% RH), obtained with the HTDMA for 100 nm particles. Part c) in Figure 3.16 shows the fraction of particles that remain unactivated, $(1-E^*)$ from the sigmoidal fits of the observed 100 nm activation spectra. When the unactivated fraction is above 20% we observe a completely non-hygroscopic aerosol mode (with a growth factor of 1.0). When there are more nonhygroscopic

particles we typically see a larger fraction of unactivated particles. One exception is during the evening after the local biomass burning event on March 22nd. Although almost all the particles are nonhygroscopic during this time period, the fraction of particles that remain unactivated is only about 20%.

We plot the particle size distribution in Figure 3.16 a), showing frequent new particle formation events during the day, with associated growth that sometimes stretches up to as large as 100 nm. We used the particle size distribution measurements to estimate the particle mass for a given particle size to compare with the particle time-of-flight (PTOF) mode operation of the AMS, which gives composition as a function of size, but we have left this analysis out of the current study, mainly because the results were extremely noisy. However, it is worth remarking that the difficulty of determining size resolved chemistry for CCN even with direct chemical measurements illustrates the utility of our analysis method and dataset, which give compositional information directly relevant for climate studies regarding both the internally and externally mixed particles. The reason that it is difficult to calculate the SVF of CCN is that we must take the ratio of two independent measurements, the soluble mass and the total mass, neither of which are well-constrained over a small particle size range, and both of which can change rapidly with time. Furthermore, assumptions must be made regarding the particle mixing state. The solute mass from the AMS measurements are not well-constrained for the small amount of mass in a narrow slice of the aerosol population at 100 nm, in addition to the fact that in the PTOF mode of operation there is more time for the volatile compounds to evaporate and be lost from the analysis. Furthermore, it must be assumed that no refractory components are soluble and that some fraction of the AMS measured

"organics" are soluble (since the WSOC measurements were not size resolved). The total mass of CCN of a given size is not well-constrained because we must assume an effective particle density to convert the particle size distribution data to particle mass. The fact that there may be a significant amount of insoluble mass externally mixed with the CCN particles, and the fact that we don't know the effective density of these particles either, makes it even more difficult to determine the amount of insoluble mass internally mixed in the CCN particles. The ideal instrument would have the ability to classify and chemically analyze single particles in the size range of interest, but even then assumptions would need to be made regarding the properties of the organic constituents (e.g. molecular weight, density and solubility). Thus, we leave it for future research to develop an experimental method that can better validate or test the proposed analysis method in this paper for inferring the CCN SVF.

Figure 3.17 shows the PILS (SVF) versus AMS (SVF) for those measurements that are within 5 minutes from each other. We have also only chosen data when the surface wind speed is greater than 2 m s^{-1} to limit local variability, as the PILS, AMS and CCNc instruments were all in different trailers on the site. From this comparison, we see that the uncertainty in SVF from the direct chemical measurements is on the order of 30%. This does not include any potential biases resulting from the lack of size-resolved mass and chemistry measurements for the CCN population.

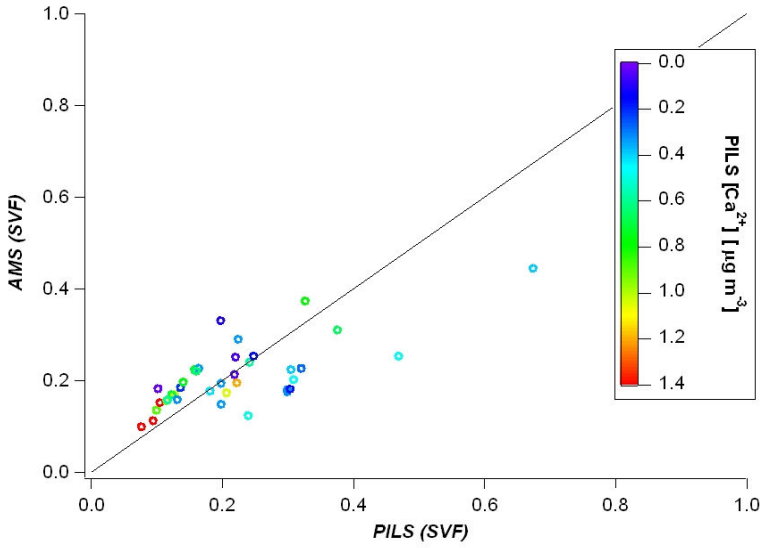


Figure 3.17. Comparing the AMS and PILS (SVF)

We see in Figure 3.16 that our inferred SVF^* is sometimes much lower than expected from the chemistry and particle mass measurements. The reason for this is not immediately clear. The difference between our inferred SVF^* and the AMS (SVF) and PILS (SVF) does not clearly correlate with wind direction (not shown). Most of the data points for which the SVF^* is substantially lower than expected (exceeding the uncertainty in the measurements) occur during daylight hours (between 11 AM and 4 PM). However, not all of the daytime measurements show this trend. Looking again at Figure 3.16 e), we see that the lower than expected SVF^* also occurs mostly after March 23rd, which is considered the third meteorological regime of the study [*Fast et al*, 2007] characterized by higher humidity, afternoon convection, and precipitation in the Mexico City basin, as compared to the second regime (from March 14-23). This third meteorological regime was also characterized by more frequent events with elevated nitrate loadings. We see that the trend of lower than expected SVF^* coincides with

higher nitrate concentrations, which may mean that some of the nitrate has evaporated in our CCN measurements, either before or after classification in the nanoDMA. This could decrease both the particle size and the amount of solute for the particles entering the CCNc, both of which would increase the particle critical supersaturation (and thereby underestimate the SVF^*).

Diurnal Behavior of CCN Activation

We plot in Figure 3.18 the SVF^* and $(1-E^*)$ parameters from the sigmoidal fits of the CCN activation spectra and a fit of the average solar intensity (UVB) as a function of the local time of day for all data from March 16th-31st. The two sigmoidal parameters are independent from each other in our analysis but show similar trends. We see consistently that during the day the fraction of unactivated particles, $(1-E^*)$, decreases, while the soluble content of the activated particles, SVF^*, increases. The SVF^* of the activated particles reaches a maximum about an hour after local noon, suggesting that photochemical processes are dominating. Several mechanisms to explain the diurnal behavior of SVF^* are plausible, all of which may be consistent with the observed increase in SVF^* during the day: 1) photochemical oxidation of gas phase chemical species and subsequent condensation of low volatility products, 2) coagulation of freshly formed particles resulting from new particle formation events, 3) photochemical oxidation in the particle phase adding functional groups to the organic constituents already present. The diurnal pattern of the mixing state is likely more influenced by the breakup of the planetary boundary layer, bringing an influx of more hygroscopic aged

particles from aloft, since there is such a rapid decrease in the unactivated fraction at 9:00-10:00 am local time.

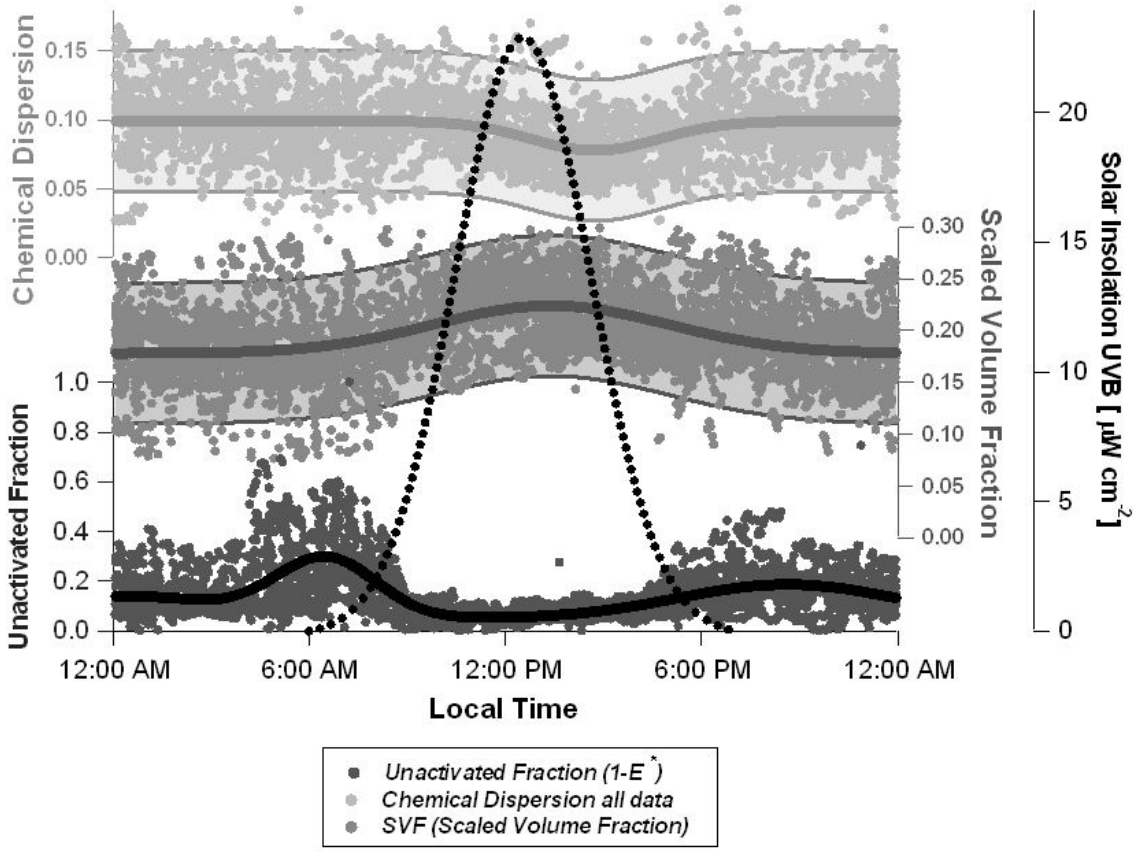


Figure 3.18. Diurnal behavior of a) inferred chemical dispersion, b) inferred SVF^*, c) unactivated fraction and d) solar insolation

We also plot the chemical dispersion, calculated using both the sigmoidal C and S^* fit parameters in Equations 3.9-3.10 for the whole study. The chemical dispersion appears to have a consistent diurnal pattern as well, but with a minimum in the mid-afternoon about an hour later than the maximum in SVF^*.

Potential Mechanisms for Chemical Broadening

We hypothesize that condensation of a more hygroscopic species decreases the chemical dispersion of the CCN population, $\sigma(SVF)$. Figure 3.19 shows a hypothetical $P^S(SVF)$ distribution (solid line), and then shows how the chemical distribution shifts when the mass is doubled by condensation of ammonium sulfate (AS) onto the particles (dotted line). We assume that the ammonium sulfate condenses equally onto all particles (since we are interested in only one particle size). To simply things further, we assume that all particle sizes originally had the same $P^S(SVF)$ distributions and number concentrations, and that the addition of solute does not change the particle density or shape.

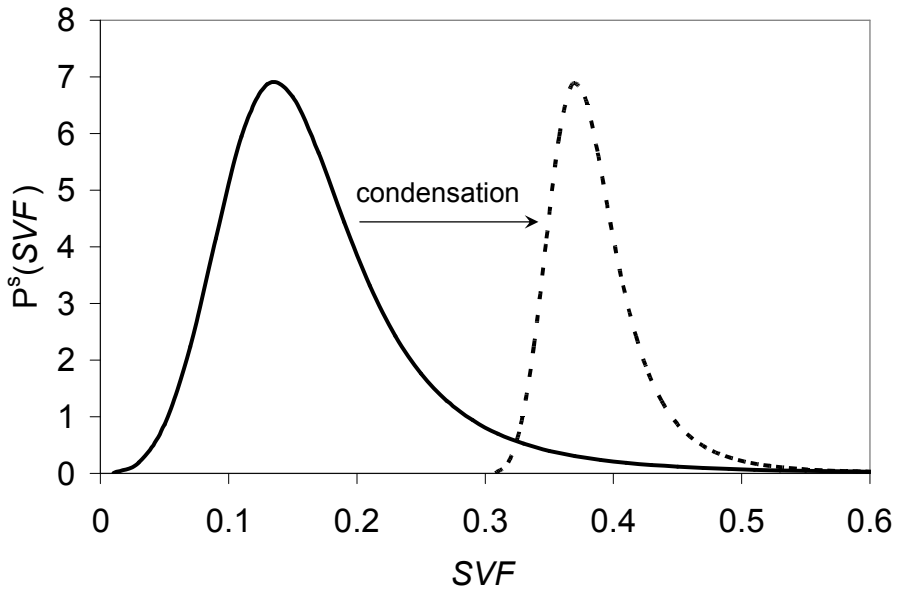


Figure 3.19. Simple model to illustrate a mechanism for narrowing the chemical distribution, by condensation of hygroscopic compounds

With the addition of soluble mass, 80 nm particles grow into 100 nm particles, but the $P^S(SVF)$ distribution is not simply shifted to the right. Those particles originally with low SVF are impacted more than particles that already have a high soluble fraction, because the additional soluble mass increases both the solute mass and the total mass. For the 80 nm particles,

$$SVF_1 = \frac{\varepsilon_s \nu \rho_s M_w}{\rho_w M_s} = \frac{m_{s1}}{m_{T1}}\left(\frac{\nu \rho_s M_w}{\rho_w M_s}\right) \tag{3.21}$$

where m_{S1} and m_{T1} are the solute mass and the total mass, respectively, of the 80 nm CCN particles (m_{s1}/m_{T1} is assumed to be constant for all particle sizes, originally). Then, with the addition of solute, for the 100 nm particles,

$$SVF_2 = \frac{m_{s1} + m_{s2}}{m_{T1} + m_{s2}}\left(\frac{\nu \rho_s M_w}{\rho_w M_s}\right) \tag{3.22}$$

For this hypothetical example, the SVF increases from 0.13 to 0.37, while the $\sigma(SVF)$ decreases from 0.09 to 0.04. Of course, the initial size resolved chemistry also affects the resulting chemical distribution; if the 80 nm particles were actually less hygroscopic than the 100 nm particles, the change in hygroscopicity of the 100 nm particles over time would be less significant. It also ignores the fact that when ammonium sulfate condenses on the externally mixed unactivated particles, it may shift these particles into the CCN active spectrum (with a corresponding decrease in the

unactivated fraction, $1 - E$), which would *increase* the chemical dispersion of the CCN, at least initially.

During the day and night, emissions of primary aerosol from various sources increases the fraction of externally mixed unactivated particles, $(1 - E^*)$. When these primary particles coagulate with CCN, the soluble content of the CCN decreases while the chemical dispersion of the CCN at a given size is likely to increase. Figure 3.20 shows a hypothetical $P^S(SVF)$ distribution, and the affect of coagulation with a less soluble aerosol population, given the same $\sigma(SVF^*)$ and same particle size. The resulting chemical distribution is broader than the initial distributions.

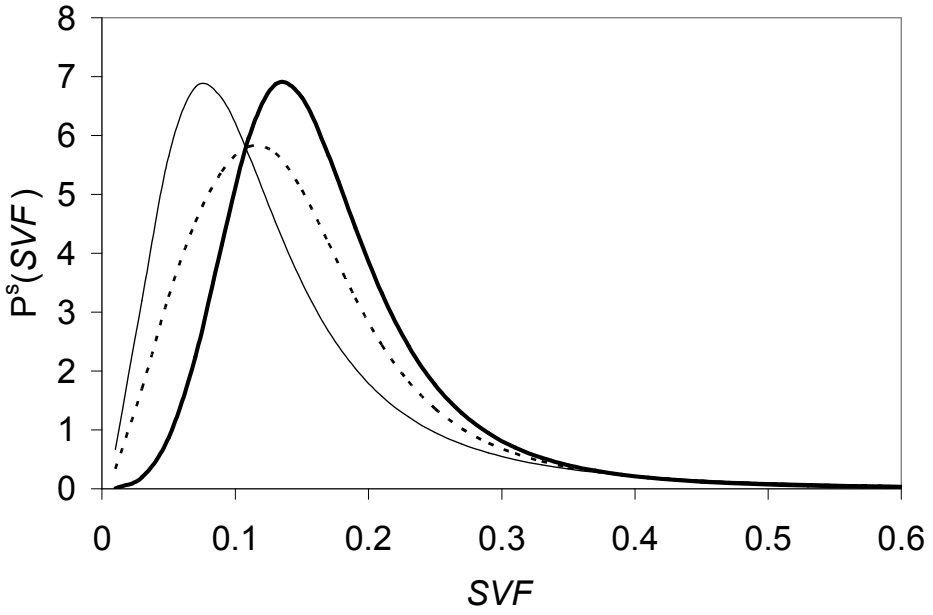


Figure 3.20. Simple model to illustrate a mechanism for broadening the chemical distribution, by coagulation with externally mixed particles

Coagulation is a much more complex issue than condensation, however, since the particle size distribution and size-resolved chemistry must be taken into account. We present this example as a simple model to illustrate one possible mechanism for increasing the chemical dispersion.

For the days March 27-31 the Aerodyne mobile lab was at the T1 site with a quadrupole aerosol mass spectrometer measuring the composition of single particles with vacuum aerodynamic diameter from 250 to 400 nm. Direct chemical measurements such as this which can provide mixing state information are invaluable for validation of our dataset and analysis method. Unfortunately, the difference in particle size ranges observed precludes quantitative comparisons. In Figure 3.21 we plot the fraction of 100 nm particles that remain unactivated up to almost 1% supersaturation in the CCNc and the number of aerosol particles composed primarily of "Hydrocarbon-like Organic Aerosol" (HOA), a chemical tracer for primary emissions from local, combustion related sources, detected with the single-particle AMS [*Cross et al*, in preparation] as a function of the local time.

Unfortunately, the fraction of 'pure' HOA particles could not be reliably obtained since the counting statistics were so poor at these large sizes. Nevertheless, we see a clear picture of primary particles being emitted during the morning rush-hour causing a greater fraction of the particles to remain unactivated. From this, we can say definitively that the observed diurnal behavior of mixing state is due in large part to human activities. This also suggests that the aerosol aloft, which is typically more aged, is both more hydrophilic and more oxygenated; when the planetary boundary layer breaks up, the number of 'pure' HOA particles and the unactivated fraction both sharply decrease.

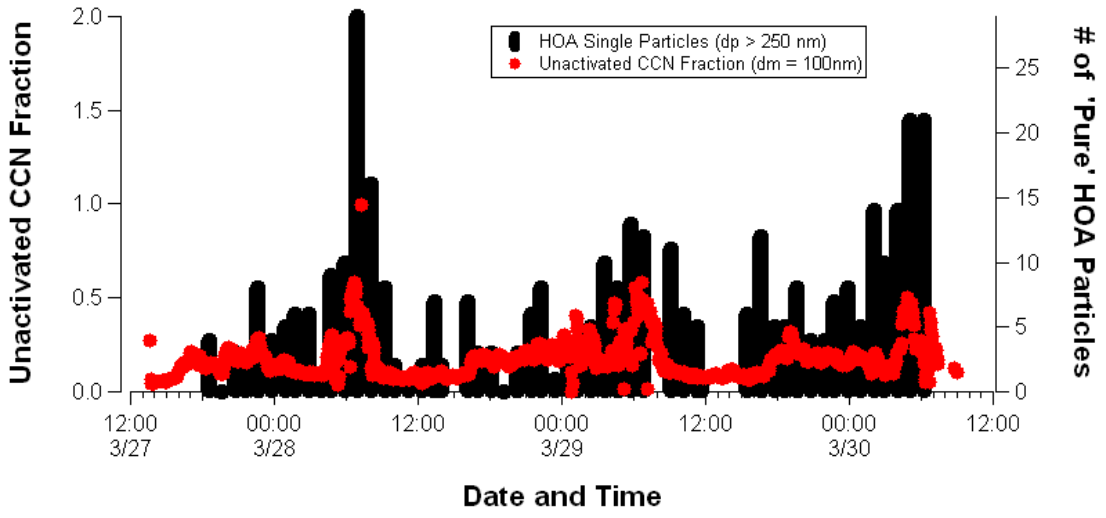


Figure 3.21. Comparing the fraction of unactivated particles with the number of pure HOA particles observed with a single-particle AMS

For almost the full day on March 19th and 20th 2006, the winds steadily transported the Mexico City plume to the northeast, towards the T1 and T2 surface sampling sites [*Fast et al*, 2007]. We highlight the diurnal variability for these two days in comparison to the rest of the field campaign in Figure 3.22. During midday, the trends for these two pollution outflow days, emphasized with straight lines through the data during midday, clearly differ from the average trend, with lower SVF and higher chemical variability than on average. We do not plot the unactivated fraction for the pollution outflow days, as it is not remarkably different from the average.

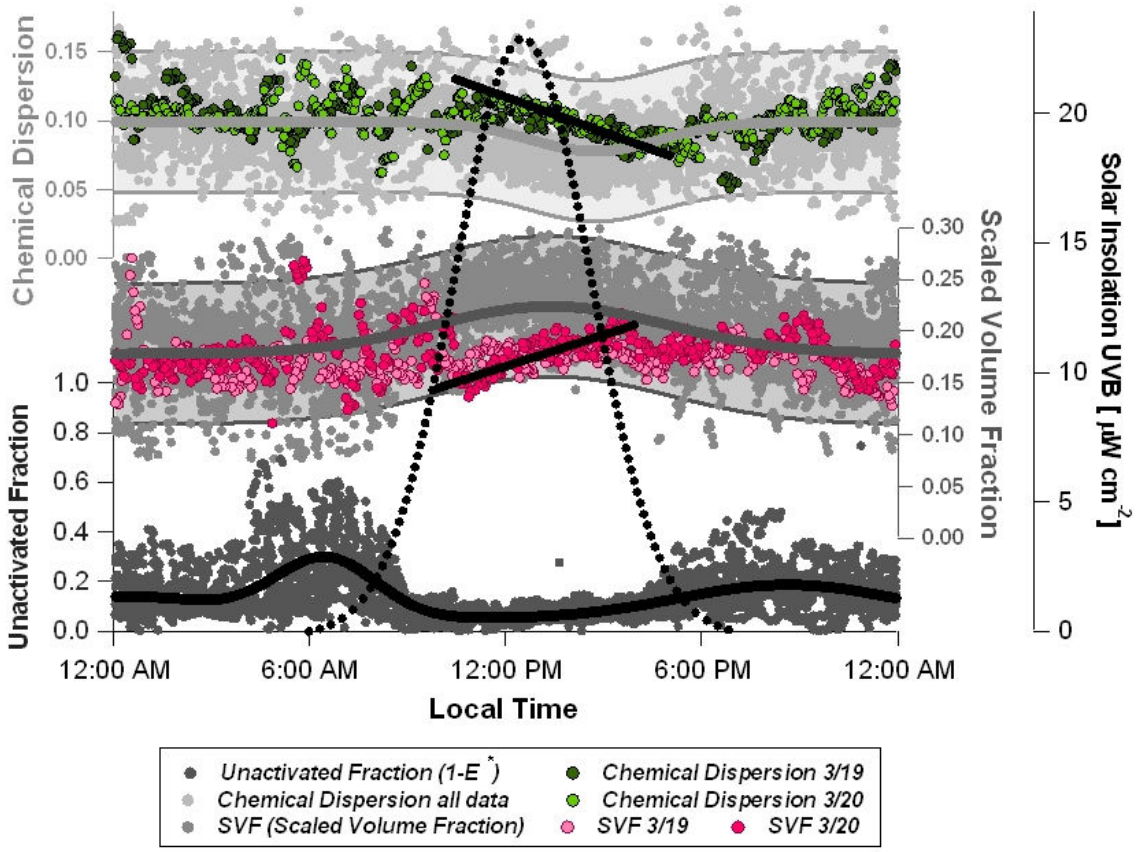


Figure 3.22. Diurnal pattern of two pollution outflow days, compared to the average

If photochemical aging is causing the CCN to become more hygroscopic on average during the day, then perhaps the lower SVF for the pollution outflow days simply indicates that the CCN are less aged.

Quantifying Uncertainties

Figure 3.23 compares the inferred chemical dispersion, $\sigma(SVF^*)$, calculated from Equation 3.11 to the chemical uncertainty, ΔSVF^*, calculated from Equation 3.10 for 100 nm particles throughout the whole study. We estimate that the uncertainty in S^* is 10% of S^*, which generally results in $\Delta SVF^* < \sigma(SVF)$. When S^* is low, the CCN

tend to have a more homogeneous composition (as discussed earlier), which lowers $\sigma(SVF)$. However, when S^* is low, ΔSVF^* is relatively high, since ΔSVF^* is proportional to $\Delta S^*(S^*)^{-3}$, which we approximate as $0.1(S^*)^{-2}$. We cannot accurately quantify the chemical dispersion during the times when $\Delta SVF^* > \sigma(SVF)$, but we can say that the chemical dispersion is relatively low. The lowest $\sigma(SVF)$ is limited by the particle size dispersion, which controls the slope of the activation spectrum when the chemical dispersion is small. The sigmoidal fit parameter C was constrained to values lower in magnitude than 15 for particles with characteristic critical supersaturation greater than 0.3%, using the calibration activation spectra as our guideline for the maximum attainable slope. The chemical dispersion may be lower than this lower limit (denoted as C = -15), but we would be unable to see it.

The chemical dispersion (one standard deviation in the Scaled solute Volume Fraction) ranges from 0.05-0.15, while the chemical uncertainty of SVF^* is usually below 0.075. This means that we can resolve the mean of the chemical distribution at least as well as our inferred chemical dispersion. The upper limit of the chemical dispersion is constrained by the range of supersaturations we operated. When the chemical dispersion is greater than ~0.15, these particles may have a significantly different enough composition to warrant classifying them as an external mixture. Our analysis method, as presented, does not have the ability to resolve separate "chemical modes" within the CCN active population. Although this could be done, it would require a significant amount of additional work.

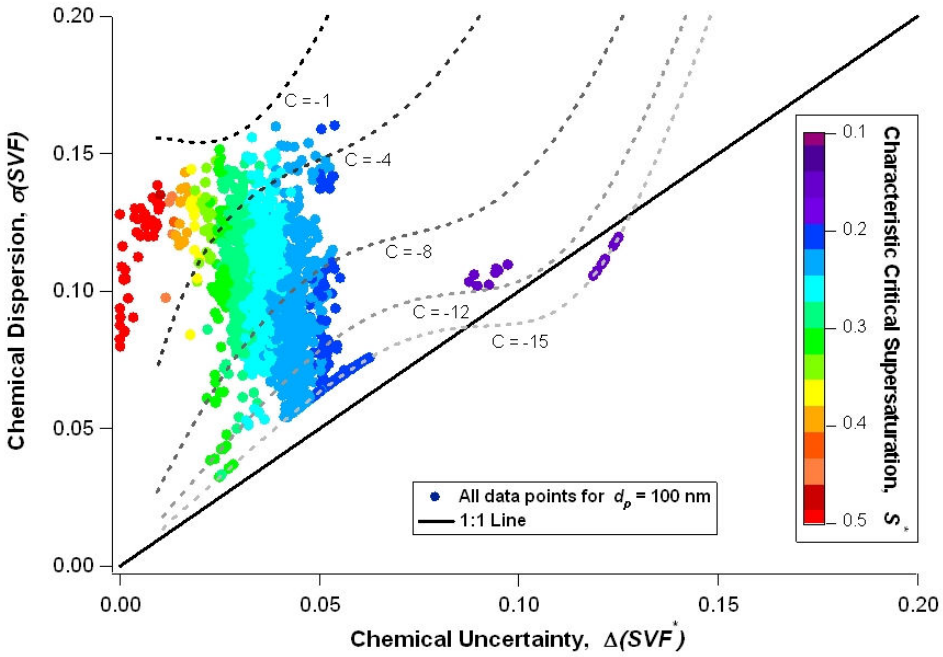


Figure 3.23. Chemical dispersion versus the uncertainty in SVF^*

Droplet Growth Kinetics

In Chapter 1, we showed that organics may affect droplet growth kinetics and can have a strong impact on droplet number and size distribution. Slightly soluble compounds may take time to dissolve, adding solute slowly to the growing droplet, and film-forming compounds may inhibit water molecules from "sticking" to the droplet surface upon collision. However, it is not known whether or how frequently this occurs with ambient particles. We investigate the droplet growth kinetics of the ambient particles under the controlled conditions of the CCNc instrument, using the droplet size distribution measured with the optical particle counter at the outlet of the CCNc.

The driving force for condensational growth is the difference between available water vapor and equilibrium water vapor concentrations. The equilibrium water vapor pressure curve (i.e. "Köhler curve") is unknown for ambient particles, but we have shown

how we can deduce the particle critical supersaturation, the maximum of the Köhler curve. We assume that the critical supersaturation is the only difference between Köhler curves for different particle sizes and throughout the day, which means that the equilibrium water vapor pressure essentially goes to zero immediately after activation. Thus we assume that the CCNc instrument supersaturation controls droplet growth, following activation. This is a good assumption when the instrument supersaturation is not depleted, which has been shown to occur only at CCN concentrations exceeding ~5,000 cm^{-3}. It should be noted that this assumption is not valid for ambient clouds, which have a sharp maximum supersaturation near cloud base due to rapid condensational growth, which leads to the potential for deactivation [*Nenes et al*, 2001]. In the CCNc, the particle critical supersaturation mainly controls the timing of activation; particles with a relatively low critical supersaturation will activate first, followed by particles with relatively high critical supersaturations, up to the point where the maximum supersaturation in the CCNc is attained. Thus, comparing particles of the same size, we would expect that particles with higher inferred SVF would activate more quickly in the CCNc and would have more time to grow, and would hence have a slightly larger droplet diameter at the exit of the instrument.

Figure 3.24 shows the average droplet diameter for 100nm dry particles at different CCNc supersaturations throughout the entire study; each point represents an average of 16 seconds of measurements, every three minutes. Also shown is the inferred SVF* for 100nm dry particles. It is clear that the droplet growth in the CCNc is mainly controlled by the instrument supersaturation and that changes in the SVF* during the study have less of an affect on the droplet growth, with variability on average that is

typically less than the OPC size bin of 0.5 μm. Error bars are shown for the 0.3% supersaturation case, denoting one standard deviation in droplet size. The standard deviation of supersaturation throughout the study is displayed in the key for each case.

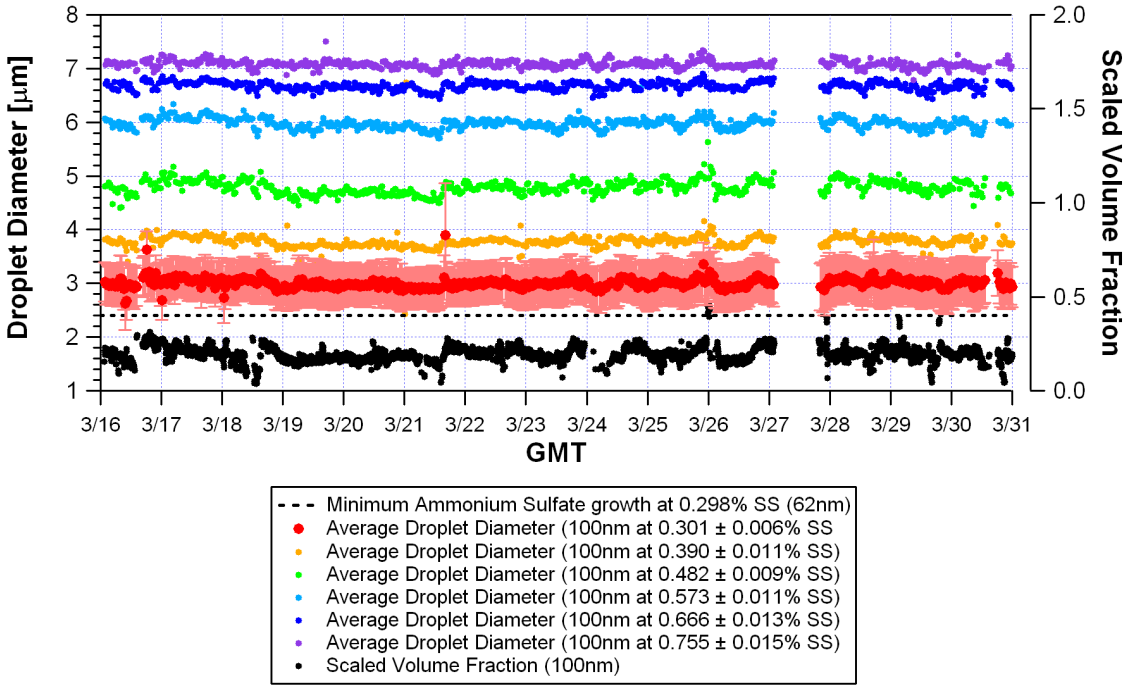


Figure 3.24. Average droplet diameter for 100nm dry particles throughout the entire study at different CCNc supersaturations, compared with SVF^*. The dotted line shows the minimum droplet diameter expected at ~0.3% SS according the droplet growth behavior of ammonium sulfate particles.

Also shown in Figure 3.24 for comparison is the measured droplet growth for classified 62 nm ammonium sulfate particles exposed to 0.3% supersaturation in the CCNc at 0.75 L min^{-1} total flow rate and ~800 mbar ambient pressure. This is the minimum droplet size expected for these conditions, since 62 nm is the minimum particle size to activate for ammonium sulfate at 0.3% supersaturation. These ammonium sulfate particles are the last to activate, as they require precisely the concentration of water vapor

available. The droplets also start off relatively small, and thus take additional time to "catch up" to less hygroscopic but larger droplets with the same critical supersaturation. Thus, if droplets are significantly smaller than this lower limit, given the same conditions within the instrument, we know that the droplet growth must have been delayed for some reason. This does not appear to occur when looking at the average droplet size. However, there is a small fraction of droplets (not shown) that are smaller than this lower limit, as apparent when the error bars in Figure 3.24 dip below the minimum droplet growth, consistent with the ~2% of particles *Chuang* [2003] estimated with kinetically limited growth in Mexico City.

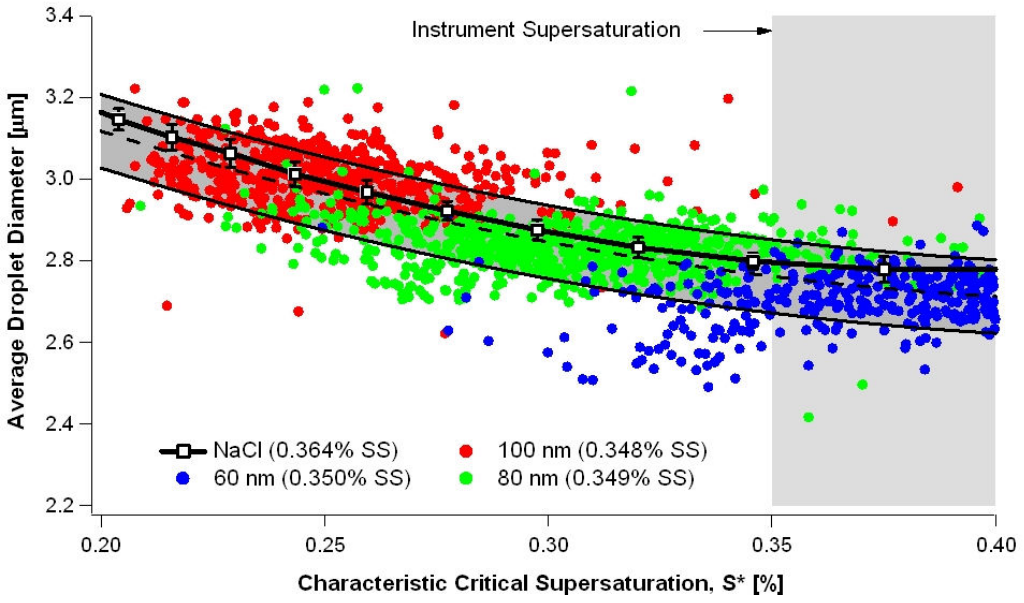


Figure 3.25. Average droplet diameter as a function of the characteristic critical supersaturation for all data at an instrument supersaturation of 0.35% SS, compared to average droplet diameter of NaCl particles at 0.364% SS

Figure 3.25 shows the average droplet diameter for each of the four particle sizes throughout the study exposed to 0.35% supersaturation in the CCNc as a function of the characteristic critical supersaturation, S*.

This highlights the affect of particle critical supersaturation on droplet growth. Recall from chapter 2 that the outlet droplet diameter, $D_p\big|_{out}$, can be approximated from the critical diameter, D_c, the instrument supersaturation and the time available for droplet growth following activation, τ:

$$D_p\big|_{out} = \sqrt{D_c^2 + 2GS\tau} \tag{3.23}$$

where the critical diameter is inversely proportional to the critical supersaturation. Particles with lower critical supersaturation activate earlier and have a larger critical diameter, thus they have a slightly larger outlet droplet diameter when exposed to the same supersaturation profile in the CCNc. For characteristic critical supersaturations above the instrument supersaturation, we expect that multiply-charged particles are contributing significantly to the droplet sizing. For example, this means that for droplets with S* above 0.482% SS, doubly-charged 60 nm dry particles are most likely contributing more to the resulting droplet diameter than the singly-charged 40 nm dry particles. We also expect that the doubly charged particles skew the average droplet diameter to larger sizes when S* is less than the instrument supersaturation, and this is why we see a slight increase in the average droplet diameter with dry particle size at the same characteristic critical supersaturation.

In Figure 3.26 we plot the average droplet diameter for the whole study as a function of the CCNc instrument supersaturation for the four observed dry particle sizes at 0.75 L min^{-1} total flow rate.

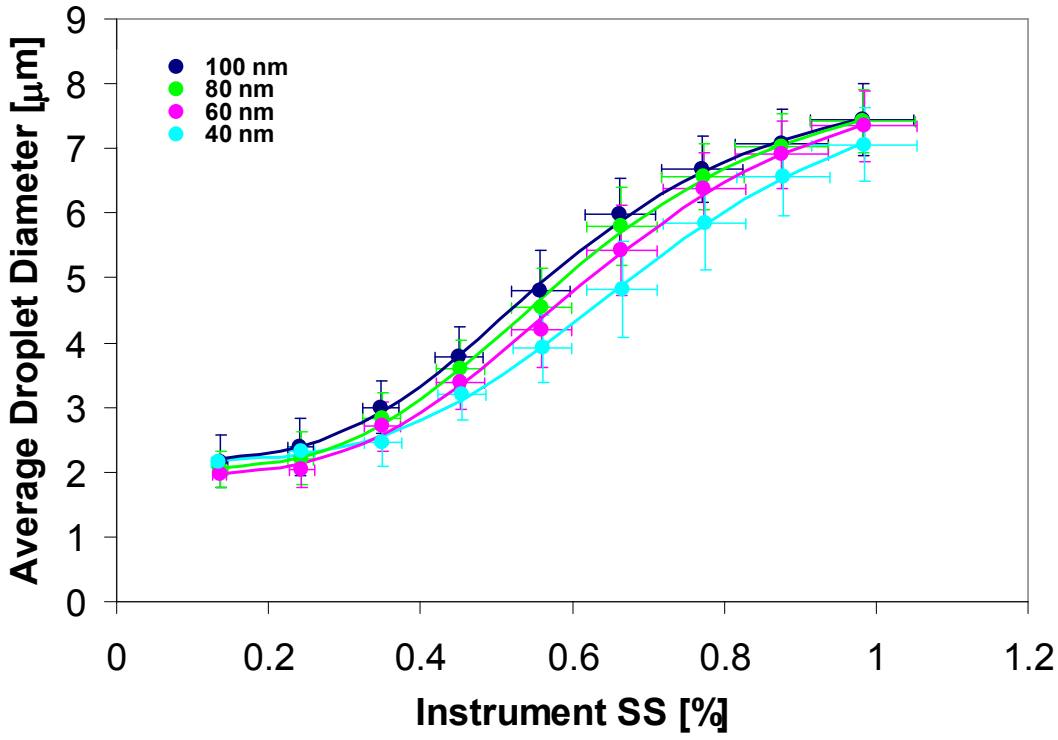


Figure 3.26. Average droplet diameter as a function of the CCNc supersaturation, averaged over the whole study

The vertical error bars represent the variability in the average droplet diameter throughout the entire study, calculated separately for each supersaturation and each dry particle diameter. The horizontal error bars denote a flat 8% error in the instrument supersaturation [*Rose et al*, 2007]. The droplet growth is slightly greater for larger dry particle diameters, as expected due to their lower critical supersaturation, larger critical diameter, and larger doubly-charged particles. However, at the highest and lowest

instrument supersaturations the discrepancies for the droplet growth of different dry size particles becomes much less noticeable. At the lowest instrument supersaturations we do not expect that the singly-charged particles activate, and thus for these cases droplets resulting from the doubly-charged particles are expected to dominate the droplet size measurement. This is why we see a leveling off in the average droplet diameter at the lower instrument supersaturations.

Conclusion

We obtained and fit the CCN activation spectra for a several week long ground-based study outside of Mexico City using sigmoidal functions to infer the size-resolved chemical composition and mixing state of the particles (from 40-100 nm). The activation spectra are thoroughly analyzed and the affect of the particle size distribution, DMA transfer function and multiply-charged particles are addressed. We present three different methods for fitting the activation spectra to obtain probability distributions of a scaled CCN solute volume fraction.

We compare our inferred composition with the average composition estimated from direct chemical and particle mass measurements at the site. Agreement is good except when the amount of dust is high (whereby we underestimate the solute volume fraction estimated from the direct measurements) and when the ammonium nitrate is high (which we believe evaporated to some extent in the instrument, whereby our inferred solute volume fraction is underestimated). We see that the inferred CCN solute volume fraction is relatively insensitive, regardless of wind direction, rain, dust, or local biomass

burning events. The most obvious trend is a diurnal pattern with greater fraction of CCN during the day and also lower chemical dispersion during the day.

The rate of droplet growth does not appear to be delayed, when comparing to the droplet growth of ammonium sulfate CCN. The CCNc supersaturation is the largest predictor of droplet size at the exit of the instrument, although the characteristic volume fraction and particle diameter also play a minor role.

CHAPTER 4

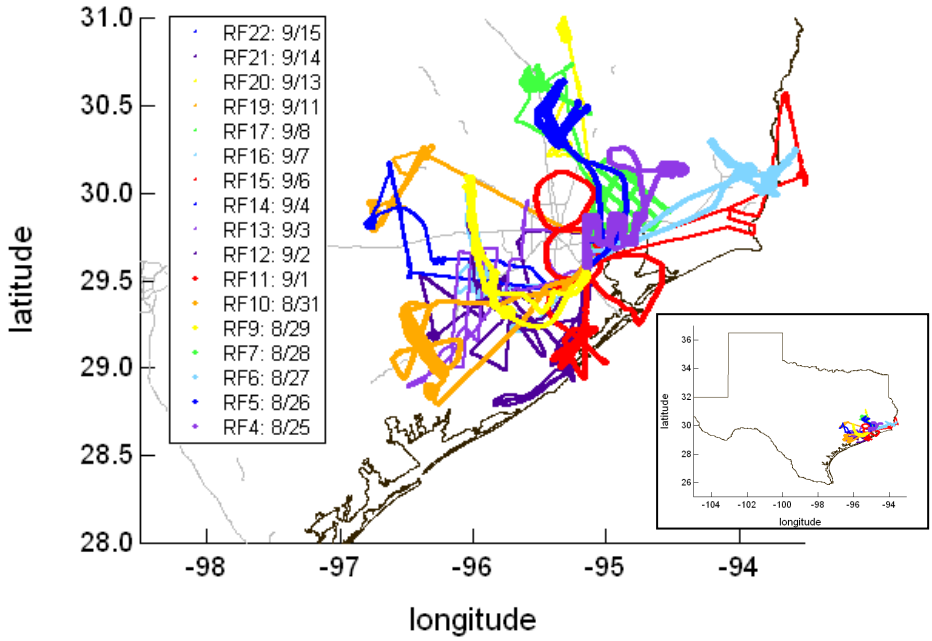
CCN CLOSURE IN THE POLLUTED BOUNDARY LAYER OVER HOUSTON, TX DURING THE GULF OF MEXICO ATMOSPHERIC COMPOSITION AND CLIMATE STUDY (GOMACCS)

Introduction

Cloud Condensation Nuclei (CCN) closure studies have been performed in different locations around the world to evaluate our understanding of the cloud formation process. These studies have mainly been done in relatively clean environments, and rarely via an airborne platform. CCN closure studies use measurements of the aerosol size distribution (and chemical composition, if available) to predict the number of CCN for a given supersaturation, which is then typically compared with direct in-situ measurements of CCN, by exposing the ambient particles to a controlled water vapor supersaturation in one of various types of CCN counters. *Medina et al* [2007] highlight many of these CCN closure studies. Of the limited number of studies in polluted environments, CCN closure has proved difficult. Under such conditions, Köhler theory often overpredicts the number of CCN for a given supersaturation of water vapor.

We expect that downtown Houston, TX is an ideal place to test the theory of cloud formation, as we expect the aerosol that act as CCN originating from such varied local sources as petrochemical industries and refineries, power plants, ship yards, and the urban Houston plume to be chemically complex.

We sampled the ambient aerosol in and around the Houston, Texas area from August 25th-September 15th, 2006 onboard the Center for Interdisciplinary Remotely-Piloted Aircraft Studies (CIRPAS) Twin Otter during the Gulf of Mexico Atmospheric Composition and Climate Study (GoMACCS)/ Texas Air Quality Study (TexAQS) field campaign. Figure 4.1 shows the flight tracks for the Research Flights (RF) presented, all of which occurred during the daylight hours.



Flight 4.1. Flight tracks for all research flights in the study

Measurements

The concentration of CCN was measured using a Droplet Measurement Technologies continuous flow streamwise thermal gradient CCN counter (CCNc) [*Roberts and Nenes*, 2005; *Lance et al*, 2006]. CCN closure was obtained using the particle size distribution measured by the Dual Automated Classified Aerosol Detector

(DACAD) and the aerosol chemical composition measured by an Aerodyne Aerosol Mass Spectrometer (AMS). The CCNc and AMS were on the same manifold, downstream of a valve that was set to sample either from the main inlet or downstream of a Counterflow Virtual Impactor (CVI). The CVI selectively samples droplets and large particles above 5 μm, and we were switched on to the CVI during constant altitude legs in-cloud. However, the DACAD was not on the sampling manifold that the CCNc was on, and the DACAD instead continuously sampled from the main inlet. Thus, CCN closure of dried cloud droplet residuals using the DACAD size distribution measurements in-cloud is not possible, and measurements in-cloud are excluded from our analysis.

The CCNc supersaturation was calibrated on the ground in Houston at various pressures (by restricting the inlet flow with a valve) using laboratory generated ammonium sulfate aerosol particles in accordance with *Nenes and Medina* [2007]. These calibrations were then used to determine the supersaturation at different pressures and temperatures during the flights, interpolating between the calibrated supersaturations when necessary using the thermal efficiency and supersaturation parameterizations from *Lance et al* [2006]. For many of the flights, the pressure at the inlet of the CCNc was controlled at ~700 mb using a DMT Inlet Pressure Controller (IPC). The IPC adds a supplemental flow in parallel with the CCNc that is greater at higher pressures in order to keep the pressure in the CCNc constant. When the IPC is used, the ambient particle concentrations are corrected, according to the following equation

$$CCN_{amb} = CCN_{meas} * \left(\frac{P_{amb}}{P_{CCN}} \right) \tag{4.1}$$

For CCN closure we are limited by the time resolution of the DACAD, which completes a scan of the full size distribution every 73 seconds. For each 73 second period we calculate the average number concentration of particles above 10 nm (also known as Condensation Nuclei, CN), as well as the average and standard deviations of CCN and supersaturation. We filter out data when the CCNc instrument supersaturation varies by more than 10% during a given time interval. We also filter out those points when the standard deviation of CCN exceeds 20% of the average concentration of CCN and when the ambient pressure changes by more than 1% of the average pressure.

The number of CCN can be predicted using the measured particle size distribution, but some assumption must be made about the chemical composition of the aerosol population, even when direct chemical measurements are available. Chemical properties for the organic or unknown components, such as solubility, surfactant properties, density and molecular weight must often be assumed or inferred. It is also typically assumed that the particles are internally mixed. We assume that the particles are dry when they are measured by the DACAD and yet have a uniform spherical shape.

CCN Closure

Figure 4.2 shows the number of CCN predicted from the size distribution assuming that particles are composed purely of ammonium sulfate, compared to the measured CCN during that same time interval, for all the research flights in Figure 4.1. On average the CCN closure is surprisingly good, even with the hugely simplifying assumption regarding particle chemistry and even with CCN concentrations ranging from less than 100 cm^{-3} to more than 10,000 cm^{-3}. A linear best fit of all the data has a slope

of 1.119 ± 0.029 when forced through the origin, indicating a slight overprediction bias on average.

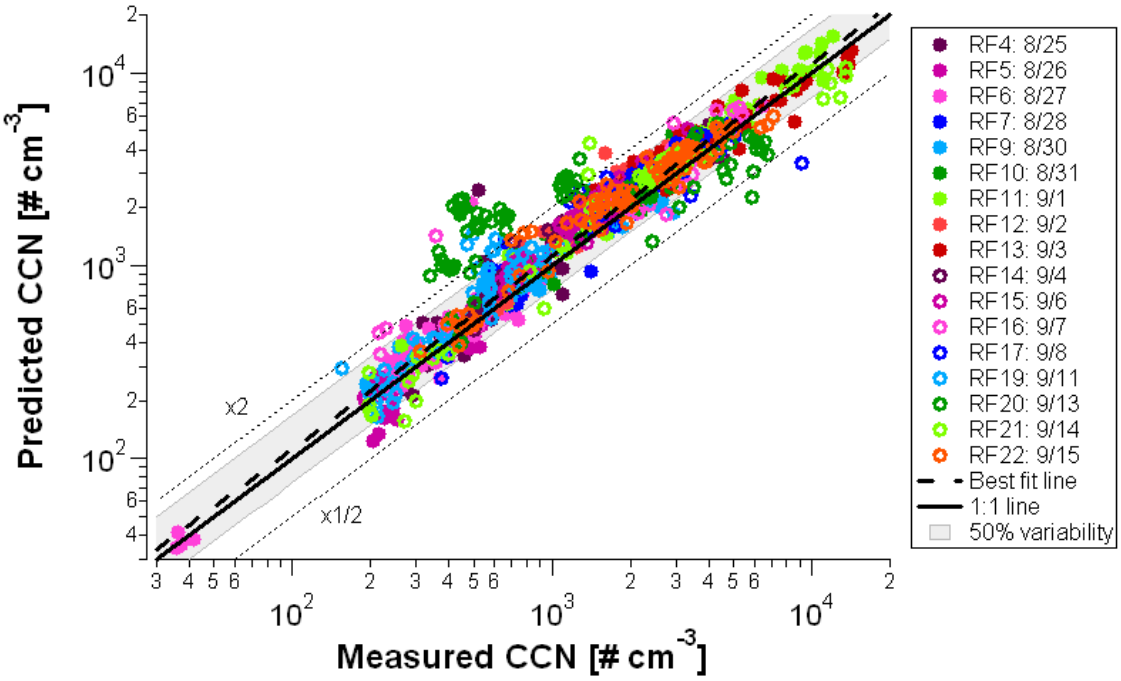


Figure 4.2. CCN Closure for all research flights listed, assuming particles are composed of ammonium sulfate.

Although the bias is on average only about 10%, there can be large discrepancies, at times exceeding a factor of two, between the measured and predicted CCN for individual flights and at times during a given flight. Typically, the variability is within 50% of the best fit. It may also be worth noting that overprediction occurs mainly for CCN concentrations up to 1000 cm^{-3} whereas at greater CCN concentrations underprediction is more prevalent, although this trend is mainly influenced by the CCN closure of one flight (RF20). For the individual flights where we have chemical information, we have the ability to address the variability and biases within the CCN closure.

On September 15, 2006 during Flight 22, the Twin Otter flew along the highly industrialized ship channel starting at the Bay of Houston, followed by a low pass over downtown Houston, with a few transects of the Houston plume downwind of the city before heading back the same way in reverse. Figure 4.3 shows the flight track colored by particle concentrations with a marker size that reflects the ambient pressure. The map also shows the location of the Houston city limit, major roadways and airports and several of the largest point sources for NO_x. We see that the highest particle concentrations are inside the city of Houston.

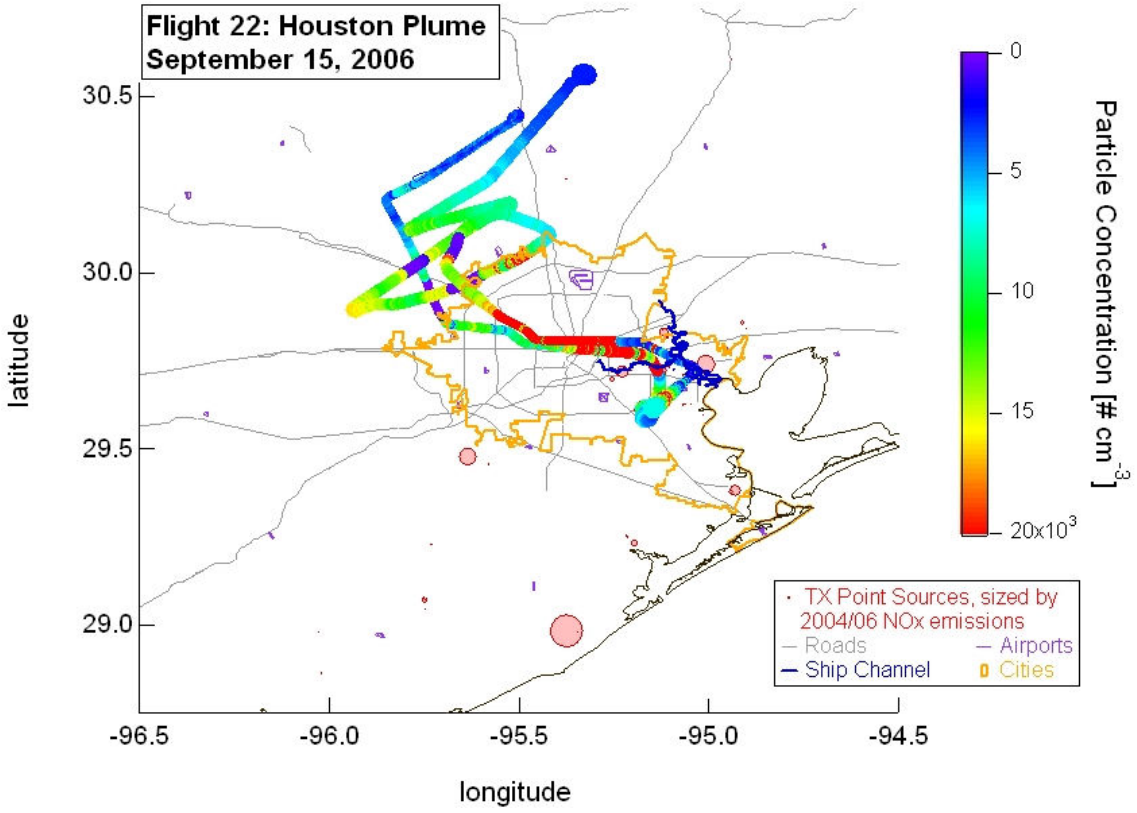


Figure 4.3 Flight track for RF 22 over the ship channel and downtown Houston, with color intensity representing the particle concentration

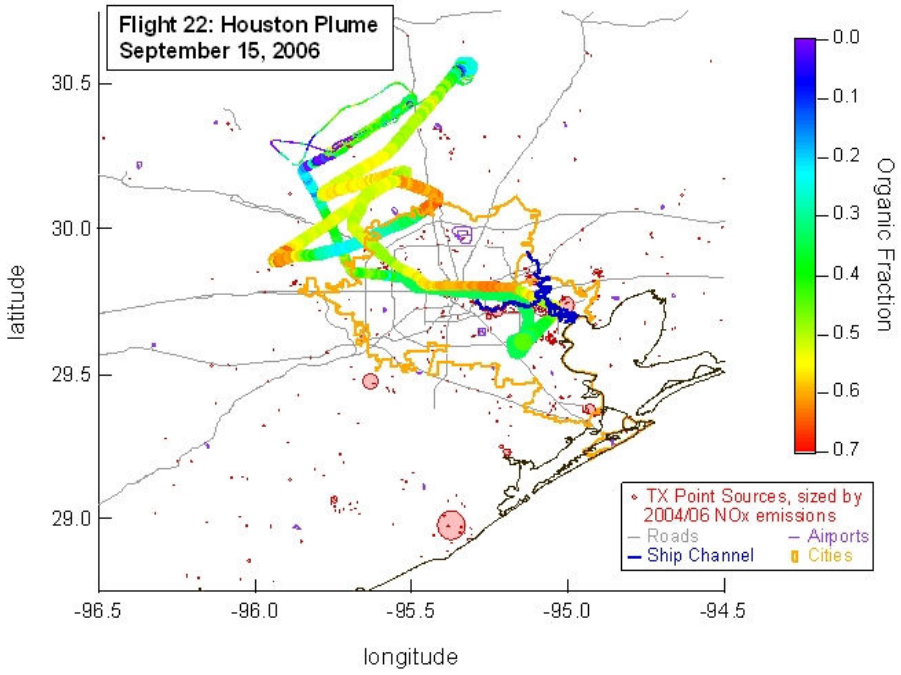


Figure 4.4. Flight track for RF 22 over the ship channel and downtown Houston, with color intensity representing the organic fraction

Figure 4.4 shows the same map with colors represented by the organic fraction (ε_{org}) defined as follows:

$$\varepsilon_{org} = \frac{m_{org} / \rho_{org}}{m_{org} / \rho_{org} + m_{AS} / \rho_{org}} \tag{5.2}$$

where m_{org} and m_{AS} are the mass loadings of organics and ammonium sulfate, respectively, ρ_{AS} is the density of ammonium sulfate and ρ_{org} is an average density of organics, assumed to be 1.4 g cm^{-3}. We make these assumptions to estimate a soluble volume fraction, which can be used directly in Köhler theory to predict CCN concentrations with the additional assumptions that the organics are insoluble and that

ammonium sulfate dominates the soluble fraction. In Figure 4.4 we see that the organic fraction is higher outside of the city and on the second pass back over the city later in the day. The high organics often correlate with high particle concentrations, but not always.

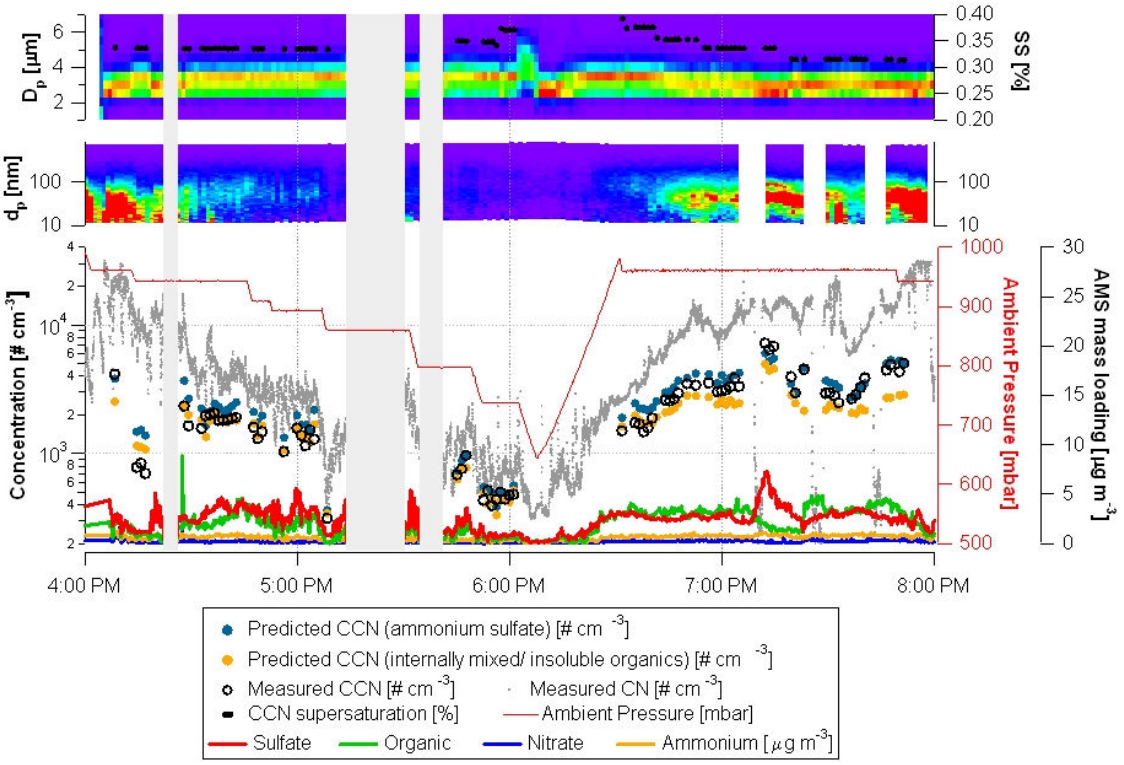


Figure 4.5. Timeseries of droplet diameter and CCNc supersaturation, dry particle diameter, measured and predicted CCN concentrations, total particle concentrations and ambient pressure

Figure 4.5 shows the time series of ambient pressure, particle concentrations greater than 10nm measured with a TSI 3010 condensation particle counter, the measured CCN concentrations, and predicted CCN concentrations given two different assumptions: 1) that the particles are pure ammonium sulfate, 2) that the particles are internally mixed with the organic fraction being insoluble and the rest being ammonium sulfate. These two cases represent our expected upper and lower bounds for the predicted CCN

concentrations, as there aren't many naturally occurring submicron aerosols that are more CCN active than ammonium sulfate, while many of the chemical compounds represented by the term "organics" are typically water soluble. Also plotted are the CCNc instrument supersaturation, the normalized droplet size distribution at the exit of the CCNc and the submicron dry particle size distribution.

The resulting CCN closure for flight 22 is shown in Figure 4.6, comparing the measured CCN concentrations to the predicted CCN concentrations given the two different assumptions about particle chemistry. For the predictions when particle chemistry is included, the markers are colored by the sulfate volume fraction ($1-\varepsilon_{org}$).

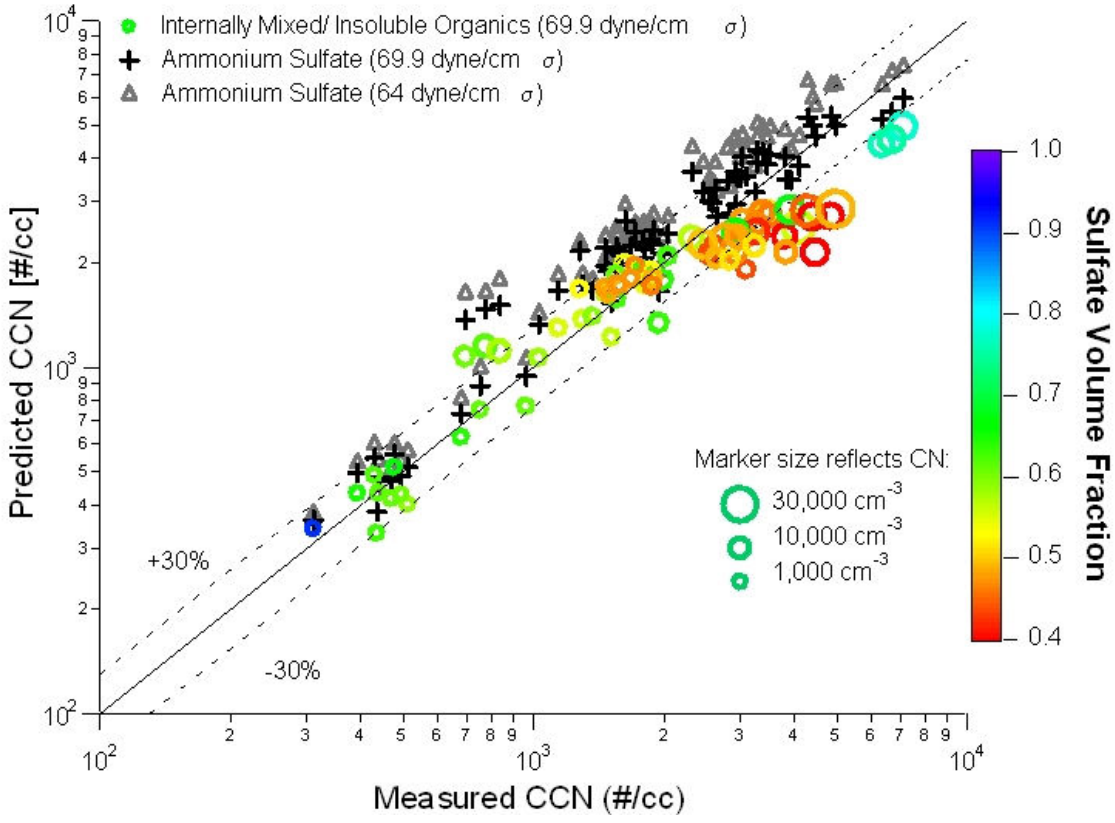


Figure 4.6. CCN closure for Flight 22, under different assumptions for the particle chemical composition

Figure 4.6 shows that CCN are overpredicted on average when assuming the particles are ammonium sulfate, although not always by the same amount. Assuming that the measured organic components are insoluble and internally mixed, the CCN closure is better for CCN concentrations less than about 2000 cm^{-3}. However, at the more polluted conditions (indicated by the marker size reflecting total particle concentrations), assuming internally mixed insoluble organics causes an underprediction of CCN. The more polluted conditions also typically have a higher fraction of organics. Size varying chemistry may explain this behavior; if the organics are high at the smallest particle sizes, which don't affect CCN concentrations much anyway, the CCN may behave similarly to ammonium sulfate even though high organic mass loadings are observed, especially when a significant bulk of the aerosol mass is in the Aitken mode. This may be what occurred at the start of flight 22 when CCN were underpredicted, as there were a large fraction of particles below 60 nm at this time (the dry critical diameter needed for activation of pure ammonium sulfate particles at ~0.3% supersaturation). Another explanation for the underprediction of CCN under the most polluted conditions may be that the organic constituents are simply different from those further from their source. It does not seem likely that freshly emitted organics are more hygroscopic than organics found further from source regions. A different explanation is that with high organic concentrations, the surface tension of the particles may be depressed, which could counteract, in terms of the particles' ability to activate, the lesser amount of solute. We show in Figure 4.6 the affect on the CCN closure of reducing surface tension by 5.9 dyne/cm, assuming that the particles are pure ammonium sulfate. This degree of surface tension reduction is easily plausible, as it has been shown for ambient aerosol in other

highly polluted environments [*Padro et al*, in prep; *Facchini et al*, 2001]. Including possible surface tension affects increases our upper limit for the CCN closure, and may also help to explain the cases when we underpredict CCN even when we assume that the particles are pure ammonium sulfate.

In some ways, the more difficult question is why we sometimes still overpredict CCN even when we assume that the organics are completely insoluble, as near the beginning of Flight 22. A possible explanation might be a delay in the growth rate leading to droplets smaller than the 0.75 μm detection threshold of the CCNc. However, the droplet growth data for this flight (Figure 4.5) shows that the average droplets size is at least 2 μm. If film-forming compounds existed only on some fraction of the droplets, then perhaps two droplet size modes could be present with one mode below the level of detection, but this would most likely show up as a tail in the observed droplet size distribution. On the contrary, the droplet sizes observed during these times appear to be larger.

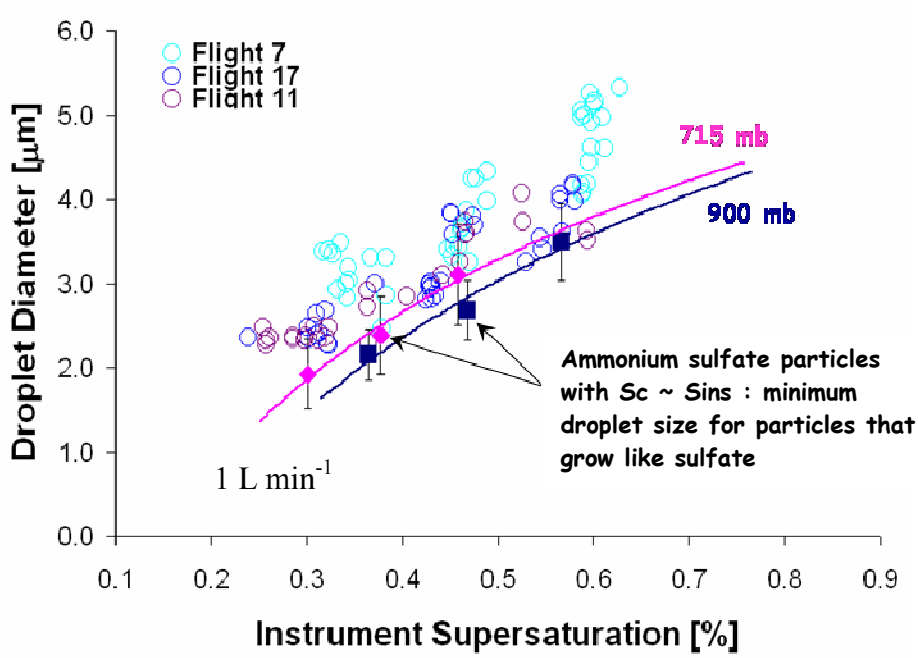
Another reason we might overpredict CCN, even when we assume that the measured organics are completely insoluble, is if the organics are concentrated in the larger particle sizes. Thus some of the sulfate that is believed to be contributing to the soluble mass in CCN may be actually in a separate size mode that is unavailable to activation at the given supersaturation. More likely, there is an external mixture of chemically heterogeneous particles. As shown in chapter 3, internally mixed particles are more likely to activate as they have at least some soluble material.

An interesting time period during Flight 22 is between 19:03 and 19:14 GMT, because the droplet growth decreases although the supersaturation is not significantly

changing. Then for the next 15 minutes the droplet size increases even though the supersaturation decreases. This change is especially interesting because it is anti-correlated with the hygroscopicity of the CCN; smaller droplets correspond to times when assuming ammonium sulfate brings better closure. Is it possible for organics to reduce the droplet surface tension and delay droplet growth at the same time? More likely, the more hygroscopic aerosol, and therefore higher number of CCN, cause a slight depletion of water vapor in the instrument which shifts the droplet size distribution to smaller sizes; this is afterall when we measure 6000-7000 cm^{-3} CCN! However, this would appear to be contradictory to our overprediction of CCN during this time period, as any depletion in water vapor should also activate fewer particles. What we know for a certainty is that the particle population is chemically changing during this time period and causes a dramatic shift in our ability to predict CCN. Although assuming the particles are ammonium sulfate often produces good closure on average, if greater than 50% prediction accuracy is desired for any given moment during a flight, simultaneous measurements of size resolved composition and mixing state as well as surfactant properties of the aerosol may be required.

For several flights (RF 7, 11 and 17) we varied the instrument supersaturation, and were thereby able to obtain a droplet growth spectrum, as shown in Figure 4.5. For comparison we show the average droplet diameter for classified ammonium sulfate particles obtained in the laboratory at 1 L min^{-1} total flow rate and at two different pressures, which have a critical supersaturation equal to the instrument supersaturation. This tells us the minimum droplet diameter expected at the outlet of the CCNc under those conditions. The minimum droplet diameter increases at lower pressures because

the maximum supersaturation in the CCNc occurs earlier in the column, and therefore the droplet have a longer time available for growth following activation, as shown in Chapter 2.



Flight 4.7. Average droplet diameter as a function of the CCNc supersaturation, compared to the minimum droplet diameter obtained from ammonium sulfate calibrations

For these flights, which were mainly over the ship channel and downtown Houston, the droplet growth is above the lower limit established by the calibration aerosol. The ambient particles that produced these droplets all have a critical supersaturation less than or equal to the instrument supersaturation. Those with a lower critical supersaturation will grow slightly larger. But, since we do not know the critical supersaturation of the particles, we cannot say exactly how large they "should" have been. What we can say is that none of the droplets grow more slowly on average than the lower limit of droplet growth, which indicates that the growth kinetics are not being

substantially delayed for any reason within the range of instrument supersaturations. This is contrary to the findings of *Ruehl et al* [2007] who report up to 62% of the particles having moderate kinetic inhibition to condensational growth at a ground-based site in Houston, using a phase doppler interferometer to monitor the droplet size. The apparent discrepancy between these observations will likely motivate future side-by-side comparisons of the instruments.

Conclusion

This study provides an airborne CCN closure analysis in an extremely polluted environment. The results show that on average the CCN closure is attainable with an overprediction bias of 10% for CCN concentrations ranging from 100 cm^{-3} to more than 10,000 cm^{-3} simply assuming a uniform chemical composition of ammonium sulfate for all particles. Furthermore, the CCN grow similarly to ammonium sulfate, with the measurable organics having an apparently negligible impact on the droplet growth kinetics. It is seen that the particle soluble fraction, estimated from the sulfate and organic mass loadings, is often useful for reducing the overprediction bias. Although the first order behavior of CCN is well constrained, variability in the quality of CCN closure may exceed a factor of two during particular flights, which indicates that further chemical information, such as the particle mixing state and surfactant properties of the organic constituents, is required.

REFERENCES

Abdul-Razzak, H., S.J. Ghan, and C. Rivera-Carpio, A parameterization of aerosol activation: 1. Single aerosol type. *J. Geophys. Res.*, 103, 6123-6131, 1998.

Abdul-Razzak, H. and S.J. Ghan, A parameterization of aerosol activation: 2. Multiple aerosol types. *J. Geophys. Res.*, 105, 6837-6844, 2000.

Baron, P.A. and K. Willeke (eds.), *Aerosol Measurement: Principles, Techniques, and Applications*, 2nd ed., Wiley-Interscience, Canada, 2001.

Berresheim, H., F.L. Eisele, D.J. Tanner, L.M. McInnes, D.C. Ramsey-Bell and D.S. Covert, Atmospheric Sulfur Chemistry and Cloud Condensation Nuclei (CCN) Concentrations over the Northeastern Pacific Coase. *J. Geophys. Res*., *98*, 12701-12711, 1993.

Boucher, O. and U. Lohmann, The Sulfate-CCN-Cloud Albedo Effect: A Sensitivity Study with Two General Circulation Models. *Tellus, Series B*, *47*, 291-300, 1995.

Broekhuizen K, Chang RYW, Leaitch WR, Li SM, Abbatt JPD, Closure between measured and modeled cloud condensation nuclei (CCN) using size-resolved aerosol compositions in downtown Toronto, Atmos. Chem. Phys. 6: 2513-2524 JUN 30 2006

Cantrell W, Shaw G, Cass GR, Chowdhury Z, Hughes LS, Prather KA, Guazzotti SA, Coffee KR, Closure between aerosol particles and cloud condensation nuclei at Kaashidhoo Climate Observatory, *J. Geophys. Res*., 106 (D22): 28711-28718 NOV 27 2001

Cantrell W, Shaw G, Leck C, Granat L, Cachier H, Relationships between cloud condensation nuclei spectra and aerosol particles on a south-north transect of the Indian Ocean, *J. Geophys. Res.*, 105 (D12): 15313-15320 JUN 27 2000

Charlson, R.J., J.H. Seinfeld, A. Nenes, M. Kulmala, A. Laaksonen, and M.C. Macchini, Reshaping the Theory of Cloud Formation. *Science*, *292*, 2025-2026, 2001.

Charlson, R.J., J.E. Lovelock, M.O. Andreae, S.G. Warren, *Nature*, *326*, 655, 1987.

Chen, D.R., D.Y.H. Pui, D. Hummes, H. Fissan, F.R. Quant and G.J. Sem, *J. Aerosol Sci*., 29, 497-509, 1998.

Chuang, P.Y., A. Nenes, J.N. Smith, R.C. Flagan, and J.H. Seinfeld (2000). Design of a CCN Instrument for Airborne Measurement, *J. Atmos. Oceanic Technol*., *17*: 1005-1019.

Chuang, P.Y. (2003). Measurement of the Timescale of Hygroscopic Growth for Atmospheric Aerosols. *J. Geophys. Res*., *108*: Art. No. 4282.

Conant, W.C., T.M. VanReken, T.A. Rissman, V. Varutbangkul, H.H. Jonsson, A. Nenes, J.L. Jimenez, A.E. Delia, R. Bahreini, G.C. Roberts, R.C. Flagan and J.G. Seinfeld, Aerosol-Cloud Drop Concentration Closure in Warm Cumulus, in press.

Cross, E.S., J. Kimmel, T.B. Onasch, X.Y. Yu, M.L. Alexander, D.R. Worsnop and P. Davidovits, A Time of Flight Aerosol Mass Spectrometer Combined with a Light Scattering Module: Results from the MILAGRO Field Study, *in preparation*.

Ervens B, Cubison M, Andrews E, Feingold G, Ogren JA, Jimenez JL, DeCarlo P, Nenes A, Prediction of cloud condensation nucleus number concentration using measurements of aerosol size distributions and composition and light scattering enhancement due to humidity, *J. Geophys. Res.*, 112 (D10): Art. No. D10S32 MAR 14 2007

Facchini, M.C., M. Mircea and S. Fuzzi, Notes and Correspondence: Comments on "Influence of Soluble Surfactant Properties on the Activation of Aerosol Particles Containing Inorganic Solute". *Amer. Met. Soc*., *58*, 1465-1467, 2001.

Facchini, M.C., S. Decesari, M. Mircea, S. Fuzzi and G. Loglio, Surface Tension of Atmospheric Wet Aerosol and Cloud/For Droplets in Relation to their Organic Carbon Content and Chemical Composition. *Atmos. Environ.*, *34*, 4853-4857, 2000.

Facchini, M.C., M. Mircea, S. Fuzzl, and R.J. Charlson, Cloud Albedo Enhancement by Surface-Active Organic Solutes in Growing Droplets. *Nature*, *401*, 257-259, 1999.

Feingold, G. and P.Y. Chuang, Analysis of the Influence of Film-Forming Compounds on droplet Growth: Implications for Cloud Microphysical Processes and Climate. *J. Atmos. Sci*., *59*, 2006-2018, 2002.

Finlayson-Pitts, B.J., and J. N. Pitts, *Atmospheric Chemistry: Fundamentals and Experimental Techniques*, John Wiley, New York, USA, 1986.

Fitzgerald, J.W. Marine Aerosols: A Review. *Atmos. Environ*., *25A*, 533-545, 1991.

Fukuta, N., and V.K. Saxena. A Horizontal Thermal Gradient Cloud Condensation Nucleus Spectrometer, *J. Appl. Meteorol*., *18*: 1352-1362, 1979.

Gultepe, I., and G.A. Isaac, Scale Effects on Averaging of Cloud Droplet and Aerosol Number Concentrations: Observations and Models. *J. Climate*, *12*, 1268-1279, 1999.

Hegg, D.A., R.J. Ferek and P.V. Hobbs, Light Scattering and Cloud Condensation Nucleus Activity of Sulfate Aerosol Measured over the Northeast Atlantic Ocean. *J. Geophys. Res*., *98*, 14887-14894, 1993.

Heintzenberg, J., D.C. Covert and R. Van Dingenen, Size Distribution and Chemical Composition of Marine Aerosols: A Compilation and Review. *Tellus, Series B*, *52*, 1104-1122, 2000.

Heintzenberg, J. Fine Particles in the Global Troposphere: A Review. *Tellus, Series B*, *41*, 149-160, 1989.

Hindmarsh, A. ODEPACK: A systematized collection of ODE solvers, in *Scientific Computing*, edited by Stepleman et al., pp. 55-64, North-Holland, New York, 1983.

Hoppel, W.A., S. Twomey, and T.A. Wojciechowski. A Segmented Thermal Diffusion Chamber for Continuous Measurements of CN, *J. Aerosol Sci*., *10*: 369-373, 1979.

Hudson, J.G. An Instantaneous CCN Spectrometer, *J. Atmos. Oceanic Technol*., *6*: 1055-1065, 1989.

Jones, A., D.L. Roberts and A. Slingo, A Climate Model Study of the Indirect Radiative Forcing by Anthropogenic Sulphate Aerosols. *Nature*, *370*, 450-453, 1994.

Khairoutdinov, M. and Y. Kogan, A New Cloud Physics Parameterization in a Large-Eddy Simulation Model of Marine Stratocumulus. *Mon. Weather Rev*., *128* (1), 229-243, 2000.

Kreith, F. and M.S. Bohn. *Principles of Heat Transfer*, 5th ed., PWS Publishing Company, 1997.

Lala, G.G., and J.E. Jiusto. An Automatic Light Scattering CCN Counter, *J. Appl. Meteorol.*, *16*: 413-418, 1977.

Leaitch, W.R., G.A. Isaac, J.W. Strapp, C.M. Banic, and H.A. Wiebe, The Relationship Between Cloud Droplet Number Concentrations and Anthropogenic Pollution: Observations and Climatic Implications. *J. Geophys. Res*., *97*, 2463-2474, 1992.

Li, Y.Q., P. Davidovits, Q. Shi, J.T. Jayne, C.E. Kolb and D.R. Worsnop, Mass and Thermal Accommodation Coefficients of H_2O (g) on Liquid Water as a Function of Temperature. *J. Phys. Chem*., *105* (47), 10627-10634, 2001.

Li, Z., A.L. Williams, and M.J. Rood, Influence of Soluble Surfactant Properties on the Activation of Aerosol Particles Containing Inorganic Solute. *J. Atmos. Sci*., *55* (10), 1859-1866, 1998.

Mason, B.J., *The Physics of Clouds*. Oxford Press, Oxford, 1971.

Medina J, Nenes A, Sotiropoulou REP, Cottrell LD, Ziemba LD, Beckman PJ, Griffin RJ, Cloud condensation nuclei closure during the International Consortium for Atmospheric Research on Transport and Transformation 2004 campaign: Effects of size-resolved composition, *J. Geophys. Res*, 112 (D10), 2007.

Mircea, M., M.C. Facchini, S. Decesari, S. Fuzzi and R.J. Charlson, The Influence of the Organic Aerosol Component on CCN Supersaturation Spectra for Different Aerosol Types. *Tellus, Series B*, *54*, 74-81, 2002.

Mozurkewich, M. Aerosol Growth and the Condensation Coefficient for Water: A Review. *Aerosol Sci. Technol*., *5*, 223-236, 1986.

Nenes, A. and Seinfeld, J.H. Parameterization of cloud droplet formation in global climate models *J. Geophys. Res., 108* (D7), 4415, doi: 10.1029/2002JD002911, 2003.

Nenes, A. R.J. Charlson, M.C. Facchini, M. Kulmala, A. Laaksonen, and J.H. Seinfeld, Can Chemical Effects on Cloud Droplet Number Rival the First Indirect Effect?, *Geophys. Res. Lett*, 24 (17), 1848, doi: 10.1029/2002GL015295, 2002.

Nenes., A., S. Ghan, H. Abdul-Razzak, P.Y. Chuang, and J.H. Seinfeld, Kinetic Limitations on Cloud Droplet Formation and Impact on Cloud Albedo, *Tellus, Series B*, *53*, 133-149, 2001.

Nenes, A., P. Chuang, R.C. Flagan and J.H. Seinfeld. A Theoretical Analysis of Cloud Condensation Nucleus (CCN) Instruments, *J. Geophys. Res*., *106*: 3449-3474, 2001.

Nenes, A. and J. Medina, Real-time measurements of CCN mixing state during NEAQS/ITCT2k4, *Geoph.Res.Lett.*, 2007.

Neusüβ, C., H. Wex, W. Birmili, A. Wiedensohler, C. Koziar, B. Busch, E. Brüggemann, T. Gnauk, M. Ebert, and D.S. Covert. Characterization and Parameterization of Atmospheric Particle Number-, Mass-, and Chemical-Size Distributions in Central Europe During LACE 98 and MINT. *J. Geophys. Res*., *107* (D21), 8127, doi:10.1029/2001JD000514, 2002.

Novakov, T., C. Rivera-Carpio, J.E. Penner and C.F. Rogers, The Effect of Anthropogenic Sulfate Aerosols on Marine Cloud Droplet Concentrations, *Tellus, Series B*, *46*, 132-141, 1994.

Pruppacher, H.R. and J.D. Klett, *Microphysics of Clouds and Precipitation*. Kluwer Academic Publishers, Dordrecht, Netherlands, 1980.

Quinn, P.K., D.S. Covert, T.S. Bates, V.N. Kapustin, D.C. Ramsey-Bell, and L.M. McInnes, Dimethylsulfide/Cloud Condensation Nuclei/Climate System: Relevant Size-Resolved Measurements of the Chemical and Physical Properties of the Atmospheric Aerosol Particles. *J. Geophys. Res*., *98*, 10411-10427, 1993.

Ramanathan, V. et al., Indian Ocean Experiment: An Integrated Analysis of the Climate Forcing and Effects of the Great Indo-Asian Haze. *J. Geophys. Res*., *106*, 28371-28398, 2001.

Rissman TA, VanReken TM, Wang J, Gasparini R, Collins DR, Jonsson HH, Brechtel FJ, Flagan RC, Seinfeld JH, Characterization of ambient aerosol from measurements of cloud condensation nuclei during the 2003 Atmospheric Radiation Measurement Aerosol Intensive Observational Period at the Southern Great Plains site in Oklahoma, *J. Geophys. Res*, 111 (D5), 2006.

Rissman, T., A. Nenes, and J.H. Seinfeld, Chemical amplification (or dampening) of the Twomey effect: Conditions derived from droplet activation theory, *J. Atmos. Sci., 61* (8), 919-930, 2004.

Roberts, G.C. and A. Nenes. A Continuous-Flow Streamwise Thermal-Gradient CCN Chamber for Atmospheric Measurements, *Aeros. Sci. Tech*., *39*: 206–221, 2005.

Ruehl1, C.R., P. Y. Chuang1, and A. Nenes, How quickly do cloud droplets form on atmospheric particles?, *Atmos. Chem. Phys. Discuss*., 7, 14233-14264, 2007.

Saxena, P. and L.M. Hildemann, Water-Soluble Organics in Atmospheric Particles: A Critical Review of the Literature and Application of Thermodynamics to Identify Candidate Compounds. *J. Atmos. Chem*., *24*, 57-109, 1996.

Seinfeld, J. and S. Pandis, *Atmospheric Chemistry and Physics: from Air Pollution to Climate Change*, John Wiley, New York, 1998.

Shaw R.A. and D. Lamb, Experimental Determination of the Thermal Accommodation and Condensation Coefficients of Water, *J. Chem. Phys*., *111* (23), 1999.

Shulman, M., M. Jacobson, R. Charlson, R. Synovec, and T. Young, Dissolution Behavior and Surface Tension Effects of Organic Compounds in Nucleating Cloud Droplets. *Geophys. Res. Lett*., *23*, 277-280, 1996.

Sinnarwalla, A.M., and D.J. Alofs. A Cloud Nucleus Counter with Long Available Growth Time, *J. Appl. Meteorol*., *12*: 831-835, 1973.

Smith, J.M., H.C. Van Ness and M.M. Abbott. *Introduction to Chemical Engineering Thermodynamics*, 5th ed., McGraw-Hill Companies, Inc, 1996.

Solomon, S., D. Qin, M. Manning, M. Marquis, K. Averyt, M.M.B. Tignor, H.L. Miller, Z. Chen, Climate Change 2007: The Physical Science Basis. Contribution of Working Group I to the Fourth Assessment Report of the Intergovernmental Panel on Climate Change, Cambridge University Press, Cambridge, 2007.

Turpin, B.J. and H.J. Lim, Species Contributions to PM2.5 Mass Concentrations: Revisiting Common Assumptions for Estimating Organic Mass. *Aerosol Sci. Technol*., *35*, 602-610, 2001.

Stroud CA, Nenes A, Jimenez JL, DeCarlo PF, Huffman JA, Bruintjes R, Nemitz E, Delia AE, Toohey DW, Guenther AB, Nandi S, Cloud activating properties of aerosol observed during CELTIC, *J. Atmos. Sci*., 64 (2): 441-459, 2007

Twomey, S. Pollution and the Planetary Albedo. *Atmos. Environ*., *8*, 1251-1256, 1974.

Twomey, S. Measurements of Natural Cloud Nuclei, *J. Rech. Atmos*., *1*: 101-105, 1963.

VanReken, T.M., A. Nenes, R.C. Flagan and J.H. Seinfeld. Concept for a New Cloud Condensation Nucleus (CCN) Spectrometer, *Aeros. Sci. Tech*., *38*: 639-654, 2004.

Vestin A, Rissler J, Swietlicki E, et al., Cloud-nucleating properties of the Amazonian biomass burning aerosol: Cloud condensation nuclei measurements and modeling, *J. Geophys. Res.*, 112 (D14), 2007.

Whitby, K.T. and G.M. Sverdrup. California Aerosols: Their Physical and Chemical Characteristics, within *The Character and Origins of Smog Aerosols: A Digest of Results from the California Aerosol Characterization Experiment (ACHEX)*. John Wiley, New York, 477-517, 1980.

Whitby, K.T. The Physical Characteristics of Sulfur Aerosols. *Atmos. Environ*., *12*, 135-159, 1978.

Yum, S.S., J.G. Hudson, K.Y. Song, and B-C Choi, Springtime cloud condensation nuclei concentrations on the west coast of Korea, *Geophys. Res. Lett*., VOL. 32, 2005.

Zelenyuk, Cai and Imre. From Agglomerates of Spheres to Irregularly Shaped Particles: Determination of Dynamic Shape Factors from Measurements of Mobility and Vacuum Aerodynamic Diameters," submitted to *Aeros. Sci. Tech,* 2005.

VITA

SARA M. LANCE

Ms. Lance was born in Phoenix, Arizona. She received a B.S.E. degree in Chemical Engineering from Arizona State University, Tempe, Arizona in 2002 before coming to Georgia Tech to pursue a doctorate in Atmospheric Science.